Development of a Corrugated Core Sandwich Panel with Enhanced MMOD Shielding Capability

by

Tanvir Howlader

A Thesis Submitted to the Faculty of Graduate Studies of

The University of Manitoba

In partial fulfilment of the requirements of the degree of

MASTER OF SCIENCE

Department of Mechanical Engineering

University of Manitoba

Winnipeg

ABSTRACT

The growing threat of orbital debris is a significant concern for active and future spacecraft. This study exploits the concept of redesigning the components of spacecraft, adding to them a new function of space debris protection. The sandwich panel is a traditional member of the satellite structure due to its high structural support capability. However, the honeycomb sandwich panel, the most commonly used sandwich structure, has demonstrated a very low efficiency for protection against space debris. Therefore, it's necessary to examine other types of sandwich panels that can serve structural purposes and simultaneously provide adequate protection against space debris.

This thesis thoroughly investigated the shielding performance of a Corrugated Core Sandwich Panel (CCSP) against hypervelocity impact as a potential alternative to conventional shield designs. To eliminate the current limitation of the experimental investigation, a robust numerical model was developed using a combination of Smoothed-Particle Hydrodynamics (SPH) technique and the Finite Element Method (FEM) in ANSYS/AUTODYN software. The developed numerical models were validated using experimental data. Parametric studies identified the areas on the CCSP that are susceptible to hypervelocity impact and its effect on the overall shielding performance of the panel. Several strategies to enhance the shielding performance of the CCSP have been proposed. Upgrading the corrugated core of the CCSP configuration leads to a 20.5% improvement. In addition, it was demonstrated that the CCSP performance could be further enhanced with ballistic inserts containing aramid or ceramic fabric layers. A triangular prism-shaped polymeric foam has been suggested for making the inserts, which are meant to fit the space within the corrugated plate core.

ACKNOWLEDGEMENTS

To begin, I would like to express my gratitude to my supervisor, Dr. Igor Telichev, for providing unflinching support throughout the project. My progress toward finishing my research was facilitated by his suggestions and comments, which kept me on the right track. I would like to thank my colleagues, Victor Babarinde and Majid Fazlollahi, for their continuous support.

The financial support provided by the Natural Sciences and Engineering Research Council of Canada (NSERC), Magellan Aerospace Winnipeg (MAW), and the University of Manitoba is greatly acknowledged.

Finally, and most importantly, I would like to thank my late Grandma for all her love, support and encouragement.

CONTENTS

LIST OF FIGURES

LIST OF TABLES

LIST OF ACRONYMS

AD	Areal Density
BLC	Ballistic Limit Curve
CC	Corrugated Core
CCSP	Corrugated Core Sandwich Panel
CFD	Computational Fluid Dynamics
CNSA	China National Space Administration
CSA	Canadian Space Agency
CSM	Computational Solid Mechanics
DEM	Discrete Element Method
EOS	Equation of State
ESA	European Space Agency
FCSP	Foam-Core Sandwich Panel
FDM	Finite Different Method
FEM	Finite Element Method
FLIP	Fluid Implicit Particle
GEO	Geostationary Equatorial Orbit
GIMP	Generalized Interpolation Material Point
HCSP	Honeycomb-Core Sandwich panel
HVI	Hypervelocity Impact
LEO	Low Earth Orbit
MFSP	Multi-Functional Sandwich Panel
MMOD	Micro-Meteoroids and Orbital Debris
MPM	Material Point Method
MPEM	Membrane Particle-Element Method
NASA	National Aeronautics and Space Administration
NS	Navier Stokes
SPH	Smooth-Particle Hydrodynamics
SSN	Space Surveillance Network
UM-ORDER Group	University of Manitoba Orbital Debris Research Group
WS	Whipple Shield

1. INTRODUCTION

1.1 Space Environment

Humankind's desire to unveil space mysteries and advance our lifestyle has resulted in the launch of frequent payloads into earth orbit throughout the years, resulting in orbital debris around the Earth and the meteoroid threat. More than 6,250 (excluding failures) launches have been placed since the first launch of Sputnik-1 on October 4, 1957, ushering in the space era [1]. During each satellite launch, extra components such as instrument covers, rocket stages, and burnt fuel are left in orbit. Such object collisions between or explode accidentally or deliberately have generated a vast number of fragments of varying sizes over the years.

The earliest known destruction occurred in June 1961, when more than 200 space junk (payloads, rocket bodies, and mission-related debris) encountered on-orbit breakups [2]. A French satellite was struck and destroyed in 1996 by debris from a French rocket that had detonated a decade before. The intentional destruction of one inactive weather satellite happened in 2007 by China's anti-satellite missile, adding more than 3,500 pieces of substantial, trackable debris and much smaller debris to the debris problem. An operational US Iridium commercial spacecraft was destroyed on February 10, 2009, after it collided with a defunct Russian spacecraft. More than 2,300 pieces of trackable debris as well as many smaller debris pieces, were added to the space trash inventory as a result of the impact. [3].

Artificial satellites and spacecraft are essential for communications, weather forecasting, scientific research, and national security, so they have become an important part of the standard of living. The growing number of space junk has become the most significant threat to the safety and reliability of these satellites and future space missions. Because of the extremely high velocity (on average, about 11 km/s) in a collision, even small particles (1-5mm) can damage, degrade or destroy spacecraft [2]. Risk analysis studies have indicated that space debris or meteoroid impact damage can have a wide range of effects on Spacecraft [4] - [6]. For instance, a modest impact on the pressure vessels of a spacecraft may trigger a leak or burst, resulting in the mission's early termination with the risk of ejecting more debris in orbit (mostly in LEO and GEO). Or collision

with an electronics box cover can lead to interior fragments (i.e., spall particles), which can be lethal to the sensitive equipment of spacecraft.

The Space Surveillance Network (SSN) is capable of tracking space junk larger than 10 cm and discrete objects as small as 5 cm in diameter in low-Earth orbit and 1 meter in geosynchronous orbit accurately. Objects smaller than this are too small to be tracked for collision risk assessments and avoidance. According to ESA [7], there will be approximately 36500 objects larger than 10 cm, 1 million objects between 1 cm and 10 cm, and 130 million pieces of debris between 1 mm and 1 cm crossing the space environment at a very high speed. The growing number of space junk/debris is demonstrated in Fig. 1.1.

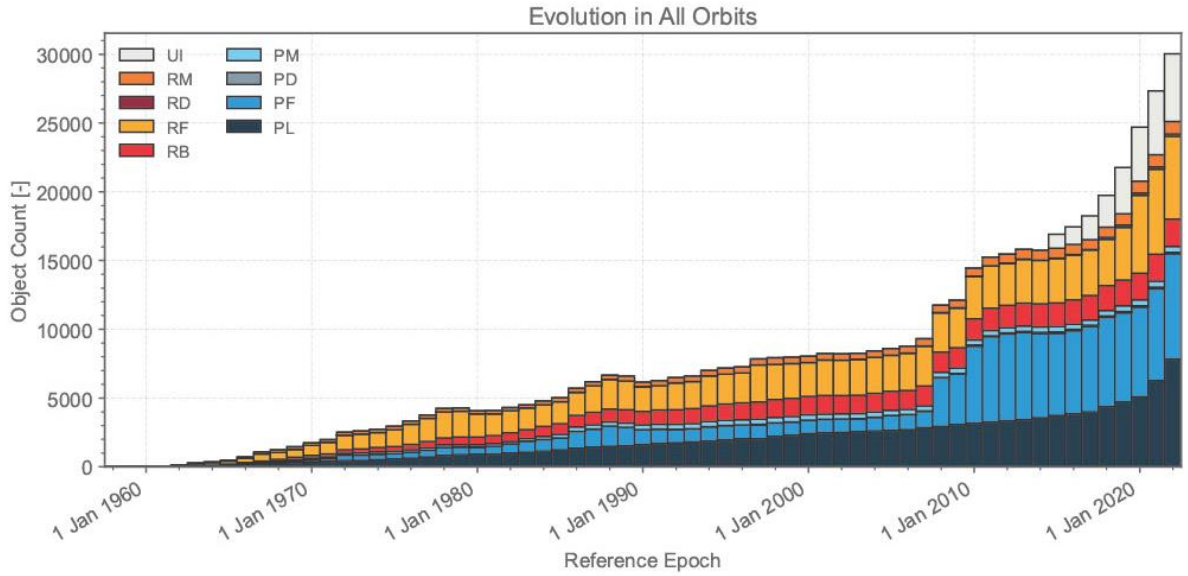

Figure 1.1 Growing number of space objects [PL = Payload (usually one or many satellites that a rocket launches to space); PF = Payload Fragmentation Debris; PD = Payload Debris; PM = Payload Mission Related Object; RB = Rocket Body; RF = Rocket Fragmentation Debris; RD = Rocket Debris; RM = Rocket Mission Related Object; UI = Unidentified [7].

Explosions and collisions with existing space derelicts can cause space debris to damage active spacecraft. And if not properly managed, they may result in a cascading effect generally known as the "Kessler Syndrome," as proposed by Donald Kessler in 1978 [8]. If the cascading effect occurs in Earth's orbit, our present and future space exploration may come to an end.

Hence, it is essential to employ a consistent set of damage regulations that handle the diverse effects of Hypervelocity Impact (HVI) [9],[10]. When a trackable space junk orbit path comes close to an active spacecraft, the spacecraft authority may use maneuver technic to avoid the

collision, called active defense. In contrast, in the case of untraceable space debris collision, the spacecraft must rely entirely on external shields to protect the satellite [6]. Micrometeoroids and Orbital Debris (MMOD) shield is considered one of the well-recognized ways to protect spacecraft from non-trackable debris.

1.2 Research Problem

Fred Lawrence Whipple proposed the initial design of an orbital debris shield in 1947, a structure containing two face sheets separated from each other by some distance, currently known as the Whipple shield (WS) [11]. This configuration is simple but effective. A WS is made of two plates, the bumper and rear wall, separated by a standoff distance. When space debris hits the bumper at hypervelocity, high-intensity shock waves are generated and propagate in both debris and the bumper due to the high kinetic energy involved. The shock wave interaction with interfaces causes the fragmentation of the colliding object, turning them into a debris cloud. As the debris cloud moves towards the rear wall, the debris cloud expansion causes its momentum to spread over a big area of the rear wall. And if the rear wall is thick enough, it can withstand impact loading from fragments preventing its perforation [12]. A WS is schematically shown in Fig. 1.2.

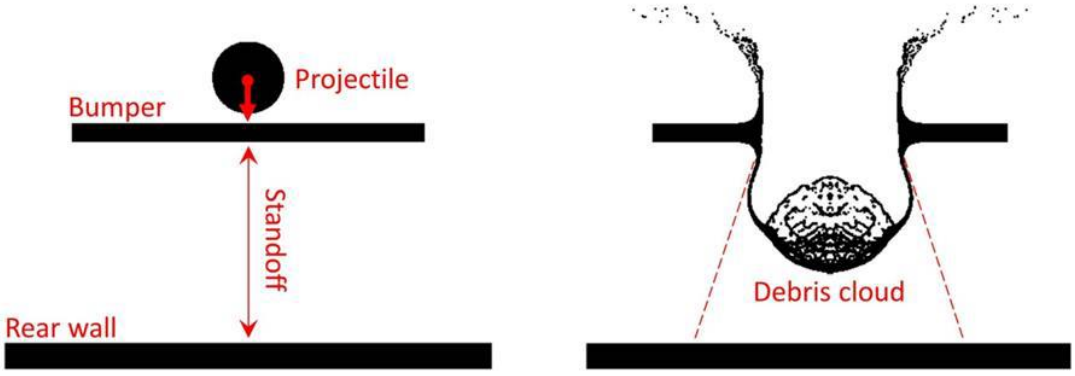

Figure 1.2 Diagram of a Whipple shield: before impact (left) and after perforation of the bumper (right) [13]

Despite recent advancements in rocket launching efficiency, the weight efficiency of all satellite components, including MMOD protection, remains a significant concern [14]. The ballistic properties of WS have been thoroughly studied in recent decades, leading to improvements in ballistic performance and weight efficiency through upgrades in design, such as adding multiple

plates between the bumper and rear wall in multi-shock shields or employing a mesh bumper [15], [16]. However, utilizing the concept of single-purpose shields might not be a weight-efficient approach, especially for Low Earth Orbit (LEO) satellite missions. Although such systems provide reasonable protection against the orbital debris impact, they require an additional supporting structure that adds to the system's overall weight and volume [17] [18]. For instance, roughly half of the total shielding weight in the Columbus module was used for supporting structures [19]. In order to avoid this mass penalty, the University of Manitoba Orbital Debris Research Group (UM-ORDER Group) introduced the concept named “ENSURE” (ENhanced SURvivability Element) based on the idea of redesigning the original structural parts to enhance their inherent protection capability without the prohibitive additional weight.

One of the possible solutions to improve the weight-efficiency is to employ the concept of multi-functionality. The concept of multi-functionality refers to a panel that may serve several objectives. For instance, a panel that can sustain mechanical loads may also provide additional protection against orbital debris and radiation. Comparing such Multi-Functional Sandwich Panel (MFSP) to a single-purpose shield can help a satellite be overall lightweight. Thus, MFSP gained considerable interest in the research community. Generally, an MFSP with a function of MMOD protection consists of 3 parts, front facesheet (Bumper), core structure, and rear facesheet (rear wall).

The Honeycomb Core Sandwich Panel (HCSP) is a conventional panel that has been used as a primary satellite structure for its excellent properties, such as its high strength-to-weight ratios [20].

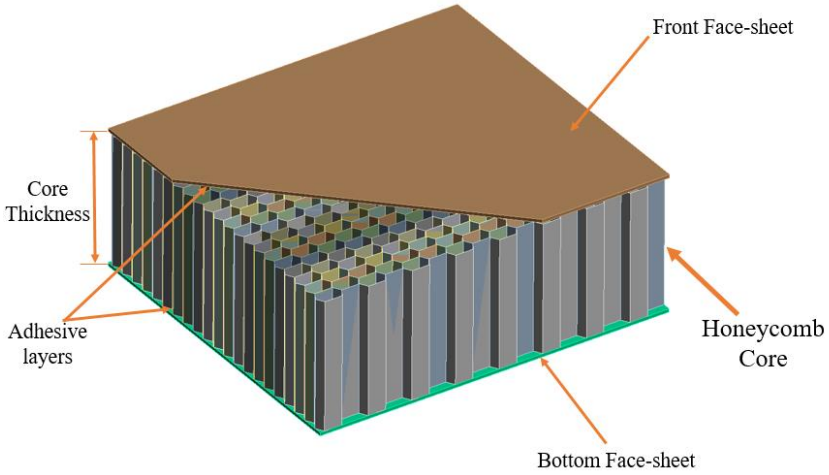

Figure 1.3 Honeycomb core sandwich panel

However, HCSP has very poor MMOD protection capability. In the case of HCSP, it suffers from the channelling effect caused by the honeycomb core's hexagonal structure cell. These cells prevent the debris cloud from expanding into a larger area and make the cloud concentrate in a small region. The narrow cluster of fragments impacts this small region and easily penetrates the rear wall. Fig. 1.4 shows a debris cloud expansion behind the bumper in the Whipple shield after HVI at 7 km/s (Fig. 1.4a) and illustrates the channelling effect in HCSP (Fig. 1.4b).

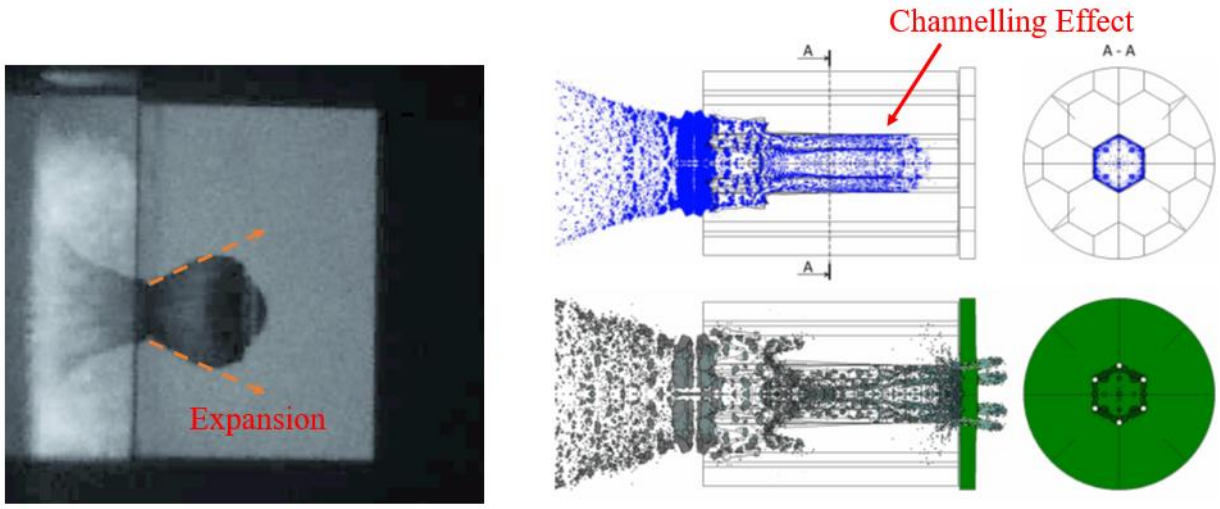

(a) (b)

Figure 1.4 Debris cloud expansion behind the bumper plate in the case of Whipple Shield (a) and HCSP (b) [13]

Experiments showed that HCSP shielding performance was comparable to a Whipple shield with 50% lower back wall thickness [80]. Besides, Foam Core Sandwich Panel (FCSP) demonstrated better protection level using 25 – 30% less areal density than HCSP in an experimental study conducted by NASA [81]. Consequently, HCSP orbital debris protection capability was not studied further in this thesis.

By redesigning the core, MMOD protection functionality can be added to the panel. The first MFSP alternative to the conventional HCSP with single-purpose external shielding is a FCSP. Several research teams, including the UM-ORDER Group, are currently evaluating the potential uses of FCSP. Another promising alternative to single-purpose external shielding can be a sandwich panel with a Corrugated Core (CC).

1.3 Research Gap

There is still a continuous effort to improve the shielding performance of sandwich panels to the escalating threat of orbital debris. Besides, the vulnerability of HCSP due to the channelling effect during HVI raises the need for alternative solutions. Therefore, examining other types of sandwich panels that can serve structural purposes and simultaneously provide considerable protection against space debris is necessary. A Corrugated Core Sandwich Panel (CCSP) can be a viable alternative to the conventional lightweight sandwich panel such as HCSP due to its adequate structural integrity [21] and the potential to provide considerably better ballistic performance.

Although CC sandwich panels have been used in various structural applications such as aerospace, transportation and civil industry due to their high structural integrity [22], their MMOD protection capability hasn't been studied comprehensively, specifically the effect of corrugated core on shielding performance. Additionally, no research has been conducted to understand the behavior of debris clouds within the sandwich core and to enhance the shielding performance by solely upgrading the CC configuration.

1.4 Research Objective

A multifunctional sandwich panel can be a weight-efficient solution compared to the conventional structural panel of spacecraft with a mounted single-purpose external MMOD shield. The challenge is finding a panel that offers robust protection against space debris while supporting mechanical loads. Limited research exists on the MMOD shielding capability of CC sandwich panels. This thesis aims to address the gap in knowledge about their MMOD protection performance by formulating the following objectives:

1. To develop and validate a numerical model to simulate the behavior of sandwich panels with the corrugated core subjected to hypervelocity impact.
2. To conduct a parametric analysis of the corrugated core sandwich panel using the developed numerical approach.
3. To design an advanced CCSP configuration with improved shielding performance by modelling the interaction of the debris cloud with a corrugated core.

4. Develop weight-efficient configurations of CCSP which has sufficient protection against space debris. Protecting the robotic satellite in LEO against a 5.16 mm spherical projectile at 7 km/s was selected for the analysis.

1.5 Thesis Formulation

A review of publications is discussed in chapter 2 regarding corrugated core sandwich panel structural integrity and ballistic performance. Besides, a brief description of the physics behind the hypervelocity impact phenomenon and numerical simulation methodologies is also included.

Chapter 3 presents the numerical modeling approach for CCSP, the calibration procedure, and the material model to predict the hypervelocity event with adequate accuracy and reasonable computational cost. This chapter also includes the experimental test setup and compares test results with the simulation data.

In chapter 4, the impact of the corrugated core is analyzed, and the most vulnerable areas of the corrugated core against high-speed impact are identified. Besides, the critical diameter for the different impact locations of the CCSP is also discussed in this chapter. Finally, it is pointed out how corrugated core geometry influences the ballistic limit and structural stiffness of CCSP.

In Chapter 5, several candidate configurations of the corrugated core are introduced and analyzed to overcome the drawbacks of the CCSP and to evaluate their performance compared to the original core design.

Chapter 6 evaluates the effect of adding ballistic fabric and concludes that a CCSP with fabric inserts can be one of the most lightweight solutions to enhance the shielding performance of the CCSP.

Finally, Chapter 7 discusses key findings from the research and recommendations for future study.

2. LITERATURE REVIEW

2.1 Corrugated Core Sandwich Panel (CCSP)

A literature review on the topic of CCSP's ballistic performance is discussed in Chapter 2. CC sandwich panels are made up of two thin facesheets with little flexural stiffness about their centroidal axes and a strongly orthotropic core. A secure bind of a CC with two facesheet is able to resist vertical deformations and allows the overall structure to act as one thick plate due to shear force strength. A CCSP has to have higher or equal stiffness of the material of facesheet than the core [23]. Such panels have a reasonable strength-to-weight ratio [24]. Besides, the configuration provides an adequate area to expend the debris cloud without making any channeling effect that occurs in an HCSP scenario.

2.1.1 The Geometry of CC Sandwich Panel

The term corrugated panel refers to any structure created by folding, molding, or any other manufacturing method that has a surface with the shape of a corrugation. CC sandwich panels have long been considered a straightforward and practical technique for constructing lightweight structures with good anisotropic behavior, buckling resistance, and energy absorption capabilities. Several CC configurations, such as triangle core, trapezoid core, X-shape core, etc., can be utilized. For decades, these corrugated structures have been utilized in various structural applications, including aerospace, because of their distinct properties [22]. Figure 2.1 illustrates five distinct geometries for corrugated core configurations.

The characteristics of the face sheets and corrugated core, such as geometry and material, significantly impact the structural performance of a CCSP. CC sandwich panels have a considerably superior shear modulus in the longitudinal than the transverse plane. Bending rigidity in the transverse direction is limited, and shear distortions are only tolerated in the plane perpendicular to the corrugations [26].

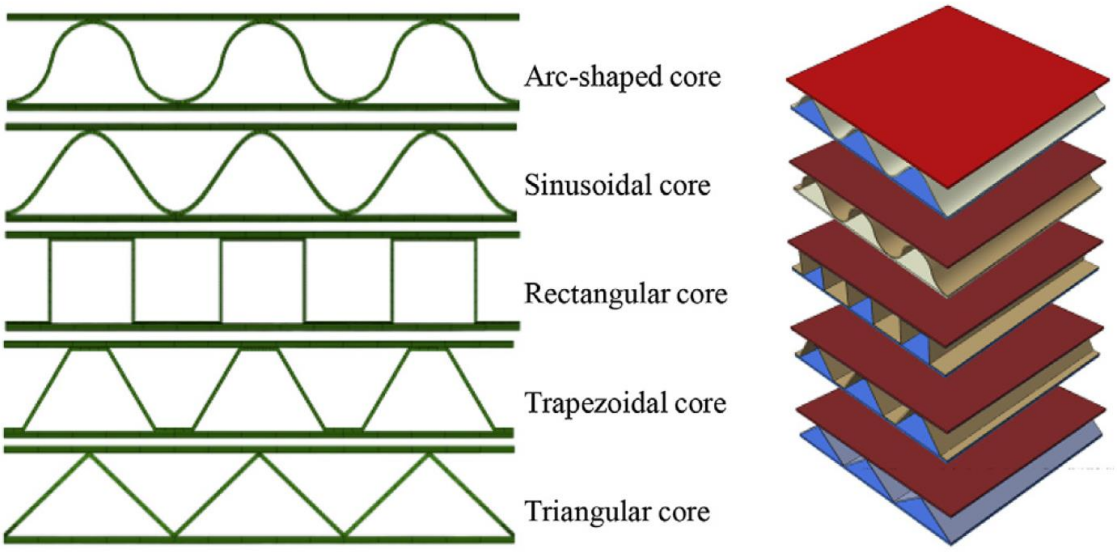

Figure 2.1 Panels with five corrugated core geometry configurations [25]

2.1.2. Ballistic Properties of CCSP

In 1991, W. P Schonberg and R.J. Tullos [27] analyzed a corrugated bumper in a Whipple shield and compared its ballistic performance with a monolithic bumper. The study used two different geometric parameters of the trapezoid core and then compared them with the monolithic bumper. The research revealed that a corrugated design is more effective than a monolayer bumper in protecting walls from getting perforated. A similar study was conducted by Hao Zhou et al. [28]. They employed a corrugated shield as a bumper and filled the empty space of the bumper with epoxy. Their research found a better fragmentation of projectile than a monolithic bumper. In 2020, Lorenzo et al. [29] conducted an experimental study with a 3D–printed multi-shock shield, corrugated core sandwich panel, and hybrid shielding configuration with a single-layer rear wall and a corrugated bumper. The CCSP and hybrid shielding configuration performed slightly better than a multi-shock shield. Another investigation was performed in 2021 by Adrian D., Scott. J. I., et al. [30]. In the research, both experimental and numerical results showed that CCSP provided slightly better protection against the HVI than multi-shock shield when both shields have the same areal density. The concept was found to be promising from the previous study, but a detailed study regarding the protection level against space debris was not performed.

2.2 Physics Behind Hypervelocity Impact

It is essential for this study to comprehend the physical phenomena of collision events. Both objects involved in the collision experience the propagation of compressive and tensile waves. The intensities of these waves increase along with the impact velocity. The shock waves of high intensity may cause fragmentation in both colliding materials. Thus, if the shock wave is strong enough, the material can experience the transition from solid to liquid or gas due to an excessive rise of entropy.

2.2.1 Material Response to Hypervelocity Impact

Immediately after impact, two shock waves propagate away through the interface of the projectile and target plate. Each element of the projectile and target experiences considerable pressure due to the shock waves (compressive wave). Subsequently, two rarefaction waves are generated and have been transmitted through the projectile and target. The rarefaction waves (tensile wave) bring the components of the projectile and target plate to ambient pressure. Fig 2.2 illustrates this process as a pressure-volume plot.

From the initial density ρ_0, the pressure of each element reaches Hugoniot pressure P_H by a shock wave following the Hugoniot curve from points 1 to 2. Subsequently, the rarefaction wave causes the pressure of materials (element of projectile and target plate) to return at ambient conditions (points 2-3). Although the releasing process is adiabatic, the initial shocking process is non-isentropic. This procedure increases the entropy of the material (generates heat in the material). The size of the dashed triangle represents the specific internal energy e_H of the material due to compressive wave.

However, when the energy is returned in an isentropic way, the volume of material expands in the area. The area under the triangle is bigger than the latter portion. The difference between the two regions is proportional to the amount of remaining heat in the element. The material will remain hot yet in a solid condition if the intensity of the shock is not high enough (when the impact velocity is less than 3 km/s). Entropy increases quickly when shock strength is increased, which can lead to melting, vaporization, or superheated vapor in the final state [31]. For instance, at HVI (3~7

km/s), the shock strength of the projectile and target turns out to be high enough to melt contact objects partially.

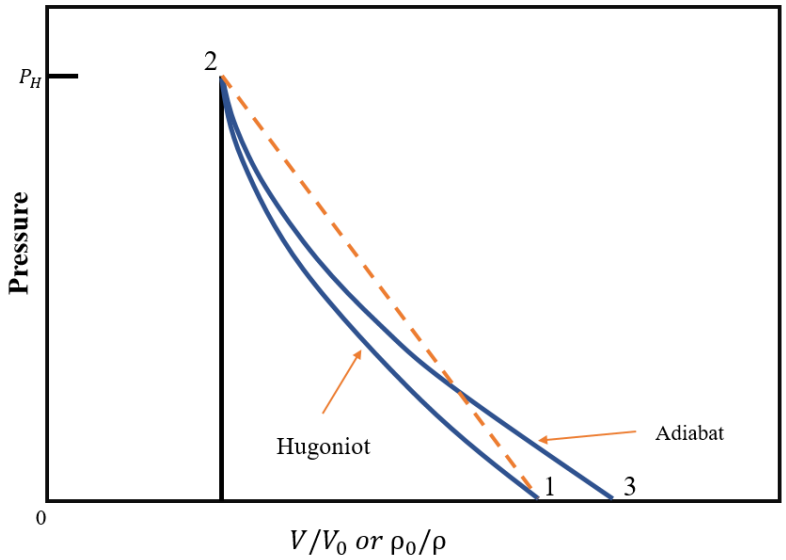

Figure 2.2 Pressure and volume curve [31]

2.2.2 Hypervelocity Impact on Thin Plate

In the scenario of HVI on thin plate, better fragmentation and dispersion of the projectile may lead to significant decay of the projectile's momentum. The shock wave from HVI causes fragmentation. Thus, it's essential to comprehend the shock phenomenon.

The shock wave phenomena can be explained in two steps:

a) A shock wave is created in the target plate and projectile and propagates toward the rear surface of the target and inside projectile immediately after impact.
b) The shock wave reflects from free surfaces, including the projectile, as a tensile wave, and interferes with the initial compression wave within the projectile.

Two shock waves S_1 and S_2 are generated immediately after impact and spread out from where the projectile and target plate met (the interface). Both projectile and target plate materials are discharged backward due to the formation of two rarefaction waves R_1, and R_2. These rarefaction waves propagate toward the axis of the projectile, as shown in Fig. 2.3 (a). As the process continues, the shock S_2 penetrates the target plate's interface and reaches its rear surface.

Afterward, the shock is reflected as a rarefaction R_3 in order to meet the boundary condition of zero pressure, as shown in Fig. 2.3 (b). Gradually, the bubble expands as material from the target plate, and projectile is added.

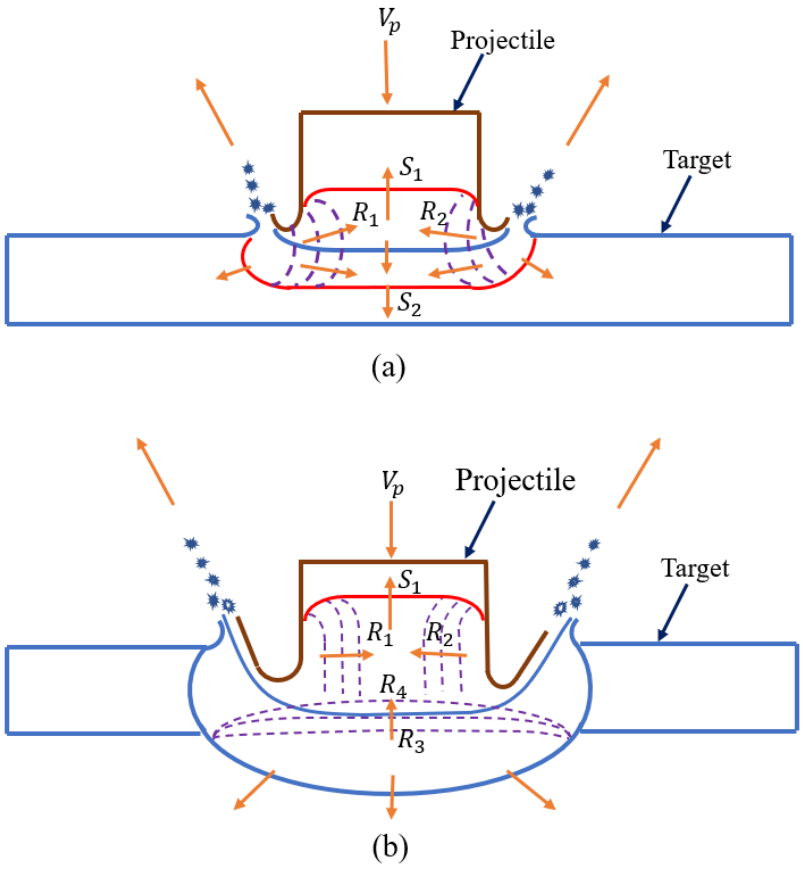

Figure 2.3 Shock waves have propagated through the projectile and target plate [31]

The rarefactions R1, R2, R3, and R4 formed to meet boundary conditions are acted like tension waves. When the tensile stress at any point in the target plate or projectile exceeds the tensile stress, fracture will occur. In addition, to satisfy boundary conditions at any new fracture surfaces, rarefactions will be generated, and these rarefactions may lead to further fractures. The entire process of projectile and target plate fracture can be called a "multiple spalling phenomena," which commences at the free surfaces [31]. In summary, when a projectile hits a thin target plate at a very high velocity, the impact generates a shock wave which leads to a rarefaction wave (tensile wave). This causes the fragmentations of both projectile and the target plate. The fragmentation process can vary depending on the material density, strength, sound speed, parts geometry, and impact velocity.

2.2.3 Ballistic Limit Curve (BLC)

For a specific structural or shielding arrangement, ballistic limit curve indicates the threshold of perforation. The BLC can be split into three regimes: ballistic range, transition (or shatter) range and melt/vaporize range [32]. These three regimes can be determined by physical tests when the projectile impacts the bumper. A conventional BLC of a Whipple shield compared with a single plate is demonstrated in Fig. 2.4.

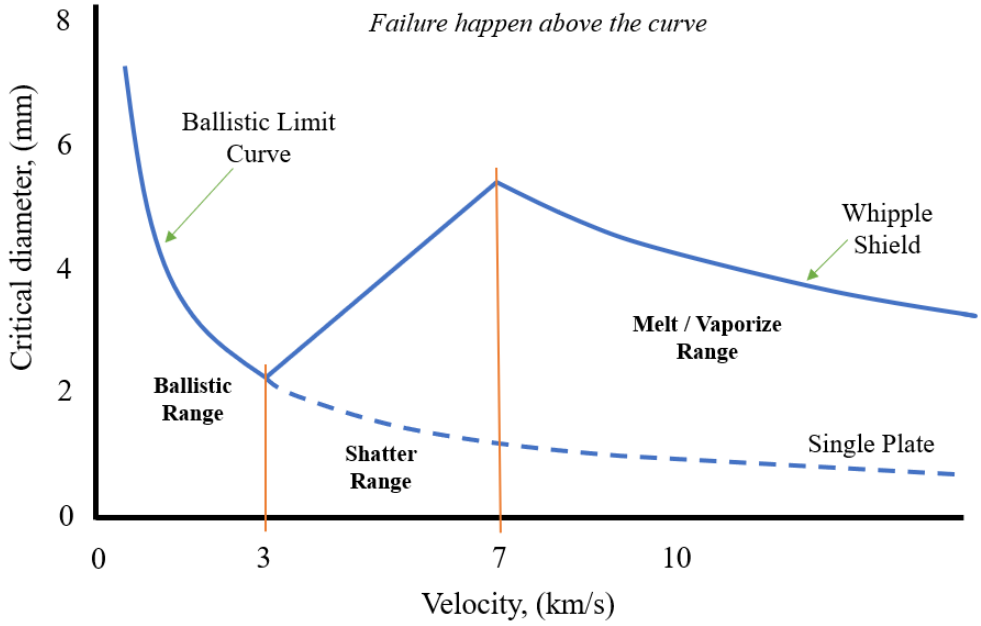

Figure 2.4 A conventional BLE of a Whipple shield compared with a single plate [32]

In the Ballistic range (up to 3 km/s), the projectile deforms but mostly remains intact due to low shock wave pressure from impact. Then the remaining part of the projectile impacts the rear wall of the shield. In the low velocity (ballistic range), the projectile becomes more destructive as velocity rises. In the transition regime (roughly 3~7 km/s), when the projectile hits the bumper, the projectile and bumper partially melt, and larger extent fragments generate. As the projectile is fragmented and partially melted, damage to the rear wall decreases. Hence, the protection potential of the shield also improves with velocity. In the third region (above 7 km/s), the debris cloud generated from projectile and bumper impact consists of different fractions of solid, liquid, and vapor components. This amount primarily relies on projectile and shield configurations and materials. In such a scenario, the critical particle diameter decreases with increasing velocity in the melt/vaporize range [33].

The shielding performance of FCSP was studied in [34]. The BLC of a specific configuration of FCSP was compared to HCSP, and WS is shown in Fig. 2.5

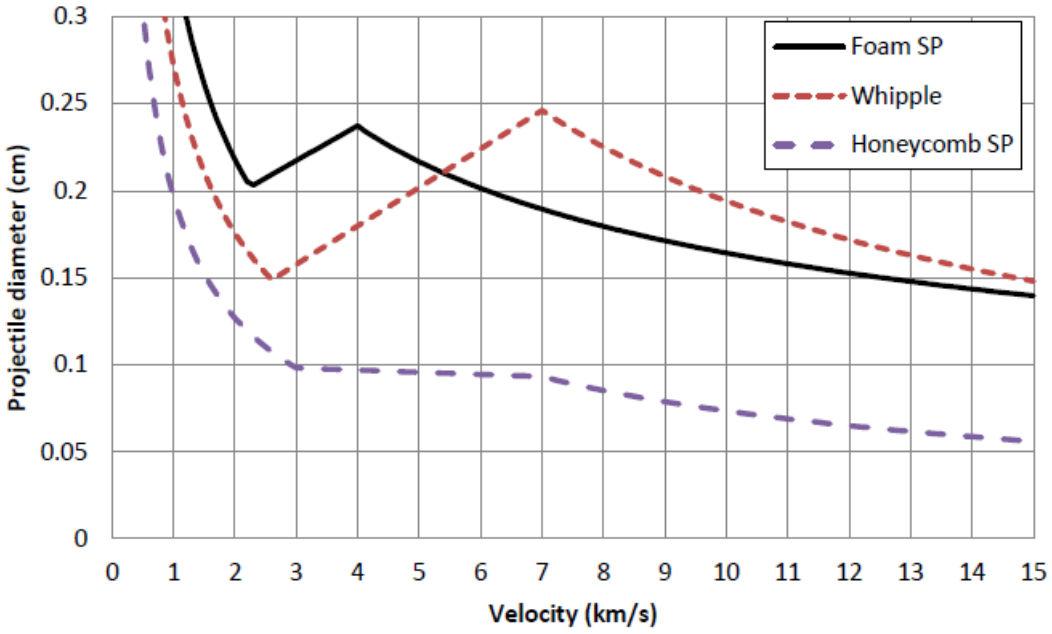

Figure 2.5 Ballistic limitation of honeycomb core, foam core, and Whipple shield [34]

Based on the study, the foam core sandwich panel can provide better protection at 3~5km/s, whereas WS showed more efficiency at higher velocity (6~8 km/s). However, the HCSP performed poorly against HVI due to its channeling effect. A projectile of 1 mm (diameter) at 7 km/s can perforate the HCSP completely.

2.3 Numerical Simulation

2.3.1 Introduction

Numerical simulation acts as a bridge between the theoretical approach and the experimental result of a problem. A numerical method is a mathematical model of any engineering problem and is performed on a computer through code implementation. Numerical simulation is useful for providing a good estimate of experiment results in an efficient manner, as well as for validating hypotheses. Numerical technologies often provide more insightful information that is too difficult to obtain through experimental tests.

There are so many numerical simulations that exist to solve different engineering problems. However, the principle of every numerical simulation works in the same way. The essential step in the procedure is demonstrated below in Fig. 2.6.

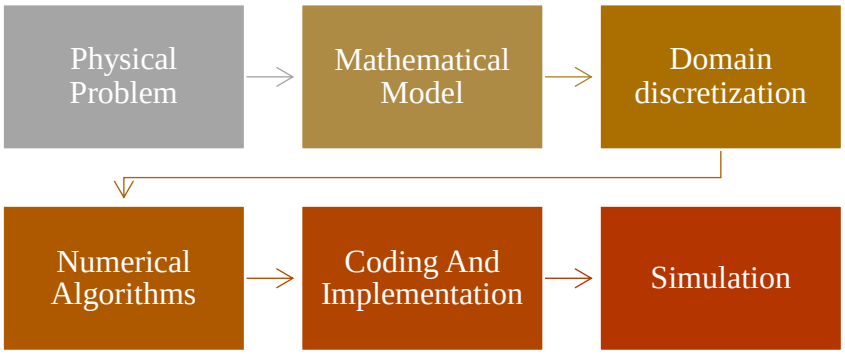

Figure 2.6 Numerical simulation procedure step by step [35]

Mathematical models simplify physical phenomena. Sometimes, a mathematical model makes some assumptions too. This mathematical model expresses a physical model in governing equations with proper initial and boundary conditions. The critical geometry of the problem area must be separated into discrete components to solve the governing equations numerically. Domain discretization forms the computational frame for numerical approximation by representing a continuum problem domain with a finite number of elements. After domain discretization and numerical discretization, the ordinary physical equations can be changed into a set of algebraic equations, ordinary differential equations (ODE), and particle differential equations (PDE), which can be solved using existing numerical routines. Numerical algorithms and domain decomposition move into computer code in some programming languages. Most time-efficient, robust, and accurate computer codes are always getting preference.

There are various method exists that can solve the hypervelocity impact problem. Each method has its strength and weakness in numerical approximation. In the following section, there is a description of the numerical methods that can be utilized to simulate HVI application and their pros and cons. Finally, the numerical approach that was selected for the purpose of simulating the HVI in this thesis is explained.

2.3.3 Finite Element Method (FEM)

FEM was formally introduced in 1960, although the algorithm of FEM appeared before that [36]. Finite element analysis can be carried out using either the Lagrangian or Eulerian formulations. However, the Lagrangian approach is preferred for the simulation of hypervelocity impact due to its ability to handle significant material deformation, large displacement, and material failure and provide a better representation of physical behavior.

Finite element analysis can be divided into two categories: Implicit and explicit. In the context of hypervelocity impact simulation, the FEM analysis uses an explicit formulation. The explicit formulation is a type of numerical solution method that solves problems by advancing the solution in small time increments. The explicit formulation is well-suited for simulating problems with high deformation rates and large strains, such as those encountered during hypervelocity impact events.

Explicit dynamics is a non-equilibrium with the sum of all forces equals mass multiply acceleration. Explicit dynamics is a time-dependent analysis that determines the acceleration of elements. Generally, the mass matrix is considered a diagonal matrix. At first, the accelerations are obtained at the nth steps. After that, the velocity and displacement are assessed at $n + 1/2$ and $n + 1$ steps, respectively. Explicit dynamics require smaller time-step as this method is not entirely stable. The time step must be less than the time taken by a sound wave to travel across an element.

Although FEM explicit dynamic can simulate hypervelocity impact, its efficiency drops dramatically for the hypervelocity impact problem as the elements get extremely deformation (i.e., simulating debris cloud) due to excessive kinetic energy, resulting in poor interpolation accuracy, and the critical time step size is reduced. In contrast, the FEM is able to create a more accurate prediction in a shorter amount of time in regions with reasonable deformation (i.e., simulating bending, bulging of object).

2.3.4 Smooth-Particle Hydrodynamics (SPH)

The SPH is a pure particle-based numerical method. The key idea behind inventing SPH was to simulate an astronomical explosion. SPH method was proposed by Lucy and Gingold in 1977 in their papers [37], [38]. Since the collective movement of those particles is similar to the movement

of a liquid or gas, and it can be modeled by governing equations of the classical Newtonian hydrodynamics, the SPH method uses a bridge between the particles and the Navier Stokes equations, so-called particle approximation. This particle approximation assists in investigating how particles do the transformation of their material properties after the transformation. Particle approximations utilize the kernel function to find a particle's material properties by checking its neighbor particles.

The accuracy of SPH approximation relies on an adequate number of particles within the influence domain and on smooth functions radius (kh). In Fig. 2.7, kh is the radius of the particle circle, and $W(r)$ is the kernel function.

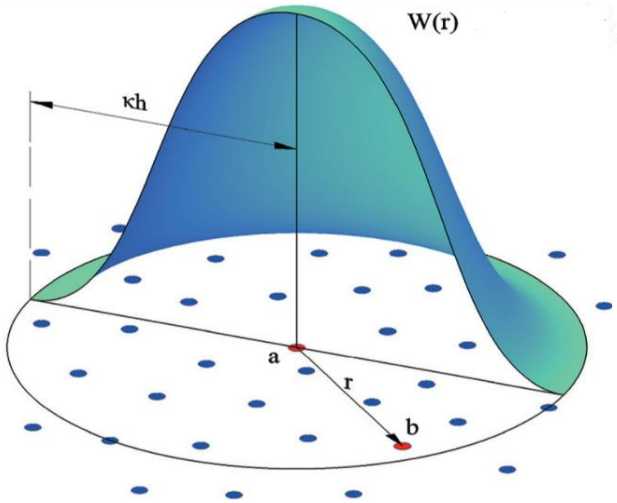

Figure 2.7 The kernel and its domain of influence [39]

2.3.4.1 Mathematical Model of SPH [40]

Basic mathematical function for smooth particle hydrodynamics is,

$$< f(X) \geq \int f(X')W(X - X', h)dX' \qquad (1)$$

$X = (x, y, z)$ is the position of the fixed point.

$X^{'} = (x^{'}, y^{'}, z^{'})$ is the position of the variable point

$< f(X) >$ is the approximate value of the scalar function f

$f(X')$ is the value of the scalar function at the variable point

$W(X - X', h)$ is the kernel evaluated in the position $\left(X - X^{'}\right)$.

Spatial derivative $< \nabla . \mathrm{f(X)} >$ is obtain from derivative function:

$$< \nabla . \mathrm{f(X)} > = \int_{\Omega} f(X') . \nabla W(X - X', h) dX' \tag{2}$$

2.3.4.2 Particle Approximation

Particle approximation is a key aspect to solve problem in continuum domain. In SPH method, whole specimen has been discretized into finite particles which carry individual mass and allocated at individual space. The general expression for particle approximation is,

$$f_i = \sum_{j=1}^{n} m_j \frac{f_j}{\rho_j} W(X_i - X_j, h) \tag{3}$$

Where,

n is number of neighboring particles

f_i is the fixed particle's approximate value

f_j is the neighboring particle's approximate value

m_j is neighboring particle's mass

ρ_j Is the density of neighboring particle

$X_i$is the position of the fixed particle

X_j is the position of the neighboring particle

2.3.4.3 Conservation Equation

Mass conservation of SPH:

$$\frac{D\rho_i}{Dt} = \sum_{j=1}^{n} m_j (\overrightarrow{v_i} - \overrightarrow{v_j}) . \nabla W(X_i - X_j, h) \tag{4}$$

Momentum conservation of SPH:

$$\begin{aligned} \frac{D\overrightarrow{v_i}}{Dt} = \sum_{j=1}^{n} m_j \left[\frac{P_i}{\rho_i^2} + \frac{P_j}{\rho_j^2} \right] \nabla W(X_i - X_j, h) \\ + 2v_i \sum_{j=1}^{n} \frac{m_j}{\rho_j} (\overrightarrow{v_i} - \overrightarrow{v_j}) \frac{(X_i - X_j)}{|X_i - X_j|^2} . \nabla W(X_i - X_j, h) + \vec{g} \end{aligned} \tag{5}$$

Energy conservation of SPH:

$$\frac{De_i}{Dt} = -P_i \sum_{j=1}^{n} m_j \left(\overrightarrow{v_i} - \overrightarrow{v_j}\right).\nabla W\left(X_i - X_j, h\right) + \varepsilon_v + \nabla.q + q_H \qquad (6)$$

Where, $\upsilon_i$is the kinematic viscosity and P is the absolute pressure.

2.3.4.4 Implementation of SPH

SPH is similar to Molecular dynamics and the Direct Simulation Monte Carlo (DSMC). After initialization, it transports the particles, does a cell list for the search, and implies boundary conditions, and the equation of motion has been calculated. After calculation, it moves to another particle. This procedure continues as a loop.

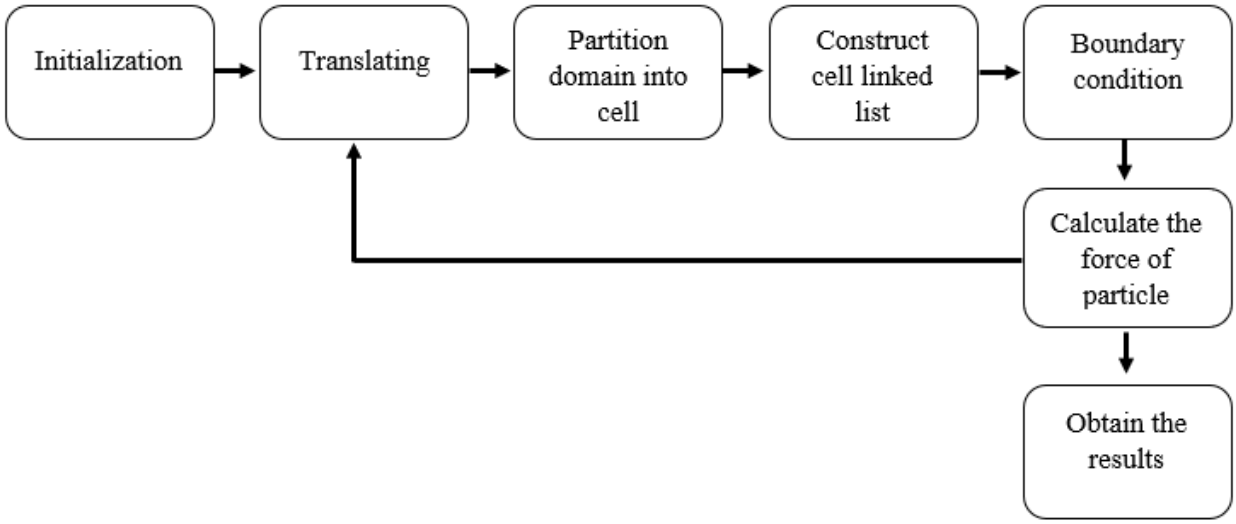

Figure 2.8 Flowchart of SPH method

2.3.4.5 Advantages of the SPH Method

1) A vast range of practical application-solving capabilities:

   SPH has continuously improved and modified, being the oldest meshless particle method. It is quickly approaching its mature stage. SPH has been reaching an acceptable level for solving practical engineering problems. Now SPH simulation is more stable, accurate, and adaptive than before. The SPH method is adequate to work with a considerable range of engineering problems, from discrete systems to continuum systems, from micro to

astronomical scale, and from CFD to CSM. By the SPH method, many exciting applications in the areas related to CFD can be represented; these include [35],

- High-velocity impact.
- Penetration.
- High explosion detonation.
- High compressive flow
- Shock response
- In-compressive flow
- Free surface flow
- Multiple scale simulations coupled with an atomistic method.

2) Unraveled SPH's significant drawbacks:

   No numerical method is able to give us a perfect solution with any difficulties. Some methods are able to simulate specific applications better than others. Despite SPH's ability to compute problems, including high deformation, it still has drawbacks such as tensile instability, numerical fracture, expensive computation cost, and difficulties in employing boundary conditions. Monaghan [41] and other scientists have gradually come up with various unique treatments and numerical corrections so that SPH can replicate physical application more precisely in the SPH model and obey the law of physical numerical as it happens in the practical world. Thus, SPH has reached the most mature numerical algorithm stage to simulate the HVI problem. We can now bring the computational cost to a reasonable stage from our processors' massive development in computational power and parallel processing. However, some minor problems, such as searching for neighboring particles, still need improvement.

3) Mature hydrocode for SPH:

   Some commercial codes (i.e., ANSYS) have already incorporated the SPH processor into their software package with many successful practical allocations. Moreover, the SPH code is composed of most standard SPH techniques and can be easily extended to other variants of SPH by modifying the continuous kernel approximation or discrete particle approximation. AUTODYN is one software that allows us to use SPH hydrocode. The

hydrocode in this software has gone through lots of updates and reached a mature stage where we can rely on it. The code is used in AUTODYN called hydrocode, where the physical equation of mass, momentum, and energy conservation coupled with material description is solved. In AUTODYN, several processors are designed to simulate different model types, such as Lagrange processors for modeling solid continua and structures and Euler processors for modeling gases, fluids, and the significant distortion of solids.

Moreover, hydrocode provides various material models with constitutive equations and material Equations of State (EOS). The EOS includes the linear, shock, polynomial, ideal gas, orthotropic, porous, Tillotson, and PUFF models. Strength and failure models, which are very important for the HVI model, are available as Johnson-cook, Zerrilli-Armstrong, Steinberg-Guinan model, etc. [42].

2.3.5 Discrete Element Method (DEM)

DEM is a meshless approach for numerical simulation that can be employed to simulate HVI problems. In DEM element has been discredited into a large number of small particles. Each particle has its own rotational, positional, and momentum vectors that can be calculated using simple Newtonian physics [43]. Cundall first proposed the DEM method in 1971 to solve the rock mechanics problem; later, in 1985, Williams, Hocking, and Mustoe utilized DEM as a generalized finite element method to simulate engineering problems [44]. DEM is ideal for discrete particle situations such as colloids, granular matters, powders, jointed rock masses, bulk material in storage, and progressive fracture/failure of materials.

In contrast to milling simulations, HVI models require unique considerations. For instance, extensive shock waves generate material state changes and fragmentation. Although DEM is handling large deformation on HVI, it shows significant error in predicting the shock wave generated at HVI. The main reason is that material strength plays a minor role in DEM, which causes the simulation result for HVI to diverge from reality. At high t/D (target thickness – t, projectile diameter - D), debris cloud shape and fragmentation lever are close to experimental results when shock pressure is high. However, the DEM model fails to reproduce the impact phenomena at low t/D when the lower shock pressure [45]. At a low t/D ratio, a rarefaction wave

is reflected off the back end of the target plate and overtakes the compression wavefront traveling through the impactor, attenuating the shock pressures.

2.3.6 Material Point Method (MPM)

Hyper-velocity impact creates large deformation. To do a numerical simulation of the HVI problem, a mesh-based method (e.g., FEM) occurs with mesh distortion, which brings inaccurate results and, in an extreme case, eventual breakdown of the numeric due to element inversion. Thus, the pure grid/mesh method does not suit HVI simulation.

The material point method is an alternative to the pure Lagrangian approach and is well suited to a colossal deformation problem like HVI. MPM method discrete a continuum body into small Lagrangian particles, so-called material point. These material points carry all material information (mass, density, etc.) and initial conditions (velocity, stress, temperature, etc.). Each particle is fixed in a background grid. The grid that is solely utilized to give a place for gradient calculation is often designed to span an area that is required for the simulation.

2.3.7 Mixed Particle and Element Method

Both pure Lagrangian, and Eulerian approaches and meshless methods have pros and cons. Certain methods work better than others for a specific engineering problem due to their ability to compute certain aspects more accurately. As the HVI model has to consider so many effects simultaneously (strength effect, compressed states, contact impact etc.), only the particle method or grid method faces difficulties in calculating HVI more efficiently and accurately. For example, SPH faces numerical fracture and tension instability. FEM deal with extensive element deformation resulting in inaccurate outcomes. Therefore, several scientists argued that combining finite elements and the meshless method may overcome the disadvantages of merely employing the mesh or meshless technique. In addition, we can simulate HVI without incurring significant processing time.

There are two established approaches for simulating various impact events that combine FEM with the meshless method.

1. Coupled FEM-SPH method [46]
2. Hybrid Particle-element method [47]

2.3.7.1 Coupled FEM-SPH Method

Generally, the whole specimen does not experience high deformation in an HVI event. Some areas' elements experience more deformation than others. In such regions, the finite element can be utilized. This approach can reduce the computational cost by lowering the model's total amount of SPH particles. The main idea is to fill the zones with the SPH particles at high deformation risk and set up finite elements for the rest of the specimen. The finite element will be attached to SPH particles. Therefore, the SPH particle can simulate the fragmentation procedure more accurately at a considerable simulation cost. The particles at the coupling interface correspond to the element nodes, and they have the same acceleration as the corresponding unit nodes, with the magnitude of the acceleration determined by both the mass and the force acting on the elements and particles.

However, the contact interface between SPH particles and finite elements is hard to stabilize. Several coupling algorithms have been introduced (johnson's coupling algorithm, Fernandez-Mendez's algorithm, SPH-FEM attachment algorithm, etc.). These algorithms either do not guarantee interface continuity or raise the computational cost much higher than the single SPH method.

2.3.7.2 Hybrid Particle-Element Method (HPEM)

Unlike the coupled FEM-SPH method, the Hybrid particle-element approach makes simultaneous use of particles and elements to model distinct physical effects in all impacting materials. This method has been developed specifically for solving HVI problems by Fahrenthold and Horban [47]. The hybrid method uses the finite Lagrangian element to represent the material strength effect (tension, elastic-plastic shear, etc.) and the Lagrangian particle to represent inertia, compressed states, and contact impact effect. Particles and elements are both used in tandem throughout the simulation for all materials. Thus, no element-to-particle conversions are necessary. Finite elements and particles are employed to compute different aspects of the numerical model. Hamiltonian mechanics provides a systematic method for developing this hybrid numerical technique. The total entropy variable is introduced as Hamiltonian displacement to include

thermomechanical dynamics in the hybrid formulation. Mass, density and entropy per mass were used to compute the particles' pressure and temperature for any chosen EOS.

Body-centered cubic particle parking is employed with eight corner particles creating a hexahedral finite element that is used to represent elastic and plastic strain tensors. The particles of each component represent hydrostatic tension. Element failure is not related to rezoning or mass discard. In reaction to contact impact stresses, particles that are not connected with any intact components are free to flow. All strain energy release related to damage development is accounted for as irreversible entropy creation.

The advantage of the Hybrid particle element method is its smooth integration of the particle method's universal contact-impact capability with lagrangian strength models of the finite element method. However, the disadvantage of the hybrid method is its computational cost as it computes elements and particles in a single core.

New approaches have been developed to improve its performance and computational time. For instance

1. Kernel-free Particle Element Method (KPEM)
2. Energy-based Particle Hydrodynamics (EPH)
3. Membrane Particle-Element Method (MPEM)

2.3.8 Rationale

There will be an assessment of different meshless techniques and their codes using the SPH method in this sub-section. This comparison will aid in selecting the best approaches currently for simulating HVI instances.

- DEM fails to characterize the fragmentation size and replicate debris cloud expansion as close to experimental results. It often miscalculates the shock pressure. These aspects are so crucial for HVI simulation results. If we can't predict the fragment size, velocity, and spreading shape by the DEM method, there is no point in using this method for Hypervelocity impact. Meantime, SPH can predict fragment size, velocity, and shock wave shape within a reasonable efficiency (roughly less than 20 percent of error) [10].

- MPM has a significant drawback called "cell crossing instability" [30]. When the internal force pushes a particle to another cell, it is not a problem where the internal energy is not that high. Yet, the HVI model has a very high internal force among particles. Some improvements have been made to overcome the situation, but the improved model still has some problems, such as boundary conditions where the SPH algorithm mostly overcomes its major disadvantages and gives a closer prediction of the experimental result than the MPM method.

- HPEM is a unique method to simulate the Hypervelocity problem. The primary purpose of developing this method is to reach a lower error rate and boost the computational time than the SPH method. However, this method is at its early stage, where it is going through lots of improvement. Although this method shows some promising results early, we still cannot rely on its results. Besides, the code is not yet available to many researchers. Maybe after a decade or so, HPEM will be used for HVI simulation. But we have recently had to rely on something available and reliable. Thus, the SPH method has become our only choice for HVI simulation, providing a better result than any known method.

Regarding all aspects of the SPH method, its hydrocode and comparison with other existing methods, the SPH method will be the best choice for predicting Hypervelocity impact response. However, the SPH method has high computational costs since the method has to do a neighbor search procedure for all particles in the model at each timestep. In order to reduce the computational cost, finite elements can be filled in the area where the risk of high deformation is lower. The FEM method can simulate with a high degree of accuracy in a shorter time. It is very easy to imply boundary conditions too. Therefore, a combination of the FEM and SPH method will be implemented in the numerical models in this research. An example is presented in Fig. 2.9.

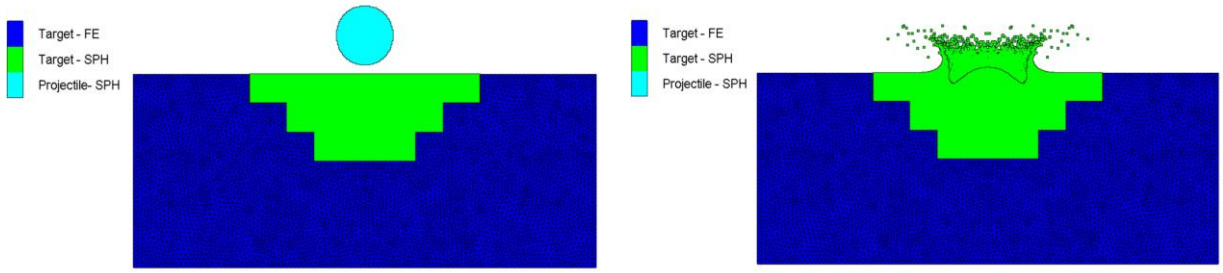

a) Before Impact b) During impact

Figure 2.9 An example of a combined SPH-FEM method to simulate HVI.

2.4 Summary of Chapter

Implementation of multifunctional panels with enhanced MMOD protection capability seems a more weight-efficient alternative than installing HCSP and WS in a satellite. A sandwich panel with a corrugated plate core is a substitute for a Honeycomb core in terms of protection from space debris.

If a material endures extreme deformation, the SPH approach can estimate the situation with a level of precision that is acceptable. Regarding all aspects of the SPH method, its hydrocode, and its comparison with other meshless methods, the SPH method will be the reasonable choice for predicting Hypervelocity impact response. But the computation cost is high for the SPH method.

On the other hand, FEM generally offers a decent harmony between simulation precision and computational effectiveness. However, the accuracy may degrade with higher deformation of elements. A combination of the Meshless method (SPH) and grid-based method (FEM) can be utilized in the CCSP model since they balance each other's weaknesses.

3. METHODOLOGY

The section presents a combination of numerical and experimental research. It explains the development of numerical models and the validation of these models through physical experiments.

3.1 Numerical Model of CCSP

3.1.1 Numerical Simulation Approach

Hypervelocity impact is a complex phenomenon where the material states vary along with extreme temperature and excessive deformation [48]. In such a scenario, meshless methods are widely considered techniques for simulating hypervelocity impact applications. The comparison of different meshless methods in section 2.3.5 shows that the SPH method is capable of accurately predicting extreme deformations and material state changes in hypervelocity impact simulations. However, not all shield components deform at the same rate during hypervelocity impact. In most cases, the projectile, the front facesheet, and some parts of the corrugated core encounter a higher strain rate than the rear facesheet. To address these conditions, both the SPH and FEM methods are employed in this study to model hypervelocity impact with the goal of overcoming the limitations of both methods and reducing computational costs.

Although SPH is superior to other methods in simulating extreme deformation, it suffers from a number of drawbacks, including tensile instability and numerical fractures [49]. Meanwhile, FEM can simulate low deformation models with high accuracy and low computational cost but can't predict high deformation with acceptable accuracy. Therefore, SPH particles can be used for the parts of the model with a greater threat of extreme deformation, and FEM can be implemented in regions with lower deformation, such as the rear facesheet. Besides, a grid-based element (finite element) eliminates the potential of numerical fracture by using SPH particles in the rear facesheet and reducing the overall computation cost.

There are two potential reasons for high tensile stresses (i) Reflection of the initial compression wave from the free surface immediately upon impact or (ii) momentum of the debris cloud dispersed across the rear facesheet occurring later. The numerical fracture may result in unphysical

material spallation from the back surface in the first situation. In the second case, a significant portion of the back wall may bulge. In both circumstances, a preliminary drawback of SPH (numerical fracturing) may result in underestimating a shielding system's ballistic performance [13]. Hence, employing finite elements rather than SPH particles to discretize the rear wall/rear facesheets is more advantageous when the strain rate is lower. However, if the impact load of the debris cloud has enough energy to generate greater perforations in the back wall, it is necessary to fill the part with SPH particles.

Nevertheless, calibration and validation procedures are necessary to ensure the numerical model can produce reasonable results for hypervelocity impact at a reasonable computation cost. The calibration and validation of the numerical model for the CCSP are discussed in Section 3.1.3 and Section 3.3, respectively.

3.1.2 Material Model

The material model is one of the critical aspects of every numerical simulation. The three components of a material model are commonly required to simulate an HVI event: the Equation of State (EOS), the strength model, and the failure model of the material.

In general, EOS demonstrates the relationship between the values of the pressure, volume, and temperature of a quantity of a particular substance. EOS is required to model the effects of the shock wave, high strain rates, and changes in volume due to discontinuities in density, pressure, and temperature on the properties of isotropic continua such as those considered in this study [50].

The strength model correlates the stresses applied to a material and the strains that these stresses cause. At high velocities, the collision of two materials can result in the generation of intense heat, a change in strain rate, and a potential transition of the material's state to liquid or vapor, altering its deformation behavior [51]. In such a scenario, the strength models characterize the deformation behavior of ductile metals under these extreme conditions.

During hypervelocity impact, the shock wave instantly triggers microcracking in the material, rendering it unable to withstand tensile stresses beyond its local tensile strength. The failure model of material is employed to simulate the phenomena of continuous degradation of material

properties [52], [53]. The model calculates the initiation of failure followed by the post-failure response.

In recent decades, various material models have been developed to depict the macroscopic behavior of different materials under dynamic loads. The following section outlines the material models utilized in this thesis.

3.1.2.1 Material Model for Components of the CCSP

Aluminum alloys are often utilized in the aerospace industry due to their high strength-to-weight ratio. In spacecraft surface structures and satellite subsystems, different types of aluminum alloys (Al6061, Al2024, and Al7075) have been used [54]. In this study, Al6061 – T6 alloy was utilized to construct the CCSP (Front and rear face-sheet and corrugated core).

Table 3.1 displays the parameters of the Al6061-T6 material model used in this study [52]. This model has been successfully utilized and validated for its accuracy in previous studies conducted by the UM-ORDER Group [13] [55].

The Mie-Gruneisen Equation of State (EOS) connects specific energy, hydrostatic pressure, and local density of the Al6061-T6 alloy to shock loading in the following form:

$$p = p_H + \Gamma\rho.(e - e_H) \quad (1)$$

Where $e,\ p,\ \rho$ are specific energy, pressure and density of the material respectively. e_H and p_H are specific energy and reference pressure obtain from material's shock Hugoniot. Γ is Gruneisen gamma.

The Johnson-Cook (JC) plasticity model, which incorporates hardening law, high strain rate and high temperature, is employed as the strength model for Al6061-T6 to model its yield and work hardening behavior. The yield stress, Y of material is demonstrated as

$$p = \left[A + B.\varepsilon_p^n\right].\left[1 + C.ln\dot{\varepsilon}_p\right].[1 - T_H^m] \quad (2)$$

Where T_H is homologous temperature $T_H = [\frac{T-T_{room}}{T_{melt}-T_{room}}]$, and ε_p, $\dot{\varepsilon}_p$ are effective plastic strain, normalized effective plastic strain rate respectively. A, B, C, n and m are initial yield strength, hardening constant, strain rate constant, hardening exponent and thermal softening exponent.

The Johnson-Cook damage/failure model, which is accurate for metallic materials, is used as the failure model for Al6061-T6. Pressure, strain rate, and temperature determine dynamic fracture strain in this model:

$$\varepsilon^f = [D_1 + D_2 \,.\exp(D_3.\sigma^*)].\left[1 + D_4 \,.\, ln\left|\dot{\varepsilon}_p{}^*\right|\right].[1 + D_5 \,.\, T_H] \qquad (3)$$

Where $\dot{\varepsilon}_p$ and σ^* are dimensionless strain rate and pressure-stress ratio respectively. $\sigma^* = \sigma_m/\bar{\sigma}$, where σ_m and $\bar{\sigma}$ are the average of the three normal stresses and von Mises equivalent stress. $D_1 - D_3$ are failure strain parameters and $D_4 - D_5$ are the strain rate and temperature parameters, correspondingly.

Table 3.1 Material model of Al6061-T6

Material model	Parameter	Value	Unit
Mie-Gruneisen EOS	Reference density	2.703	g/cm^3
	Gruneisen gamma	1.970	
	C_0	5240	m/s
	S	1.400	
	Ref. temperature	300	K
	Specific modulus	885	J/kgK
Johnson-Cook Strength model	Shear modulus	26000	MPa
	Yield stress	324	MPa
	Hardening constant	114	MPa
	Hardening exponent	0.420	
	Thermal softening Exponent	1.340	
	Melting temperature	925	K
	Ref. strain-rate	1	s^{-1}
	Strain rate constant	0.002	
Johnson-Cook Failure model	Damage constant, D_1	-0.770	
	Damage constant, D_2	1.450	
	Damage constant, D_3	-0.470	
	Damage constant, D_4	0.000	
	Damage constant, D_5	1.600	
	Melting temperature	925	K

3.1.2.2 Material Model for Ballistic Fabric in Inserts

Due to its high strength and resistant properties, basalt fabric has received a lot of attention in recent decades. Besides excellent mechanical properties, the competitive price and good environmental adaptability of basalt fabric give the potential to replace existing glass fiber composite in the field of high and new technology, such as aerospace, ship, and vehicle [56]. The orthotropic EOS model is used to imply the woven nature of basalt fabric. The material stress/strain

strength model and failure model are employed to present the material properties of basalt fabric. The material model parameters of basalt fabric are detailed in Table 3.2 [57],[58].

Table 3.2 Basalt fabric material model

Material model	Parameter	Value	Unit
EOS – Orthotropic	Reference density	2.800	g/cm^3
	Stiffness	Stiffness matrix	
	C11	$4.798137 \cdot 10^6$	KPa
	C22	$4.892893 \cdot 10^6$	KPa
	C33	$4.878951 \cdot 10^6$	KPa
	C12	$1.800238 \cdot 10^6$	KPa
	C23	$1.807145 \cdot 10^6$	KPa
	C31	$1.781561 \cdot 10^6$	KPa
	Material Axis	X-Y-Z space	
	Volume Response	Polynomial	
	Bulk modulus	$2.816430 \cdot 10^6$	KPa
	Parameter T1	$2.816430 \cdot 10^6$	KPa
	Ref. temperature	300	K
	Specific Heat	840	J/KgK
Strength model – Elastic	Shear modulus	5.0	KPa
Failure model – Material stress/strain	Default value from AUTODYN		

3.1.3 Calibration Procedure

This subsection aims to present the calibration procedure for finding the SPH particle size, which allows getting acceptable accuracy from the numerical simulation. The accuracy of numerical simulation improves as the number of SPH particles increases until it reaches a specific threshold (convergence). When the model reaches its convergent point, adding more SPH particles has less

effect on the outcome other than increasing the computing cost. Hence, the convergence of the numerical test result permits determining the appropriate SPH particle size for modelling hypervelocity impact on the CC panel with an acceptable level of accuracy and a satisfactory computational cost.

The experimental results of a hypervelocity impact on a Whipple shield were used to determine the SPH particle size needed for convergence in the numerical simulation. The WS configuration and its specifications are shown in Fig. 3.1 and Table 3.3, respectively. This experiment was conducted by UM-ORDER Group using the hypervelocity impact facility in University of New Brunswick.

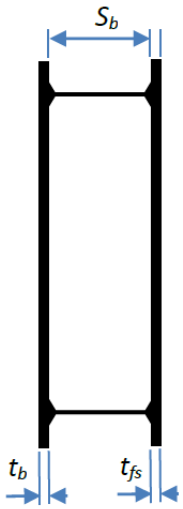

Figure 3.1 The WS configuration used for the model calibration.

Table 3.3 Parameters of the WS experiment

Parameters	**Value**
Bumper thickness, t_b	1 mm
Facesheet (rear wall) thickness, t_{fs}	1.25 mm
Material	Al6061-T6
Projectile shape	Spherical
Projectile radius	3 mm
Projectile particle velocity	6641m/s
Standoff distance, S_b	50 mm

The outcome of the HVI test on WS is shown in Fig. 3.2

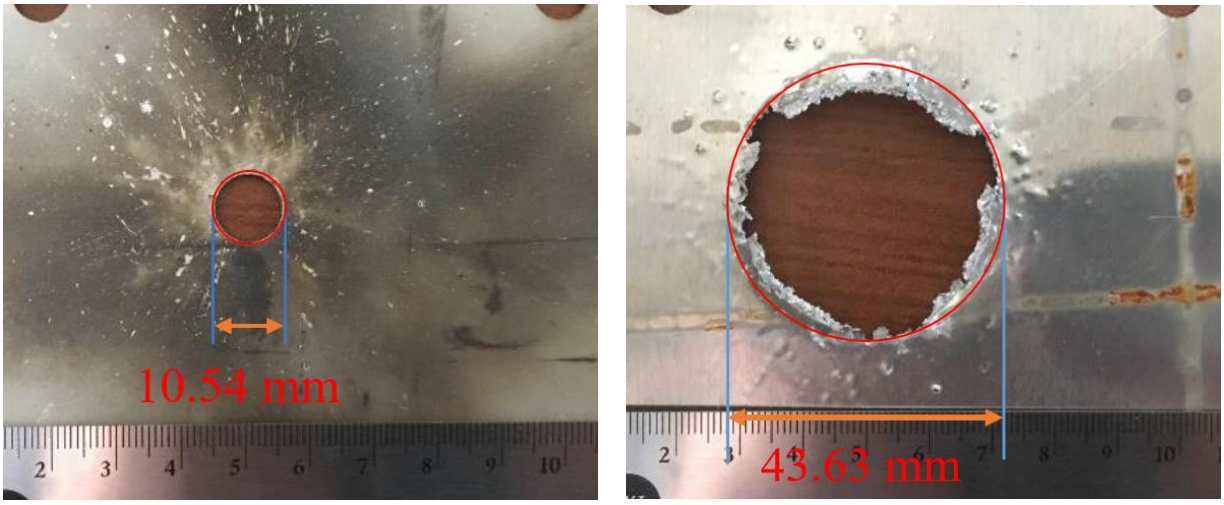

a) Hole size in Bumper

b) Hole size in rear wall

Figure 3.2 HVI test outcome a) bumper (back side view); b) rear wall (back side view)

This study simulated 7 numerical models of the hypervelocity impact test setup, each with varying SPH particle sizes (0.5 mm, 0.4 mm, 0.2 mm, 0.1 mm, 0.09 mm, 0.08 mm, and 0.07 mm). All parameters, except particle size, were kept constant across models. The simulation results were compared to experimental data (size of impact hole in the bumper and rear wall) to determine the most accurate particle size. The comparison between the numerical models and experimental data are presented in Table 3.4 and 3.5.

The convergence of the numerical results to experimental data on the size of the impact holes in the bumper and rear wall is achieved as the SPH particle size decreases from 0.5 mm to 0.07 mm. The summary of this convergence analysis is illustrated in Fig. 3.3.

Table 3.4 Comparison of experimental and numerical data for HVI on WS (using perforated area)

	Numerical Data							**Test Data**
Particle size, mm	0.5	0.4	0.2	0.1	0.09	0.08	0.07	
Bumper hole size(±0.5mm)	13.83	14.49	12.11	11.38	11.62	11.16	11.04	10.54
Error (%)	31.21	37.4	14.89	7.9	10.2	5.8	4.7	--
Rear wall hole Size(±0.5mm)	49.01	49.61	48.91	41.6	44.72	44.34	42.62	43.63
Error (%)	12.33	13.7	12.1	4.6	2.4	1.6	2.3	--

While it may be more cost-effective from a computing standpoint to use larger particle sizes in a model, the simulation outcomes may be subject to more significant errors (> 20%). Based on the diagram in Fig. 3.3, the error percentage decreases with particle size, proving that the particle size was approaching a point of convergence. The error rate between experimental and numerical results achieves a reasonable level (i.e., less than 10%) when the particle size is 0.1 mm or below.

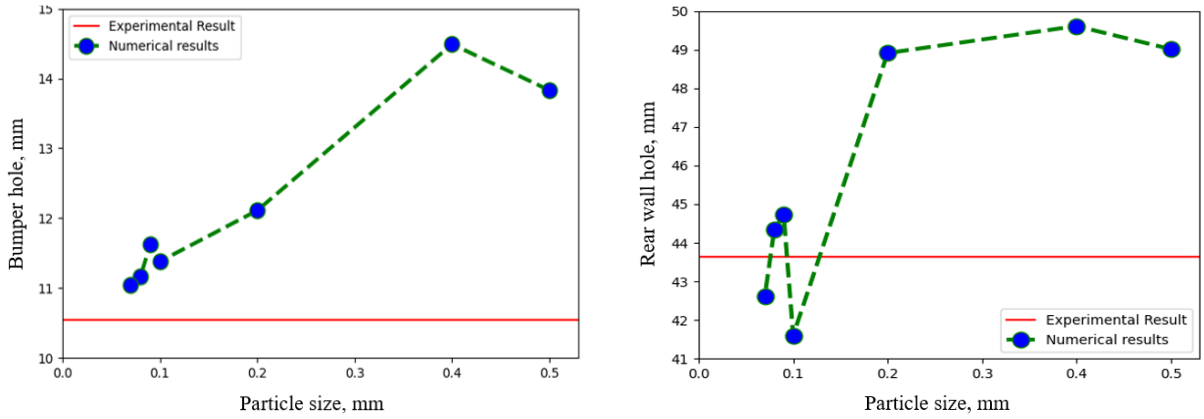

a) b)

Figure 3.3 Convergence of numerical results: a) impact hole in the bumper, b) impact hole in the rear wall

A similar analysis was conducted for the shape of the debris cloud. If a model is filled with a sufficiently small particle size that can simulate acceptable accuracy (i.e., > 10% error), the numerical model can generate a similar shape of debris cloud like an experimental test. The shape of the debris cloud during the physical test was utilized to compare the numerical accuracy of different particle sizes.

The numerical and physical test data were compared based on the average velocity of the debris cloud expansion. The latter was evaluated based on the position, and lateral expansion of the debris cloud at 4.6 μs after the projectile struck the bumper.

Table 3.5 demonstrates larger SPH particle sizes (e.g., 0.5 – 0.2 mm) generate the simulation with a higher error. The accuracy improves in direct proportion to the decrease in particle size. However, error converges as particle size decreases. Fig. 3.4 illustrates the debris cloud expansion simulated with 0.5, 0.1, and 0.07 mm SPH particles and at physical test. 0.1 mm particles mimicked debris cloud expansion with less than 5% error, and 0.07mm SPH particles simulated HVI with less than 3% error.

Table 3.5 Comparison of experimental and numerical data for HVI on WS (using debris cloud)

	Numerical Data							Test Data
Particle size, mm	0.5	0.4	0.2	0.1	0.09	0.08	0.07	
Ave. V_x of debris cloud expansion, km/s	5.049	4.950	5.295	5.607	5.540	5.562	5.707	5.864
Error (%)	13.88	15.55	9.7	4.36	5.55	5.51	2.66	--
Ave. V_y of debris cloud expansion, km/s	4.927	4.457	4.884	5.106	5.171	5.392	5.405	5.273
Error (%)	6.66	15.47	7.36	3.17	1.93	2.26	2.51	--

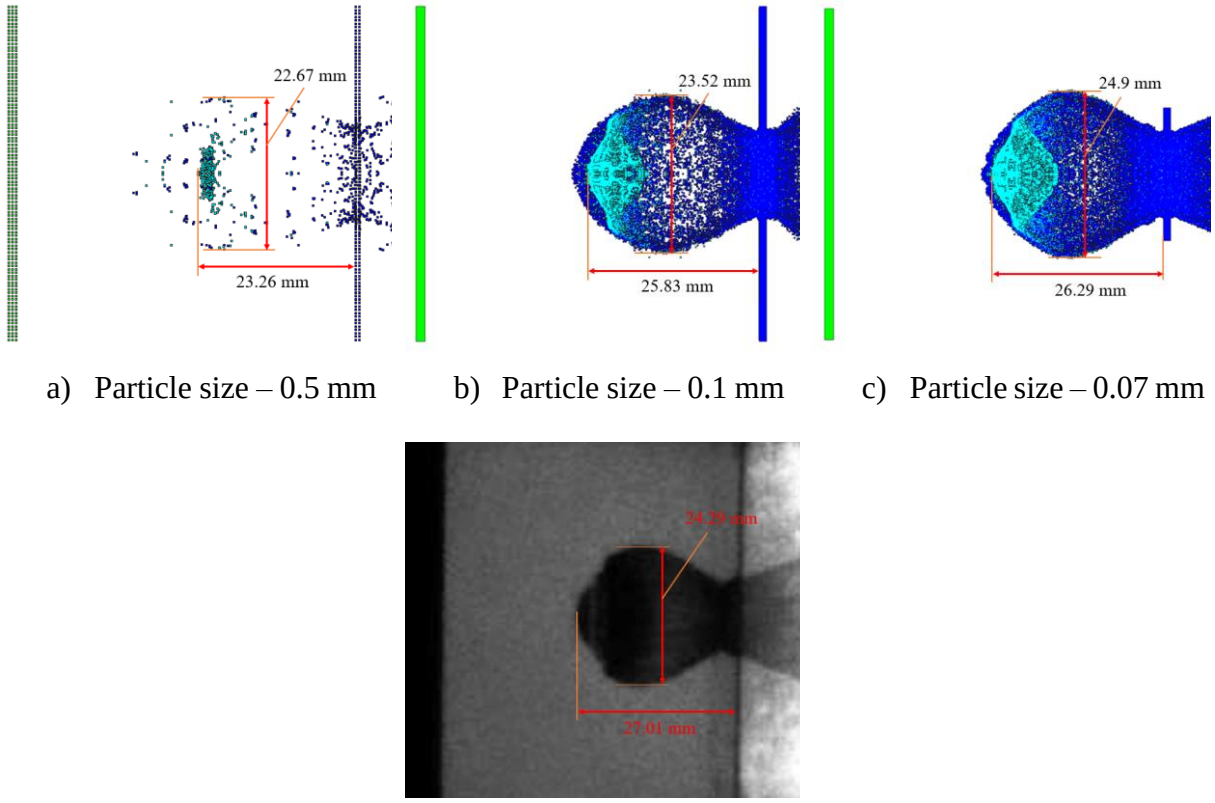

a) Particle size – 0.5 mm b) Particle size – 0.1 mm c) Particle size – 0.07 mm

Physical Test

Figure 3.4 Comparison of debris cloud shape from the numerical and experimental model with different particle sizes (0.5,0.1, and 0.07)

The calibration analysis gives a range of SPH particle sizes for the CCSP model, which is suitable for the hypervelocity impact simulation. For the facesheets thickness of 1 mm, SPH particle sizes of 0.07 mm to 0.1 mm showed results comparable with the experimental data. Other smaller SPH sizes were also studied. For instance, 0.05 mm SPH particle increased the computation cost

excessively without improving the accuracy appreciably. Hence, the SPH particle sizes ranging between 0.07 mm and 0.1 mm were chosen due to the balance between computational cost and accuracy in the form of conformity to the experimental data. Previous researchers selected a similar particle size range [59] [60].

Thus, the above analysis determined the acceptable range of SPH particle sizes for the CCSP model, resulting in a simulation with sufficient precision and reasonable computation costs. Further numerical studies were conducted based on these findings.

3.1.4 Setup for Numerical HVI Testing

This study was conducted on a CCSP with a triangular corrugated plate core. Fig. 3.5 illustrates the setup for the numerical HVI testing of the selected CCSP configuration. The facesheet and core thicknesses were selected based on the conventional sandwich panel for the robotic Earth observations satellite. Both facesheet had the same thickness in a 1.0 – 2.0 mm range, and the core thickness was set at 42 – 44 mm, depending on the facesheet thickness. The thickness of the corrugated plate ranged from 0.5 to 0.8 mm. The simulation domain included a spherical projectile with a diameter ranging from 1 mm to 6.0 mm, impacting the CCSP at 6.5-7 km/s. The vertex angle of the triangular core in the study varied from 45° to 90°.

The 3D model was utilized since the 2D model could not be applied to conduct a proper investigation on CCSP as axisymmetric does not apply to corrugated geometrics. Due to the geometry of the corrugated core, the model could utilize only one plane (X-Z) of symmetry to reduce computing costs. The geometry of the computational domain was adjusted for each configuration modeled to balance the accuracy of the predictions with the time it takes to run simulations.

Both SPH and FEM were employed for the numerical model. Since the deformation of the rear facesheet was anticipated to be much lower than other parts', the rear facesheet was modeled using the finite elements. The other parts of the model, including the front facesheet, projectile, and corrugated core, were modeled using SPH particles to accurately represent their extensive deformation and fragmentation.

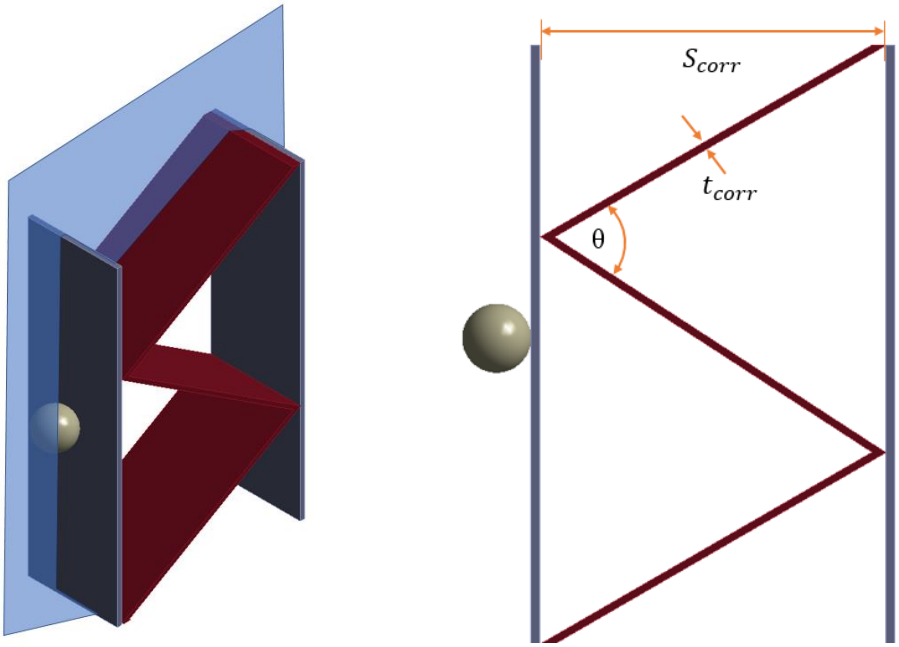

a) b)

Figure 3.5 a) X-Z plane of symmetry for the numerical model; b) side view of the setup model

The size of SPH particles was individually chosen for each component to reduce the simulation duration. Based on the calibration study of SPH particles, presented in section 3.1.3, the projectile and front facesheet were filled with 0.07 mm SPH particles, while the CC plate was filled with 0.1 mm particles. When a projectile hits the front facesheet at hypervelocity, a debris cloud is generated due to the interaction of the strong shock waves with the free boundaries of both the projectile and front facesheet. Fine SPH particle size (0.07mm) was used for accurate simulation of the debris cloud. On the other hand, a corrugated core experiences a lesser deformation than the front facesheet and projectile and contributes less to the debris cloud. Therefore, using a slightly larger particle size (0.1 mm) for the corrugated core allows for faster simulation while still maintaining accuracy.

The proposed CCSP is expected to withstand the impact of hypervelocity debris particles without perforating the rear facesheet, which is expected to only bulge. Therefore, it was proposed to model the rear facesheet using finite elements. The element size of the rear face sheet was selected to be 0.2 mm. Lagrangian finite element models may tangle and interpenetrate between elements nodes due to substantially deformed meshes in HVI simulation. The deformation of meshes might lead to the discretization formulation failing, which would lower accuracy. Therefore, the simulation must let the element nodes "erode" at significant strain.

The erosion parameters prevent the finite elements from deforming when particular criteria are satisfied, such as strain (geometrical or plastic), computational time step, or failure model that are utilized in the study. When the erosion parameter removes nodes' mass, energy and momentum to stabilize the numerical model, AUTODYN code attempts to count for eroded nodes' mass and energy. There is still some level of accuracy loss. Hence, the erosion factor must be contained within a specific range to 1) balance computational cost and accuracy; 2) produce reasonable numerical data that is comparable to experimental results. The simulations were conducted with an erosion strain of 1.0, following the conclusion in the paper [13] that utilized the same material model and impact conditions. The numerical model was simulated using the AUTODYN 2021 R2 software. Parallel processing was utilized to enhance computational efficiency, as compared to the traditional single CPU configuration, as described in [61]. In order to define the interaction between the various parts (Lagrangian element and SPH particle) of the model, "Lagrange/Lagrange" option was chosen. This option sets up impact/slide contacts between Lagrangian Parts (Parts using an SPH solver, Lagrange, Beam or Shell). AUTODYN offers 2 types of Lagrange/Lagrange interaction (contact) methods: 1) Gap contact 2) Trajectory contact. When an SPH part is present in the model, the Trajectory contact approach does not allow for parallel processing. Therefore, Gap contact was used to develop the model. In the Gap contact method, each surface part is surrounded by a contact detection zone. The gap distance should exist between the outside surfaces of the components in contact [62].

Two different computational resources were used to develop and simulate the model. To develop the model, Intel(R) Xeon(R) Processor E5-2470 @ 2.30Ghz with 8 cores and 64 GB RAM desktop had been employed. The system had 64-bit Windows 10 operating system. The numerical model in this research was simulated using a High-Performance Computing (HPC) system with a 2.10 GHz Inter(R) Xeon(R) Gold 6230R CPU and 96 GB RAM, as detailed in [63]. The HPC system operated on CentOS Linux with SLURM resource management. Each model contained 100K to 300K finite elements and 300K to 1000K SPH particles, depending on its configuration. Simulation time ranged from 7 to 18 days, depending on the number of SPH particles and finite elements in the model.

3.2 Physical HVI Testing of CCSP

Physical examinations are essential for HVI research fields. Experiments were conducted to evaluate the effectiveness of the proposed CCSP configuration against a 6 mm aluminum projectile at 7 km/s and validate the numerical models. The following subsections discuss the specimens, HVI test setup, procedure and obtained results.

3.2.1. CCSP Specimens

Three specimens were fabricated and tested. The test specimen schematic is illustrated in Fig. 3.6. The first and second specimens were equipped with lightweight foam prismatic ballistic inserts that had two pairs of evenly placed basalt fabric layers (Fig. 3.6). The third specimen was tested without inserts. The CC thickness of all three specimens, S_{core} was 40 mm.

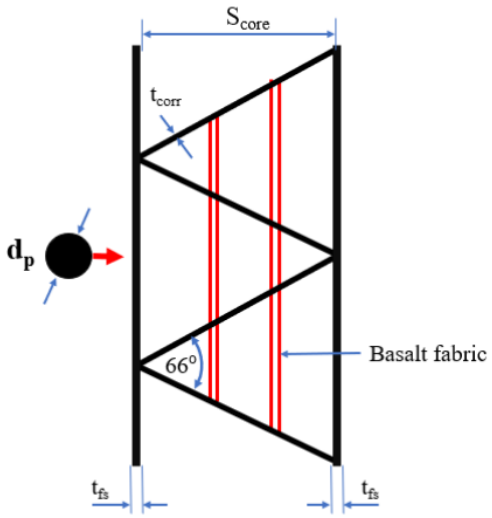

Figure 3.6 Configuration of the CCSP for physical test

Aluminum facesheets measuring 120x120 mm were cut from an Al6061-T6 sheet using a waterjet cutting machine. The first specimen had facesheets that were 2mm thick, while the second and third specimens both had face sheets with a thickness of 1mm. The corrugated core was made from an Al6061-T6 sheet that was 0.8 mm thick. Fig. 3.7 is demonstrated the geometric layout of the facesheet and corrugated core.

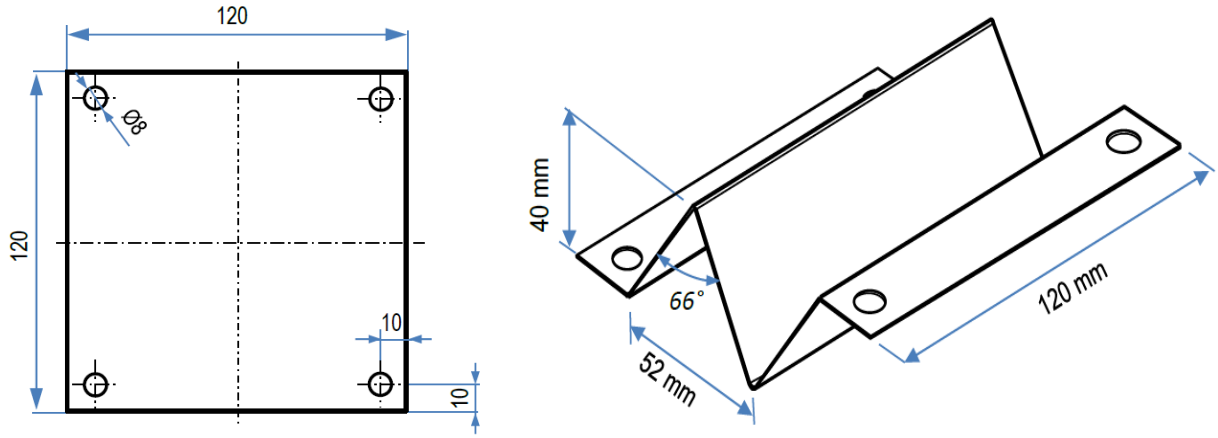

a) Dimension of facesheets b) Dimension of Corrugated core

Figure 3.7 Dimension of specimens of the CCSP

These ballistic inserts were fabricated from lightweight polymeric foam in the shape of a triangular prism fitting the dimensions of the empty space within the corrugated plate core. Two double layers of high-strength basalt fabric (with a density of 2.803 g/cm^3 supplied by McMaster-Carr) were distributed evenly within the insert, as shown in Fig. 3.8. Each basalt layer had a thickness of 1.2 mm. The light foam served only one purpose: to keep the basalt layer in place.

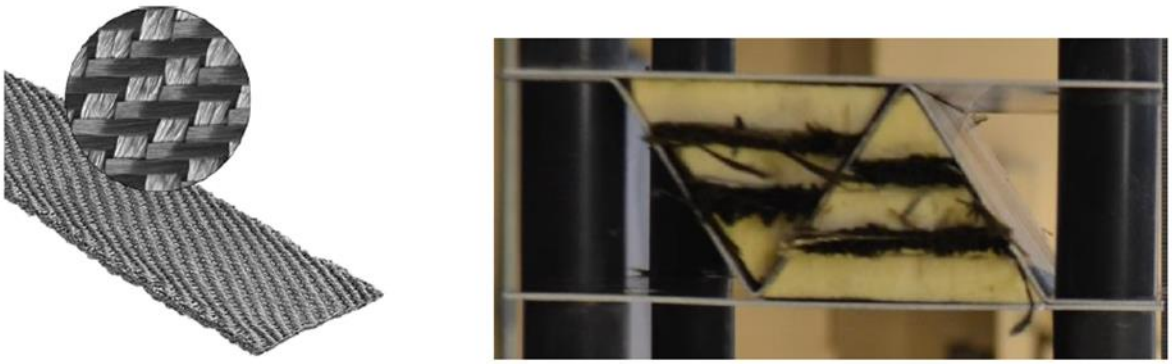

a) b)

Figure 3.8 Basalt strip (a) and specimen assembly with ballistic inserts (b)

3.2.2. Physical HVI Tests Setup

The hypervelocity experiments were carried out at the University of New Brunswick facility in Fredericton, New Brunswick, using a two-stage light gas gun shown in Fig.3.9. An ultra-high-performance camera with a 1.2-megapixel resolution and frame rates of around 200 million frames

per second was used in the test to record the impact reaction at hypervelocity. A high-intensity flashlight was placed as backlighting, and the camera was set perpendicular to the projectile velocity vector.

a) b)

Figure 3.9 a) Two-stage light gas gun b) Target tank on the right and blast tank on the left of the image

A test fixture was designed to hold the specimens securely in place for the HVI testing. Fig. 3.10 includes a drawing of the test fixture along with its measurements. An aluminum witness plate, 0.8 mm thick and measuring 120x120 mm, was cut from an Al6061-T6 sheet using a waterjet cutting machine. This plate was positioned 50 mm away from the rear facesheet of the panel with the purpose of evaluating the extent of damage to components located behind the panel in the event of full perforation.

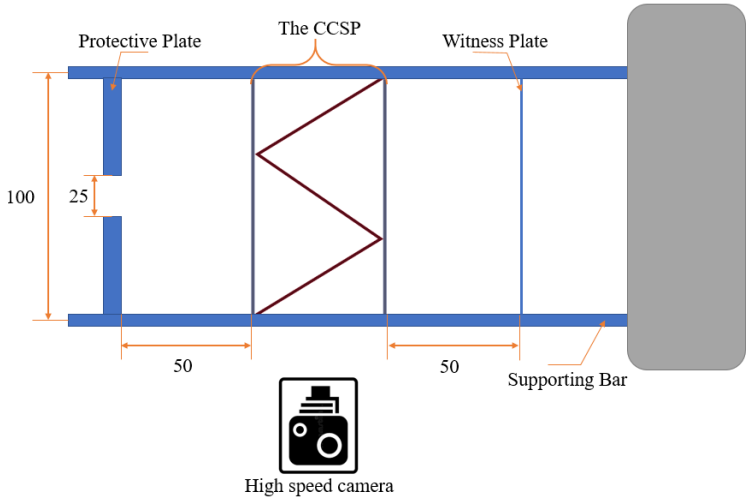

Figure 3.10 HVI Tests Setup

The following procedure was used to conduct testing. First, the test fixture was assembled to include the witness plate, test specimen, and protection plate. The test fixture was then placed into the testing chamber after being mounted to the base plate. Finally, the target was disintegrated following a hypervelocity shot with a 6 mm projectile traveling at around 7 km/s.

3.2.2. Physical HVI Tests Outcome

The HVI test data, including the specimen configuration, projectile impact speed and test outcome for each test, are listed in Table 3.6.

Table 3.6 HVI tests data

Test #	**t_{fs}, mm**	**t_{corr}, mm**	**S_{core}, mm**	**AD*, Kg/m^2**	**V_p, Km/s**	**Ballistic inserts**	**Outcome***
1	2	0.8	40	21.66	6.625	Yes	NP
2	1	0.8	40	16.09	6.625	Yes	NP
3	1	0.8	40	9.41	6.559	No	P

(* AD = Areal Density; P = Perforation; NP = No Perforation)

The first and second test specimens were similar with the exception of the thickness of their facesheets. Test #1 used a facesheet of 1.0 mm thickness, while Test #2 utilized a facesheet of 2.0 mm thickness. Fig. 3.11 and 3.12 present the HVI test setup and the test outcome for specimens #1 and #2, respectively. The rear facesheets of the specimens showed evidence of bulging, with specimen #2 exhibiting a significantly higher degree of bulging compared to specimen #1. No perforations were observed. The witness plates remained unmarked, with no evidence of impact.

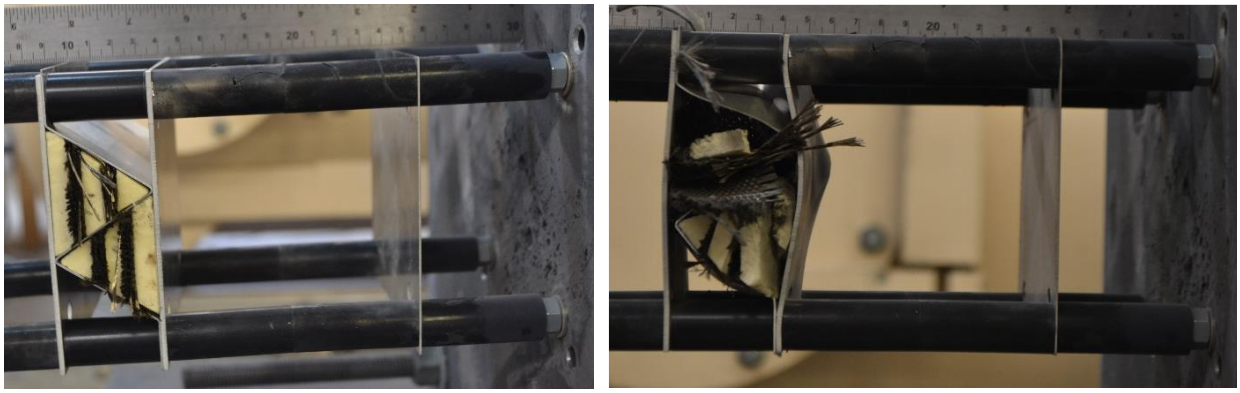

a) Setup for Specimen #1 b) Specimen #1 after the test

Figure 3.11 Specimen #1 a) before b) after experimental test

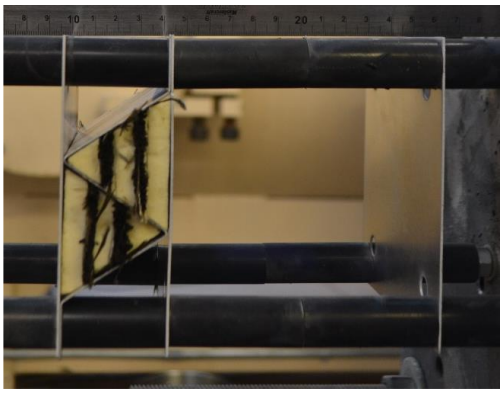

a) Setup for Specimen #2

b) Specimen #2 after the test

c) Rear facesheet after the test

Figure 3.12 Specimen #2 a) before b) after experimental test

When the projectile hit the front facesheet, it caused fragmentation in the form of a debris cloud that was split into two streams by the oblique corrugated plate and traveled towards the rear facesheet, creating two holes and causing several pin-sized penetrations on the witness plate. Fig. 3.13 and 3.14 show the splitting of the debris cloud and damage to specimen #3, respectively. Specimen #3 was perforated with a formation of two large holes on the rear facesheet during the HVI.

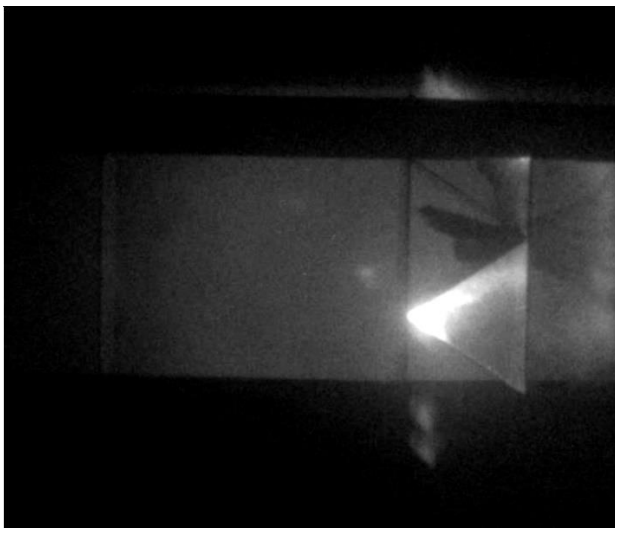

Frame 8, t=16.121μs

Frame 9, t=20.697μs

Figure 3.13 Image of debris cloud at 16.12μs and 20.697μs

a) b)

Figure 3.14 Test #3 outcome: damage in rear facesheet (a) and witness plate (b)

In summary, the corrugated plate has a significant impact on the dispersion and interaction of the debris cloud with the rear face sheet. The use of ballistic inserts allowed to improve the protective performance of the CCSP.

3.3 Comparison of Numerical and Physical HVI Test Data

In this section, the study was conducted to validate the numerical model of the CCSP by the experimental results. It is necessary to validate the numerical model with experimental data to confirm that it can accurately simulate the impact of HVI on the CCSP. The size of the front and rear facesheet hole and damage area were used as qualitative and quantitative parameters to compare numerical and physical test data for specimens #1, #2, and #3, outlined in Table 3-6.

3.3.1. Analysis of Test #1 Data

In Test #1, a 6 mm projectile impacted specimen #1 at 6.625 km/s. The facesheets were 2 mm thick. The point of initial impact contact was identified as 0.8±0.1 mm below the valley of the corrugated core, based on the image captured by the high-speed camera. The physical test of Specimen #1 during HVI is presented in Fig. 3.15. During the physical test, specimen #1 was not fully penetrated by the projectile resulting in no perforation of the rear wall.

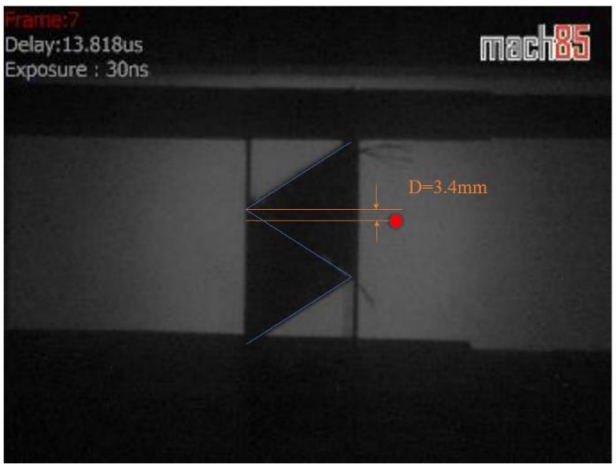

(a)

(b)

(c)

Figure 3.15 Test #1 outcome: a) Image of Specimen #1 at 13.818 µs; b) Image of Specimen #1 at 54.972 µs; c) Rear facesheet damage (front view)

The FEM was utilized to model the rear facesheet of the specimens based on the experimental data. The components that underwent perforation and fragmentation, including the front facesheet, projectile, and corrugated core, were simulated using SPH particles. To achieve a balance between computational cost and numerical accuracy, a meticulously determined SPH particle size of 0.07 mm was utilized in the modeling of the front facesheet and projectile, due to their crucial role in determining the characteristics of the resulting debris cloud.

Since the corrugated core and basalt layers have a limited impact on the debris cloud, an SPH particle size of 0.1mm was used to model these regions. To reduce the overall number of SPH particles and computational costs, the parts of the sandwich panel that had no interaction with the

projectile or debris cloud were omitted from the numerical model. Figure 3.16 presents the numerical simulation of specimen #2.

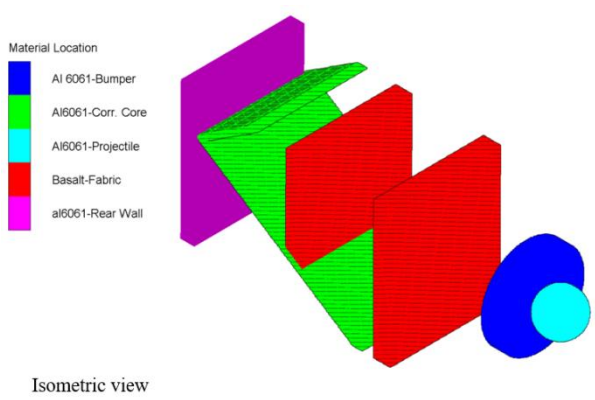

(a) Numerical model of Specimen #1

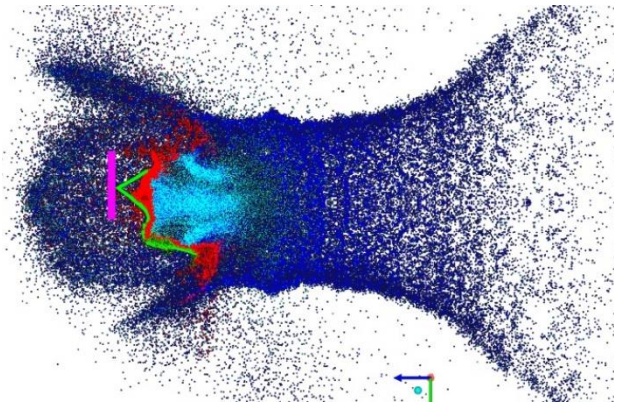

(b) During HVI at 19 µs

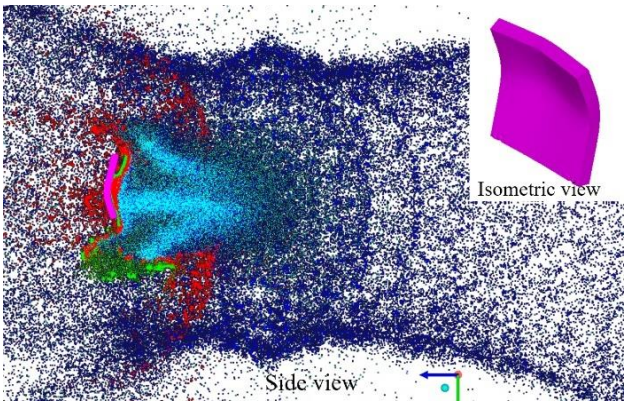

(c) After completing the simulation (at 40 µs)

Figure 3.16 a) Numerical model of specimen #1; b) The impact reaction at 19 µs; c) Deformation of the rear wall after the HVI.

The rear facesheet of specimen #1 experienced minor bulging during the HVI. However, no perforation was observed in the physical experiment. The numerical model also replicated this result, showing no perforation in the rear facesheet. Test #1 successfully validated the numerical model with an acceptable margin of error.

3.3.2. Analysis of Test #2 Data

Specimen #2 was similar in setup to specimen #1, with the exception of its facesheet thickness, which was 1 mm. During the experimental test, a 6 mm projectile impacted the front facesheet in the normal direction at a speed of 6.625 km/s. The point of impact was captured by a high-speed

camera and determined to be approximately 2 mm below the vertex of the triangular corrugated core, as shown in Fig. 3.17 (a). The rear facesheet experienced substantial bulging but remained imperforated.

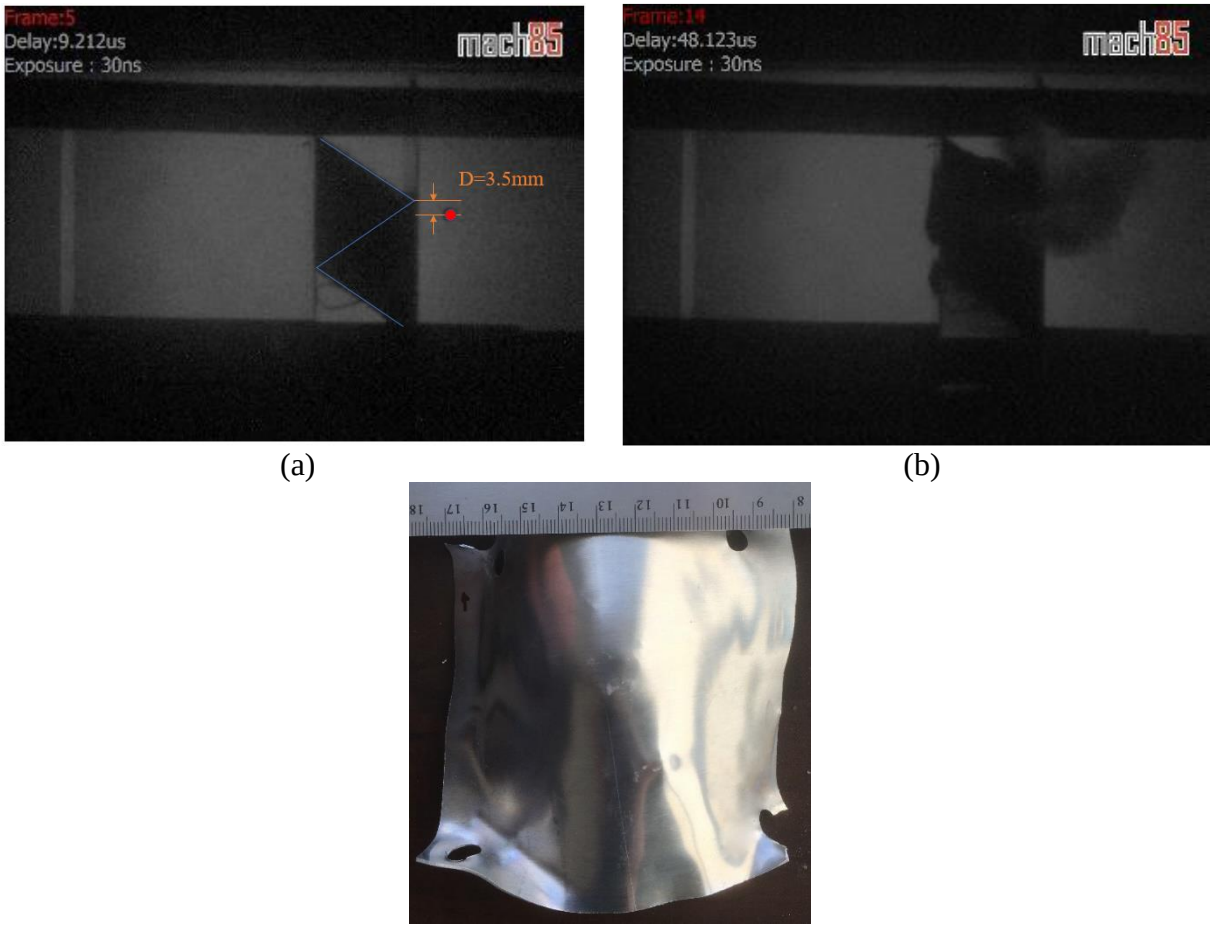

(a) (b)

(c)

Figure 3.17 Test #2 outcome: a) Image of Specimen #2 at 9.212 µs; b) Image of Specimen #1 at 54.972 µs; c) Rear facesheet damage (rear view)

Different-sized particles were employed to fill the portion (corrugated core, front facesheet, projectile, and basalt fabric), similar to section 3.3.1. The front facesheet and projectile were filled with 0.07mm, and the corrugated core and basalt layers were filled with 0.1mm SPH particles. In the Test #2 scenario, the back facesheet was not perforated. Therefore, the finite element was employed in the rear wall to reduce the inherent drawback of SPH.

The numerical model of specimen #2 was designed with utmost efficiency, excluding the portions of the front face sheet and corrugated plate that did not interact with the projectile fragments. The

geometry and impact conditions of the experimental test were accurately replicated in the numerical simulation. Figure 3.18 depicts the numerical simulation of specimen #2

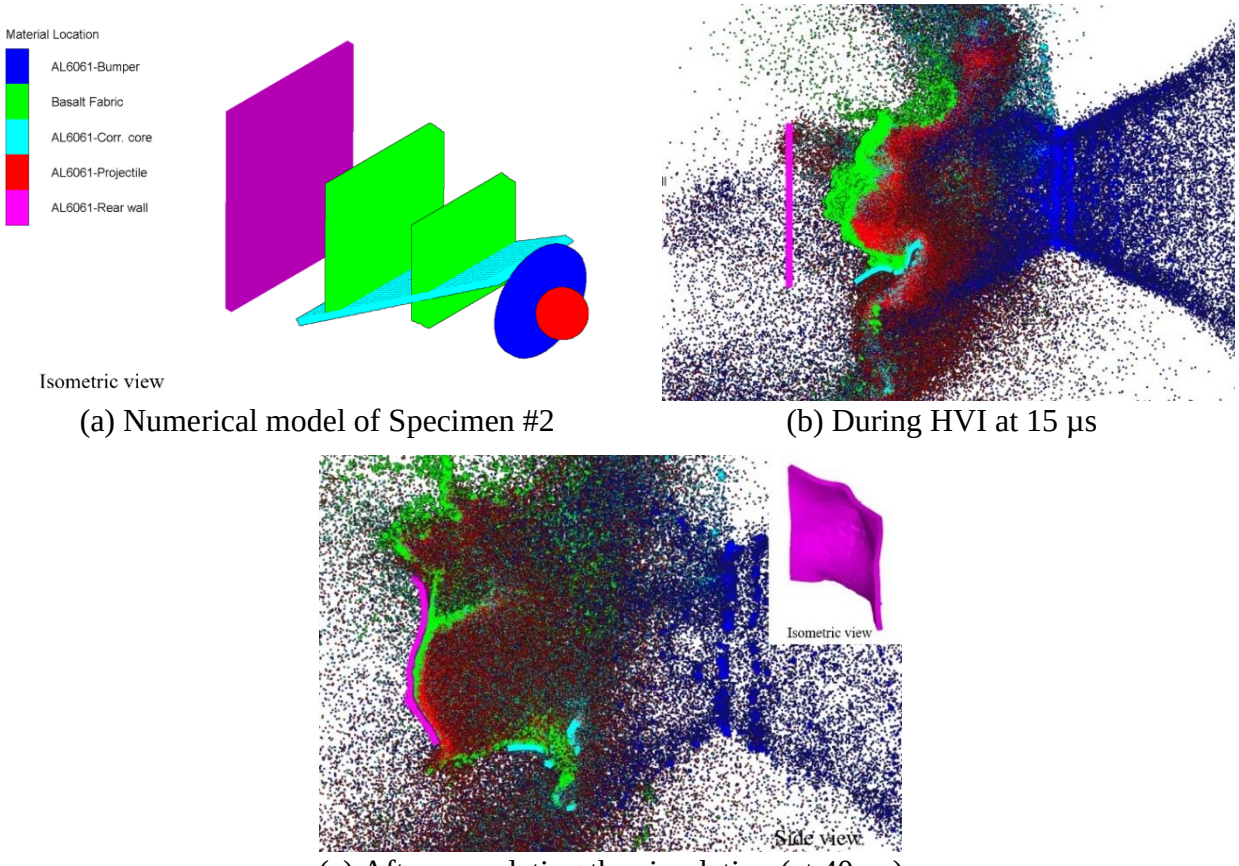

(a) Numerical model of Specimen #2 (b) During HVI at 15 µs

(c) After completing the simulation (at 40 µs)

Figure 3.18 a) Numerical model of Specimen #1; b) The impact reaction at 15 µs; c) Deformation of the rear wall after the HVI.

The numerical simulation, which replicated the conditions of Test #2, resulted in substantial bulging of the rear facesheet, as illustrated in Fig. 3.18 (c). This outcome was consistent with the physical test result demonstrating that the numerical model of specimen #2 was validated by the experimental data with a satisfactory margin of error.

3.3.3. Analysis of Test #3 Data

Specimen #3 had a similar setup to Test #2, with the exception of the presence of basalt layers. The location of impact was determined from the images captured during the HVI of Test #3, which

showed that the projectile hit the specimen approximately 1.05mm below the vertex of the corrugated core. Figure 3.19 displays the physical test of Specimen #3 during HVI, as well as the resulting damage to the rear wall. The physical test of specimen #3 resulted in the formation of two large holes in the rear facesheet.

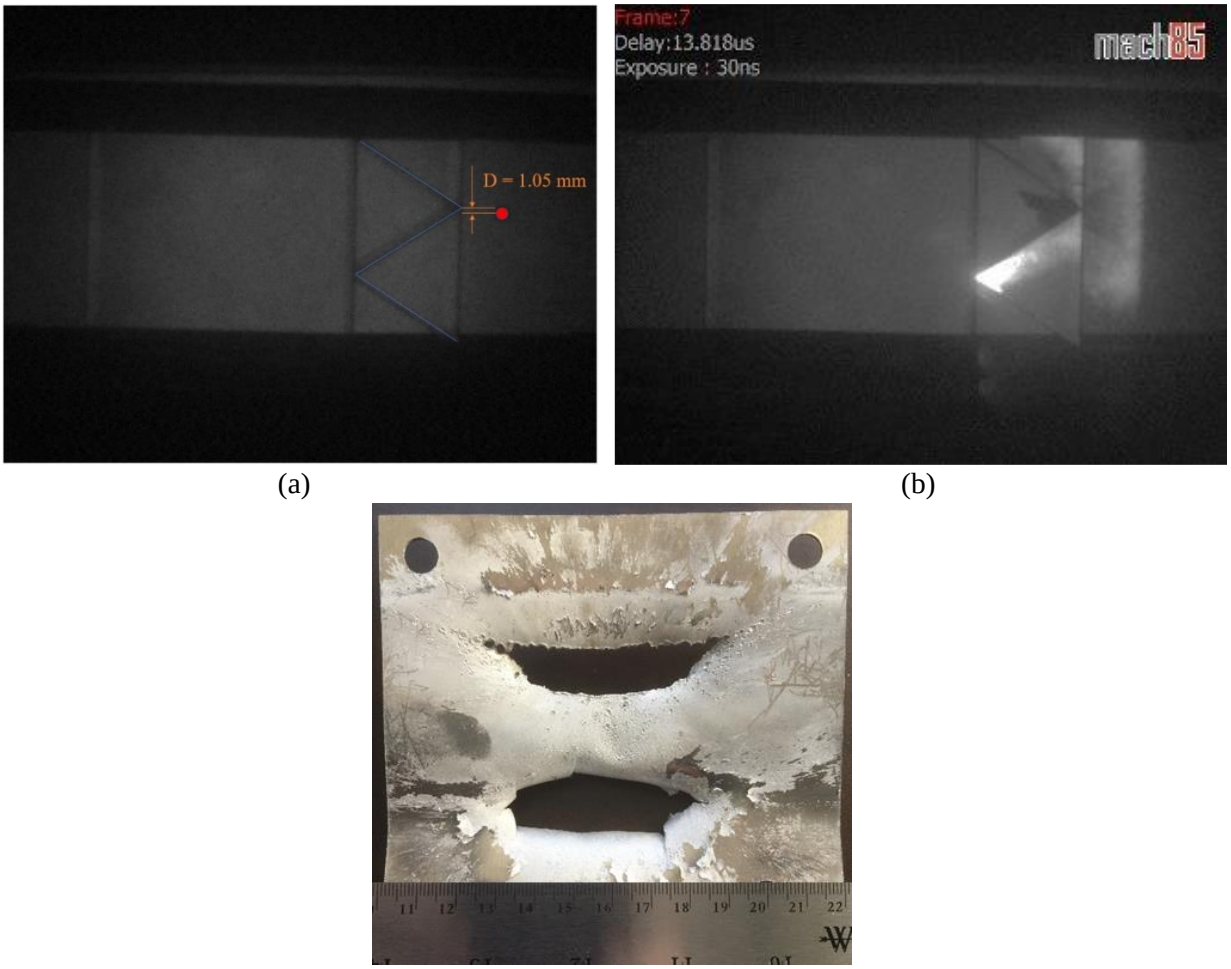

(a) (b)

(c)

Figure 3.19 Test #3 outcome: a) Image of Specimen #3 at 6.909 µs; b) Image of Specimen #3 at 13.818 µs; c) Rear facesheet damage (front view)

Consequently, the numerical model of specimen #3 was anticipated to experience an increased loading and complete perforation of the rear facesheet. To accurately simulate the extreme loading, the entire model of specimen #3, including the rear facesheet, was composed of SPH particles. The front facesheet and projectile were filled with 0.07 mm, and the corrugated core and rear facesheet were filled with 0.1 mm SPH particles. The impact location in the numerical model was set according to the results obtained from the physical experiment, as shown in Fig. 3.20.

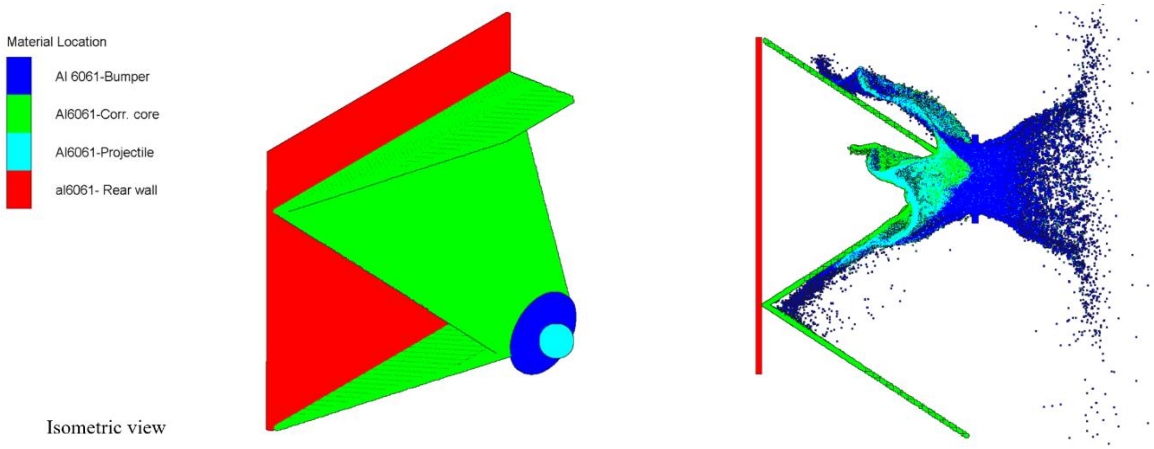

(a) Numerical model of Specimen #3 (b) During HVI impact (4.6 µs)

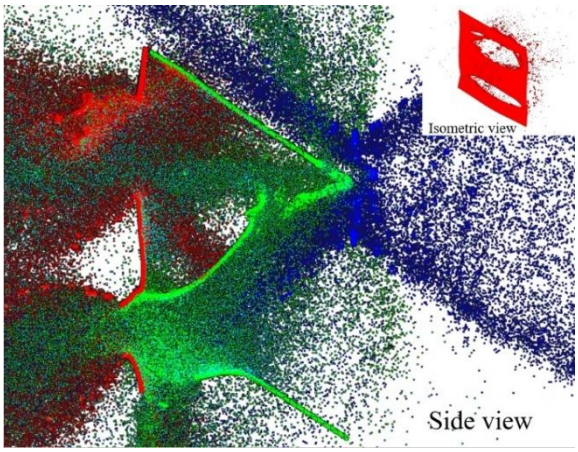

(c) After completing the simulation (at 40 µs)

Figure 3.20 a) Numerical model of specimen #3; b) The impact reaction at 4.6 µs; c) Damage of the rear wall after the HVI

3.3.4 Comparison of the Results

Table 3.7 Comparison between experimental and numerical data

	Experimental data, mm			**Numerical data, mm**	**Error, %**
Front facesheet hole	10.42			10.64	2.1
Rear facesheet holes	1st	Length, L_1	58.07	56.58	2.5
		Width, W_1	10.88	8.84	18.74
	2nd	Length, L_2	49.4	47.49	3.86
		Width, W_2	14.2	15.31	7.81

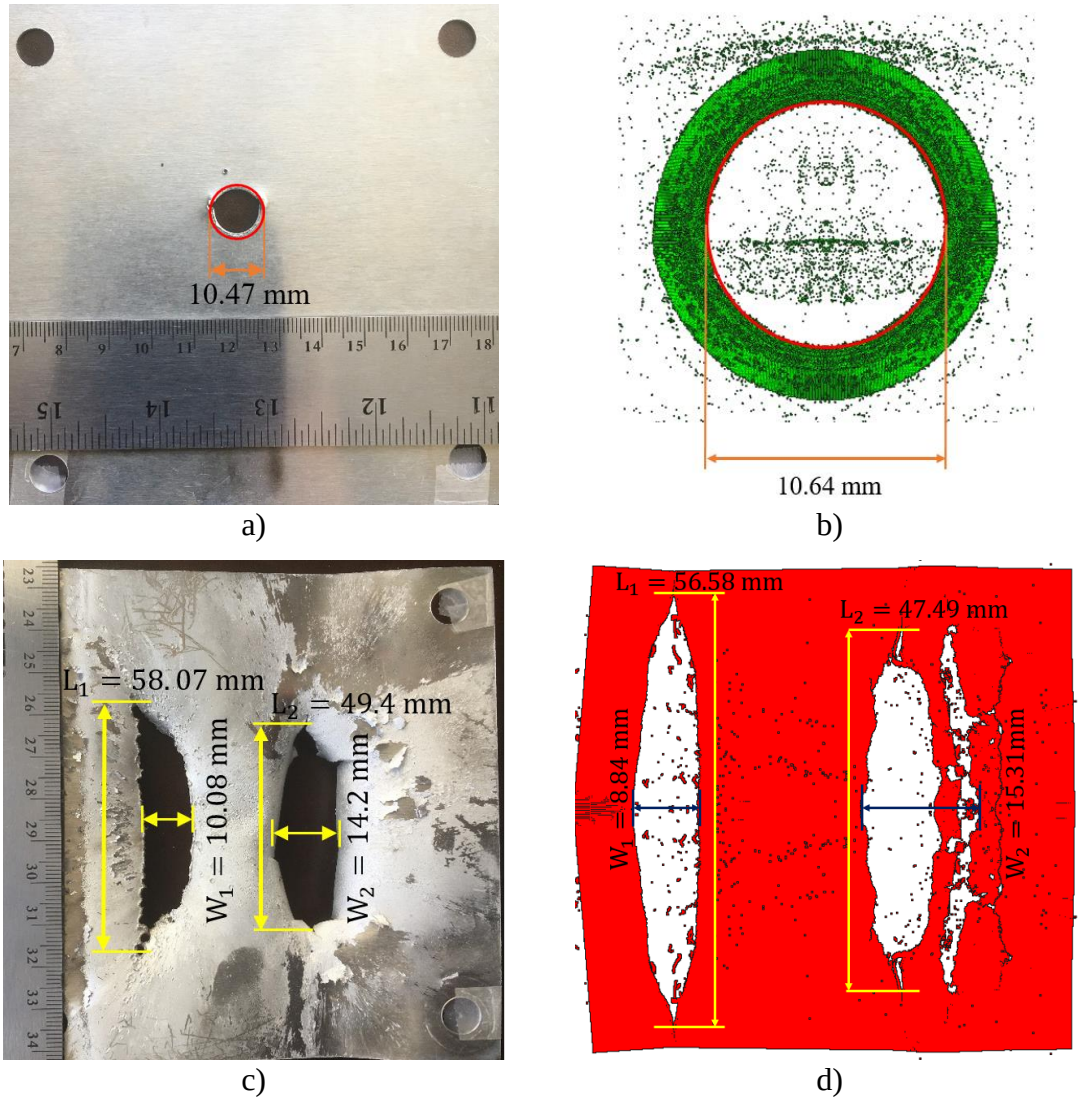

Figure 3.21 Test #3 data: a) hole in front facesheet (physical test); b) hole in front facesheet (simulated); c) damage of rear facesheet (physical test); d) damage of rear facesheet (simulated)

The validation of the numerical model was primarily based on the comparison of the dimensions of the perforated holes in the front and rear facesheets. The average error in the rear facesheet was 8.23%, while the front facesheet exhibited an error of only 2.1%, which was deemed to be a sufficient level of accuracy to support the predictions of the numerical model. The following figures present a comparison of the experimental and numerical results for the sizes of the holes in the front and rear facesheets. Thus, it can be concluded that the numerical model is sufficiently validated by the specimen #3 test results. Fig 3.21 demonstrates the comparison between experimental and Numerical data.

3.4 Summary of Chapter

This chapter presents a numerical model of the CCSP. A combination of Smoothed-Particle Hydrodynamics and Finite Element Method was utilized to take advantage of the strengths of each method while avoiding their drawbacks. A comprehensive calibration process based on physical data was performed to determine the appropriate range of SPH particle sizes for the numerical analysis. The calibration and previous studies resulted in the development of a robust numerical model for the CCSP, capable of delivering accurate predictions while keeping computational costs reasonable. The effectiveness of the CCSP in shielding a spacecraft from a 6mm orbital debris impact at 7 km/s was evaluated through three Hypervelocity Impact (HVI) tests. The numerical model of the CCSP was validated by the results of these physical tests.

4. PARAMETRIC ANALYSIS OF THE CCSP

An essential design exploration technique is parametric analysis, which may be used, for example, to investigate the impact of the CCSP's shielding performance under various impact scenarios and CC angles. A parametric analysis, also known as a sensitivity analysis, examines the effects of various geometric on the problem's solution.

A preliminary investigation of the hypervelocity impact protection performance of the CCSP showed the variation of the CCSP protection with the impact position. For this reason, a parametric study is required to understand the effect of the corrugated core design parameters on its ballistic protection performance.

In this section, the ballistic performance of the CCSP is evaluated at different locations and impact conditions to determine the weakest and most decisive point of the panel. In addition, the parametric study includes the effect of the corrugated core angle on the ballistic and structural integrity of the panel.

4.1 Parameters Selected for Assessment

In this section, we examine two key parameters for evaluating the performance of MMOD shielding based on various HVI scenarios. The parameters are the test outcome and the critical diameter of the projectile. The test outcome is a qualitative measure of the condition of the rear face sheet after the HVI test, specifically whether it has been perforated or not. The critical diameter, a quantitative characteristic, represents the minimum diameter of the projectile required to cause perforation of the rear face sheet.

Determining these two parameters through numerical simulation requires precise modelling of the damage formation, which is highly dependent on the accuracy of the modelling of the generation and expansion of the debris cloud. As illustrated in Fig. 4.1, even a little deviation in the impact point, such as a 0.5 mm offset, can significantly alter the structure of the debris cloud, its interaction with the rear facesheet and ultimately, the outcome of the test. The results presented in

Fig. 4.2, and 4.3 show that the model calibration outlined in Section 3.1.3 has effectively achieved an acceptable level of accuracy in simulating the formation of the debris cloud and impact hole.

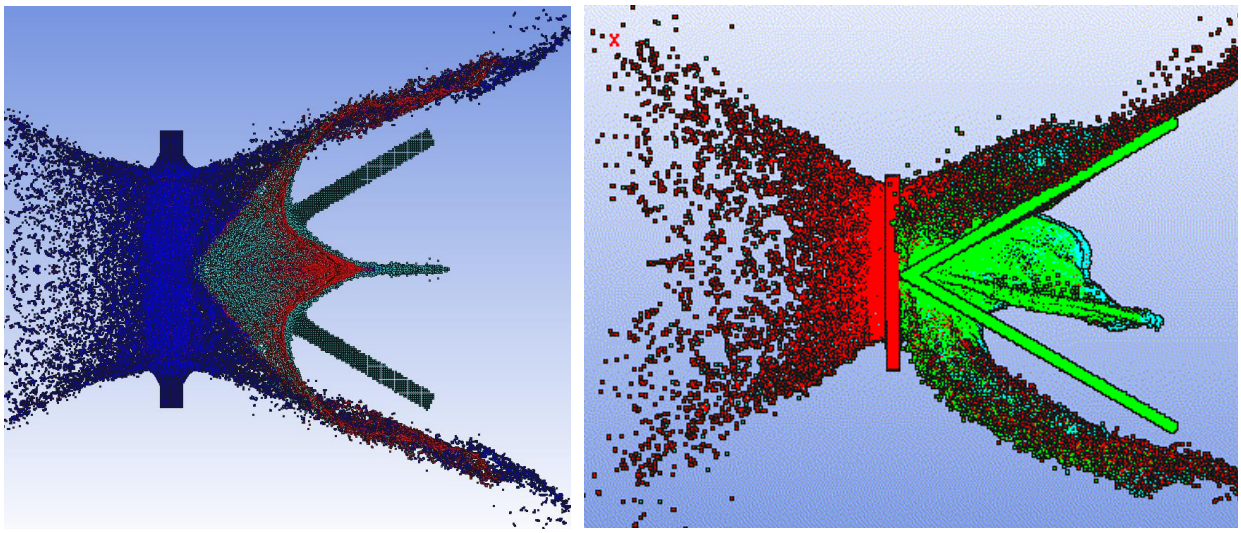

a) Impact at the peak of CC b) Impact at nearby (1 mm) the peak of CC

Figure 4.1 Effect of a slight change of initial impact point

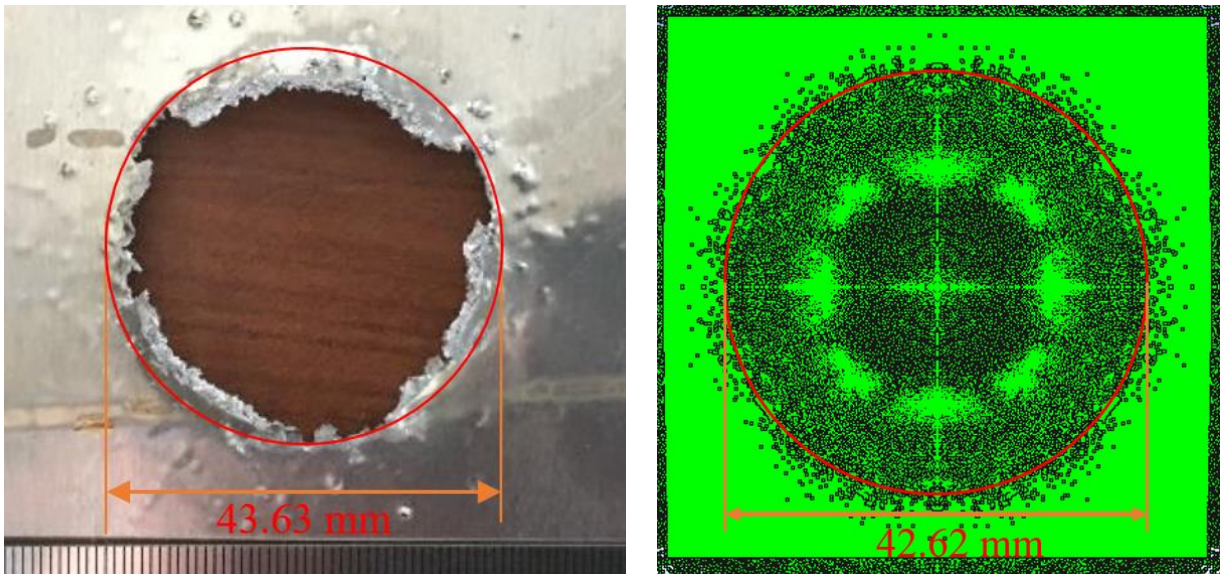

a) Rear wall damage measurement in physical test b) Rear wall damage measurement in numerical simulation

Figure 4.2 Damage assessment at HVI a) physical test; b) numerical simulation

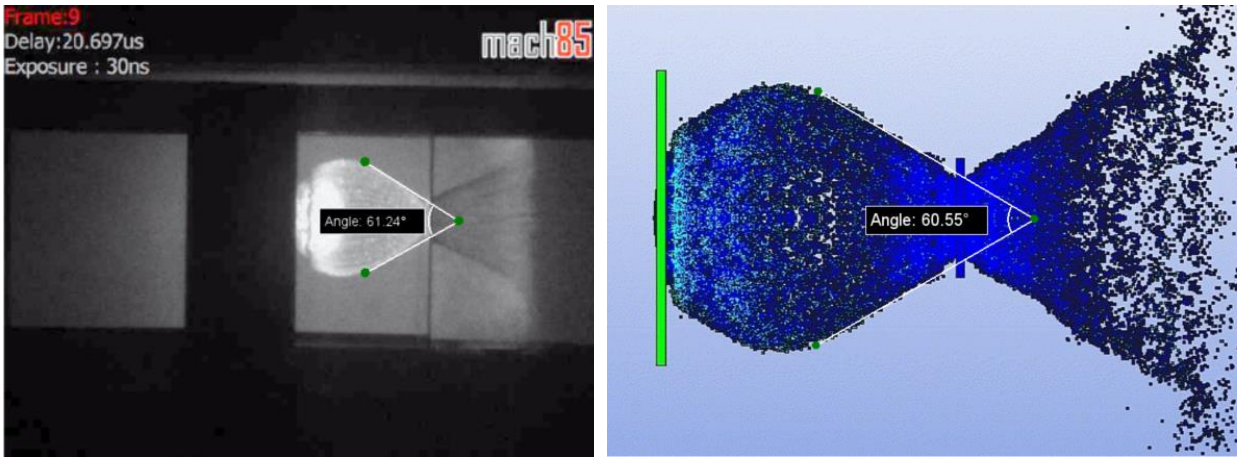

a) Expansion angle of debris cloud from physical test

b) Expansion angle of debris cloud from numerical simulation

Figure 4.3 Expansion angle of debris cloud from a) physical test; b) numerical simulation

Damage assessment was chosen as the primary approach to conducting the parametric study. Besides, analysis of debris cloud interaction with the panel was implied to support the assessment.

4.2 Numerical Setup for Parametric Study

This section describes the numerical setup of the CCSP to perform the parametric study of finding the most susceptible location on CCSP for HVI. The front facesheet and projectile were modelled using SPH particles with a size of 0.07 mm, while the corrugated core was filled with SPH particles of size 0.1 mm. The finite element mesh size was set at 0.2 mm, with an erosion strain of 1.0.

A 6 mm projectile at 7 km/s carries considerable kinetic energy (34.674 kJ) to perforate the conventional structural sandwich panel. To better understand the severity of damage to the rear facesheet, the kinetic energy of the projectile was decreased to a level where it would only penetrate the weakest point of the CCSP. After thorough research, a 3.3 mm diameter projectile was selected for the investigation. The simulations were stopped after 30 microseconds, and damage to the rear facesheet was evaluated. The parameters of the CCSP shield are outlined in Table 4-1.

Table 4.1 The parameters of numerical setup to conduct a parametric study

Parameter	Value
Projectile Diameter, mm	3.3
Material of Projectile	Al6061-T6
Projectile Speed, km/s	7
Panel thickness, mm	42
Facesheet thickness, mm	1
Material of facesheet	Al6061-T6
Corrugated plate thickness, mm	0.8
Corrugated plate angle	60
Material of corrugated plate	Al6061-T6

4.3 Initial Conditions for Parametric Study

In order to conduct a parametric study, a set of different initial impact conditions were applied to understand the influence of corrugated core configuration. The investigation allows for determining the CCSP's weakest points against HVI. In the study, the following conditions, such as projectile size, velocity, material, thicknesses of the CCSP parts, and size of SPH particle and finite element mesh, were constant. Only the impact conditions, such as the impact point and angle, were altered to discover the most vulnerable impact areas and the directions.

Given the geometry of the corrugated plate, three key positions, referred to as "peak," "valley," and "midpoint," were studied to identify the most susceptible areas within the panel. Four impact angles (0°, 30°, 45°, and 60°) were analyzed for each position. Consequently, the projectile hit the panel at four different angles for each of the previously mentioned impact points.

A total of 12 distinct scenarios were studied to gain insight into the overall protection level of the CCSP and identify the most vulnerable areas among them. A comprehensive description of 12 impact scenarios is presented in Table 4.2.

Table 4.2 Cases of study

CC peak	Case #	Impact angle	Velocity in Y, Z-axis
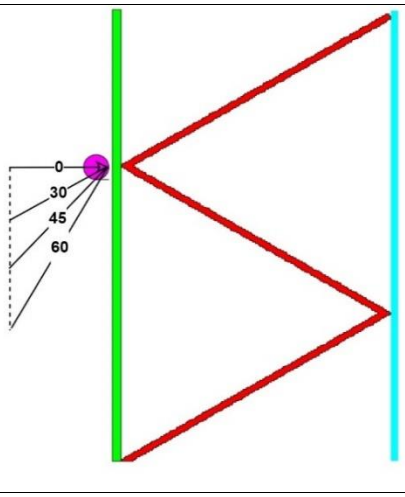	1.1	0°	Y-axis – 0 Km/s
			Z-axis – 7 km/s
	1.2	30°	Y-axis – 3.500 Km/s
			Z-axis – 6.062 km/s
	1.3	45°	Y-axis – 4.949 Km/s
			Z-axis – 4.949 km/s
	1.4	60°	Y-axis – 6.062 Km/s
			Z-axis – 3.500 km/s
Middle of CC Slope			
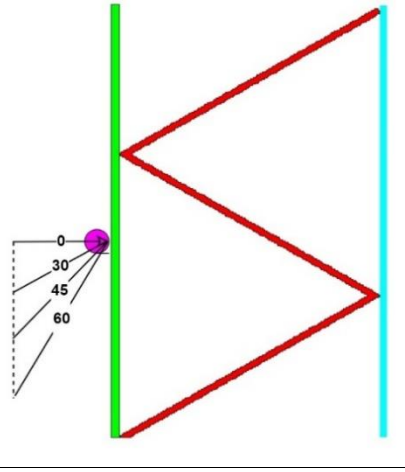	2.1	0°	Y-axis – 0 Km/s
			Z-axis – 7 km/s
	2.2	30°	Y-axis – 3.500 Km/s
			Z-axis – 6.062 km/s
	2.3	45°	Y-axis – 4.949 Km/s
			Z-axis – 4.949 km/s
	2.4	60°	Y-axis – 6.062 Km/s
			Z-axis – 3.500 km/s
CC Valley			
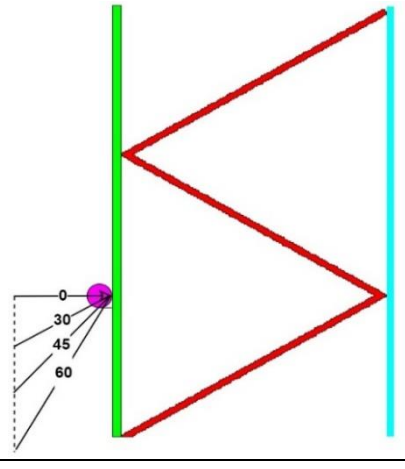	3.1	0°	Y-axis – 0 Km/s
			Z-axis – 7 km/s
	3.2	30°	Y-axis – 3.500 Km/s
			Z-axis – 6.062 km/s
	3.3	45°	Y-axis – 4.949 Km/s
			Z-axis – 4.949 km/s
	3.4	60°	Y-axis – 6.062 Km/s
			Z-axis – 3.500 km/s

4.4 Simulation Results

Out of 12 cases of HVI, perforation occurred in two instances, specifically cases #1.1 and #3.1. These two cases involved the projectile hitting the front facesheet in CC "peak" point and "valley" point. When the projectile hit at CC "peak" point, it resulted in a larger hole of 28.36 mm^2, while hitting at CC "valley" point resulted in a smaller hole of 0.87 mm^2. In both cases, the projectile hit the front facesheet perpendicularly. The remaining simulations resulted in a slight bulging and a small crater on the rear facesheet, but no perforation occurred. Detailed information regarding the simulation results is presented in Table 4.3 and Appendix A.

Table 4.3 Numerical test outcomes for 12 impact scenarios

#	Impact Point	Impact Angle	Damage to rear facesheet
1.1	CC peak	0°	Perforation
1.2	CC peak	30°	Bulged, No perforation
1.3	CC peak	45°	Small craters, no perforation
1.4	CC peak	60°	No crater, no perforation
2.1	Middle of CC slope	0°	Bulged, No perforation
2.2	Middle of CC slope	30°	Bulged, No perforation
2.3	Middle of CC slope	45°	Small craters, no perforation
2.4	Middle of CC slope	60°	No Crater, no perforation
3.1	CC valley	0°	Bulged, Tiny perforation
3.2	CC valley	30°	Bulged, No perforation
3.3	CC valley	45°	Small craters, no perforation
3.4	CC valley	60°	No Crater, no perforation

When a projectile hits the panel perpendicularly at the CC peak point, the debris cloud is generated while the projectile perforates the front face sheet. The central part of the debris cloud perforates

the vertex of the corrugated plate, while the lateral parts slide along the plate's slopes, forming a three-tongue cloud of fragments. The central tongue of the debris cloud contains more energetic fragments that pose a more significant threat to the rear facesheet. Fig. 4.4 demonstrates the debris cloud shape at 3 and 15 µs and the extent of the damage on the rear facesheet.

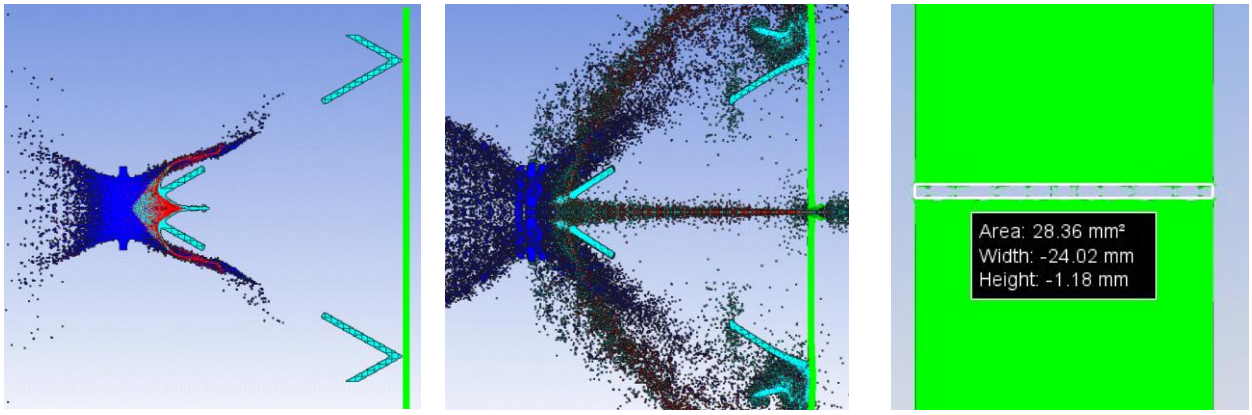

a) b) c)

Figure 4.4 Numerical simulation of HVI at CC peak point: a) debris cloud 3 µs after impact; b) debris cloud 15µs after impact; c) impact hole in rear facesheet after 30 µs

When a projectile impacts the panel in a normal direction to position at the CC valley point, the resulting debris cloud moves towards the rear wall, as illustrated in Figure 4-5. However, the corrugated plates prevent the fragments from expanding and instead guide them down toward the bottom corner of the plate. Consequently, the debris cloud accumulates near the bottom corner and eventually perforates the rear facesheet. Fig. 4.5 shows the debris cloud at 3 and 15 microseconds and the impact hole on the rear facesheet.

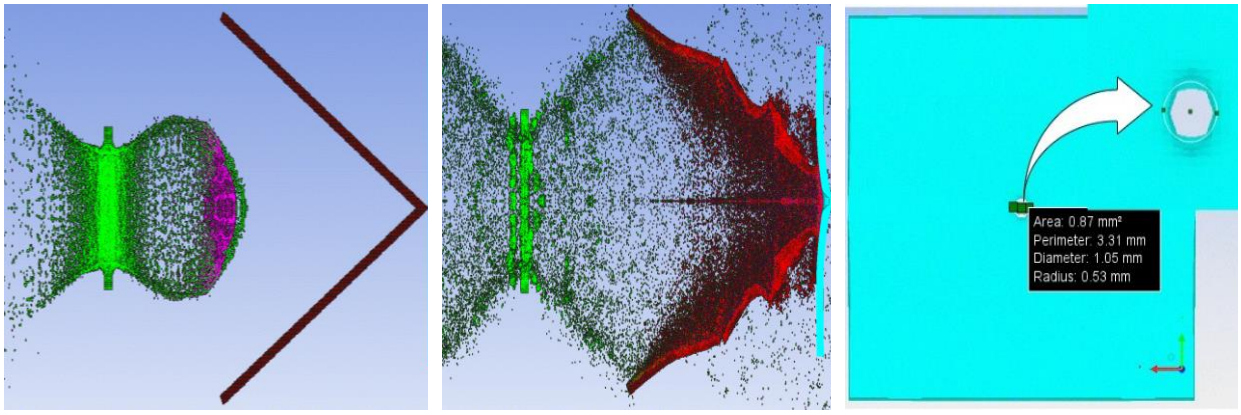

a) b) c)

Figure 4.5 Numerical simulation of HVI at CC valley point: a) debris cloud 3 µs after impact; b) debris cloud 15µs after impact; c) impact hole in rear facesheet after 30 µs

The normal impact causes more damage in terms of penetration/perforation of the rear wall due to the higher normal component of momentum compared with oblique impact. For instance, the in the case of normal impact at 7 km/s, the normal component of velocity is at its maximum. When the impact occurs at an angle such as 30°, 45°, and 60°, the normal component of velocity reduces to 6.062 km/s, 4.949 km/s, and 3.500 km/s, respectively.

When a projectile hits a panel at an angle, the fragments it produces must travel a greater distance and interact with the corrugated core before reaching the rear facesheet. For instance, if the projectile hits the panel straight on, the fragments must travel 40 mm to reach the rear facesheet, but if it hits the panel at a 30-degree angle, the fragments must travel 44.94 mm. This increased distance results in the fragments spreading out over a larger area, which, coupled with the interaction with the corrugated plate, reduces the overall momentum subjecting the rear facesheet.

4.4 Effect of Impact Point

The way in which the debris cloud interacts with the corrugated plate core plays a significant role in the shielding performance of the CC sandwich panel. This section aims to comprehensively examine how the initial impact point's position affects the panel's shielding performance and identify the most vulnerable points on the CCSP.

An investigation was conducted on the vulnerability of the panel, focusing on the "peak" and "valley" points displayed in Fig. 4.6. The impact site of the projectile was varied, shifting from Y = 0 to Y = 0.5 mm, Y = 1.0 mm, and Y = 1.5 mm, at both the peak and valley locations of the corrugated core. The numerical setup used in this investigation was identical to the one outlined in section 4.2, except for the projectile size. The current analysis defines the critical diameter as the projectile size that results in a tiny perforation, which measures less than 1 mm^2, on the rear facesheet. By performing a series of numerical HVI tests, the critical diameter was determined for every impact point that was examined. The case of normal impact was considered.

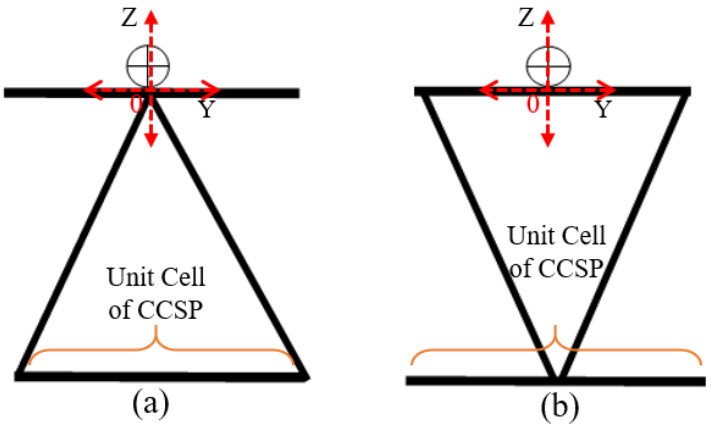

Figure 4.6 Impact location near the CC peak and valley points

Although hypervelocity impact directly at the CC peak point results in more significant damage, the likelihood of such an event is low. Therefore, it is essential to examine the ballistic performance of CCSP in the surrounding area. Fig. 4.7 demonstrates the variation of the projectile critical diameter in the vicinity of the CC peak point, as determined through numerical analysis.

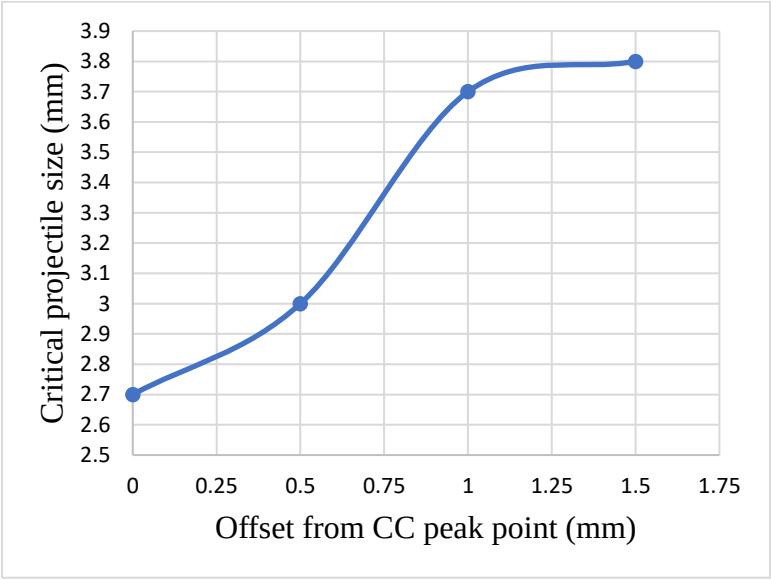

Figure 4.7 Critical diameter of projectile near the CC peak point

The graph shows a significant change in the critical projectile size of 40% as the impact location changes by only 1.5 mm from the CC peak point. When comparing the impact directly at the peak point (Fig. 4.8a) to the scenario with a 1.5-mm offset (Fig. 4.8b), the simulation demonstrated a significant change in how the debris cloud splits and interacts with the corrugated plate and rear face sheet.

It illustrates that a slight offset causes the expansion of debris clouds over a broader area resulting in a better shielding performance of the panel.

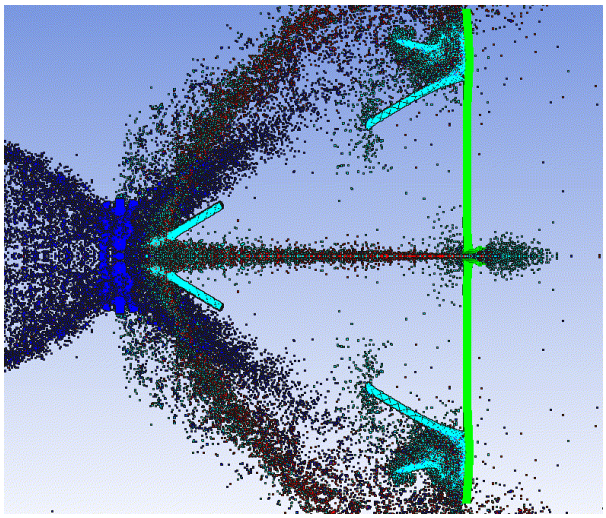

a) Impact location toward the pinpoint of the peak of CC

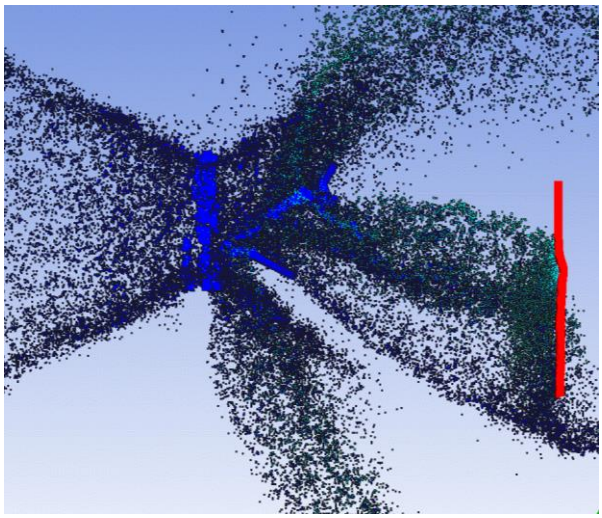

b) Impact location toward the 1.5 mm offset from the peak of CC

Figure 4.8 Effects of the slight alteration of impact location toward the peak of CC

Another vulnerable point on the panel is the CC valley point. To determine the critical diameter in its proximity, a similar approach was employed as in the previous section. The variation of the critical projectile diameter near the valley point of the panel is presented in Fig. 4.9

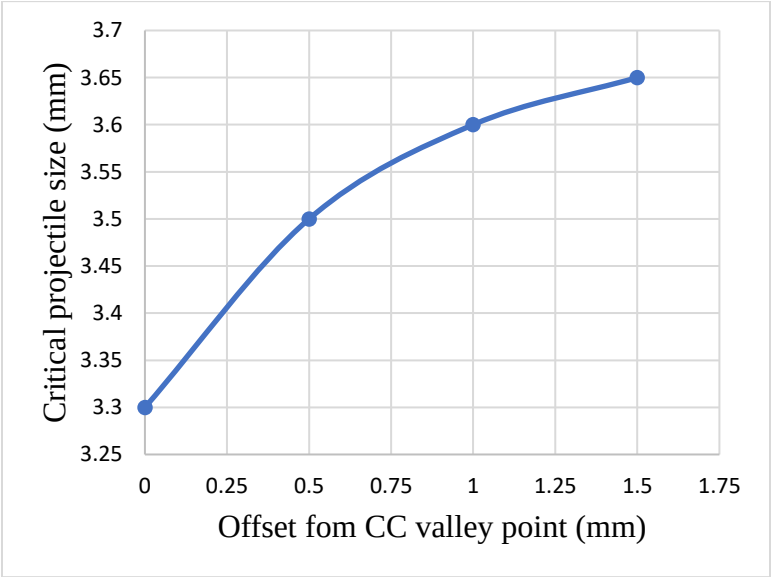

Figure 4.9 Critical diameter of projectile near the CC valley point

The graph indicates that if the CC valley point is shifted by 1.5 mm, the critical diameter of a projectile can increase by up to 10%, which is lower than observed in a previous case.

The variation of the critical diameter of a projectile over a unit cell of the CCSP is shown in Fig. 4.10. The figure highlights that the impact point across the middle of the CC slope is the most secure compared to the two most vulnerable areas in the proximities of the CC peak and valley points. Of the two above regions, the CC peak point is the weakest, posing the highest risk for projectile penetration.

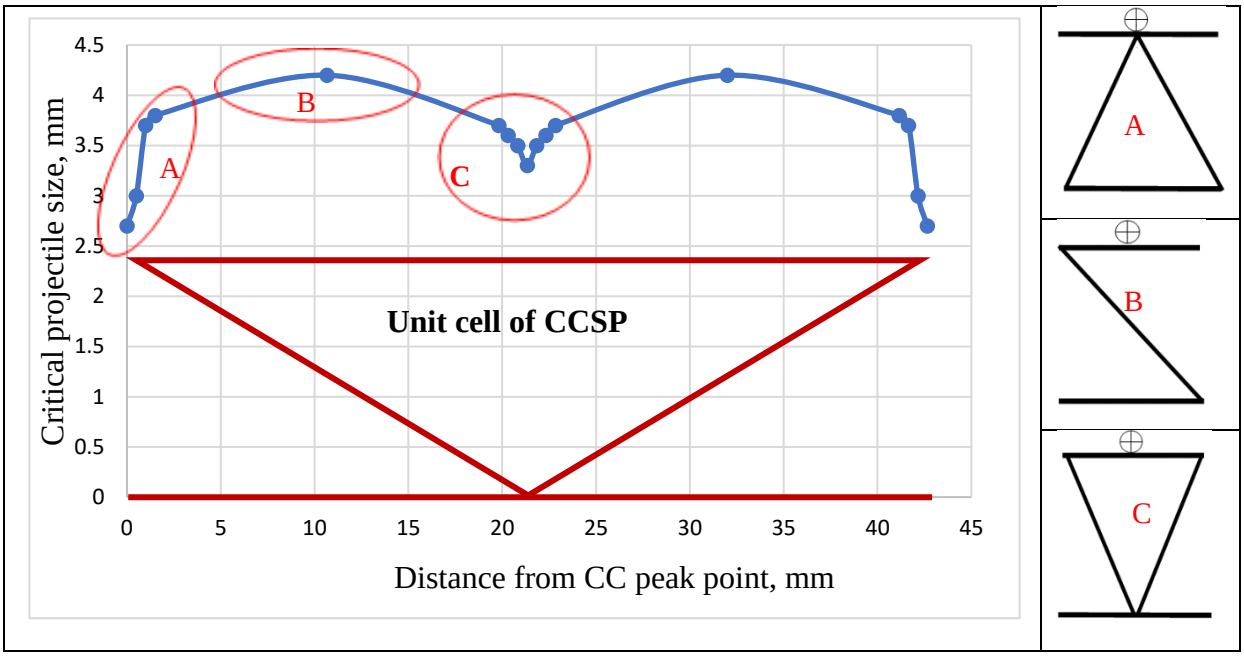

Figure 4.10 Critical diameter of projectile throughout the CCSP

4.6 Effect of Corrugated Core Angle

By conducting numerical HVI testing, it was determined that the CCSP featuring a triangular core exhibited superior shielding performance among the five geometries shown in Fig. 2.1. The details of numerical testing are presented in Appendix B. Consequently, the research was directed toward further investigating and analyzing the configuration with the triangular core.

This section investigates the effect of a CC angle on the shielding and ballistic performance of the CCSP. The probability of impacting the weak zone near the CC peak point is lower than that of

the wider zone near the CC valley point. Thus, out of the two most vulnerable points, the CC valley point was selected for the analysis of the effect of the CC angle.

In the present study, four different angles of the corrugated core were chosen: 45°, 60°, 75 °, and 90°. The thickness of the corrugated plate was adjusted to ensure that all configurations evaluated had equivalent area densities. That thickness is specified in Table 4.4.

Table 4.4 Thickness of the corrugated plate vs core angle

Corrugated core angle, θ	**Corrugated plate thickness (mm), t_{CP}**	**Areal Density (AD), kg/m^2**
45°	0.558	9.41
60°	0.728	9.41
75°	0.884	9.41
90°	1.135	9.41

4.6.1 Shielding Performance

The semi-infinite rear plate was utilized to evaluate the shielding performance of CC sandwich panels with different CC angles. The depth of the deepest crater on the semi-infinite rear plate was chosen to quantify the numerical HVI test outcome. Fig. 4.11 shows the setup for the numerical HVI testing, where a 6 mm diameter projectile impacted the 1 mm front facesheet at a velocity of 7 km/s. The CC plate thickness was modified along the core angle to maintain a constant areal density as per Table 4.4. The obtained results are shown in Table 4.5.

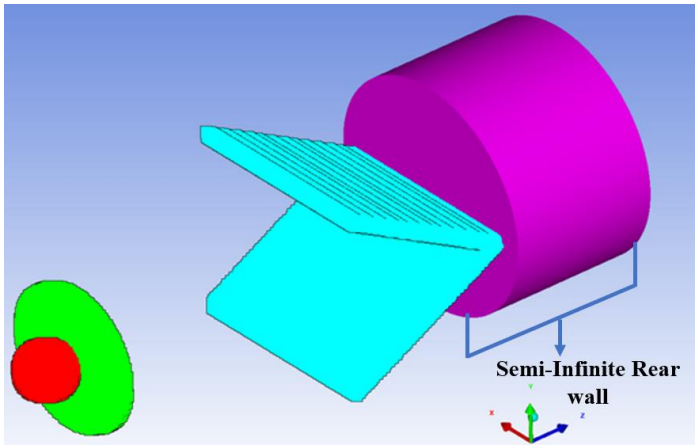

Figure 4.11 Setup with a semi-infinite rear plate

Table 4.5 Crater depth in the semi-infinite rear wall

The angle of the corrugated core, θ	**Crater depth in semi-infinite rear plate (mm)**
45°	17.21
60°	14.82
75°	11.25
90°	8.97

According to the study, increasing the CC angle leads to a reduction in the damage to the rear wall. This trend is attributed to two primary factors: 1) greater space for debris clouds to disperse before reaching the semi-infinite rear wall and 2) a higher thickness of CC plate required to maintain a constant areal density. Specifically, a corrugated core with a 90° angle resulted in a crater size that was about half the size of the one created by a corrugated core with a 45° angle.

4.6.2 Structural Performance

The purpose of this section is to assess the trend in the relationship between the CC angle and the structural stiffness of CC sandwich panels. A three-point bending test was carried out numerically utilizing the FEM, widely recognized for its highly precise numerical approximation in the context of static structure analysis [64]. The assembled configuration for the 3-point bending test of CCSP is shown in Fig. 4.12.

Four numerical tests were conducted for the CC angles of 45°, 60°, 75°, and 90°. The thickness of the CC plate was adjusted along the core angle in order to keep the areal density from changing, as detailed in Table 4-4. The contact surface between the loading bar to the upper facesheet and support bars to the lower face sheet had frictionless contacts. The interface treatment was "Adjust to Touch." As the loading bar applied a compressive force on the upper facesheet, the support bar was fixed from any displacement to mimic the standard ASTM C393 test scenario. The loading and support bar had structural steel material properties from the ANSYS material data source. Al6061-T6 material model was acquired from [65],[66]. Debonding of the corrugated core sandwich panel wasn't considered in this study.

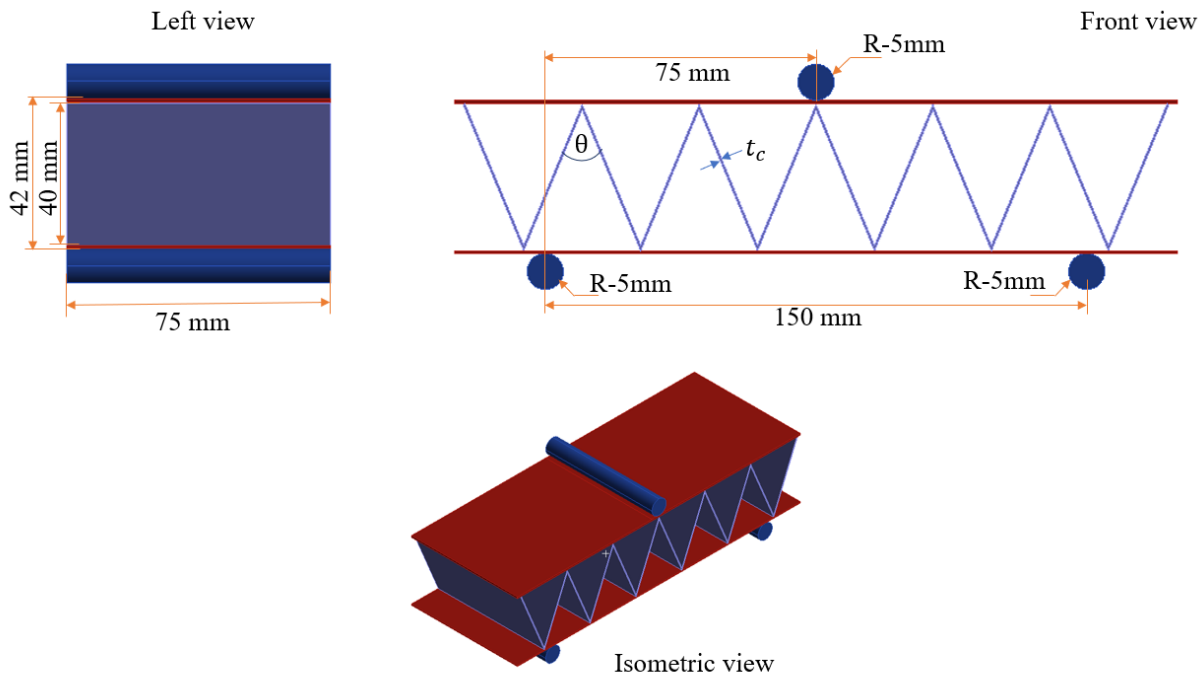

Figure 4.12 Typical assembly configuration for flexural analysis of CCSP

In the numerical testing process, a compressive load was continuously applied via the loading bar until a displacement of 10 mm was reached. The required force was then calculated, and the resulting data is displayed in Fig. 4.13 as a load vs crosshead displacement curve. The results demonstrate that as the CC angle decreases, the stiffness and flexural strength of the CC sandwich panel experience a significant increase.

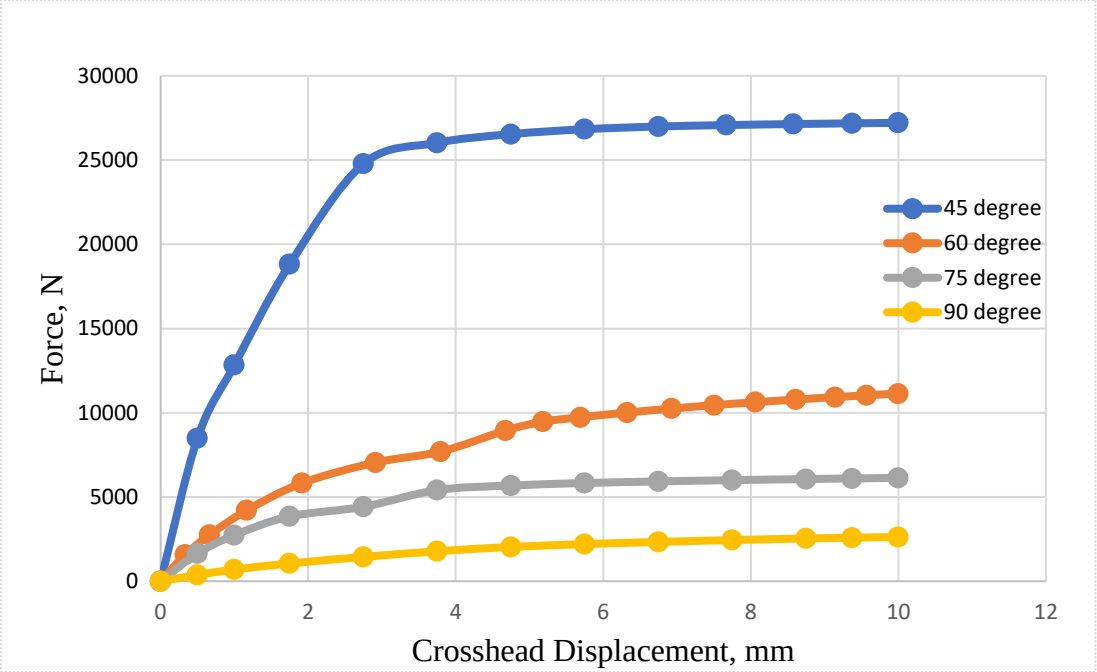

Figure 4.13 Load-crosshead displacement curve

4.7 Summary of Chapter

According to the study conducted, the greatest risk to a CC sandwich panel is posed by hypervelocity impacts that occur perpendicular to its surface. The regions surrounding the peak and valley points of the panel are especially vulnerable to HVI.

An analysis of the CCSP shielding performance indicated that the protection level of the CC sandwich panel increases as the angle of the corrugations rises while keeping the areal density constant. The structural stiffness of the CCSP was evaluated at varying CC angles via a 3-point bending test, and the study confirmed that a reduction in angle results in an increase in structural stiffness.

5. ENHANCE THE PROTECTION LEVEL OF CCSP

The effectiveness of the CCSP configuration in providing shielding was discussed in the previous chapter. However, it was noted that the protection level is weaker at the CC peak and valley points compared to the middle area of the CC slope. To improve the overall shielding performance of the CCSP, it is necessary to address these weaker points and enhance their protection level. One potential solution is to modify the core to better fragment and disperse debris clouds, which would improve its shielding performance.

The improvement of the shielding performance of the CCSP through the modification of the geometry of the corrugated plate core will be explored in this chapter. This procedure would be led by a set of evaluation steps, which are shown in Fig. 5.1. These evaluations would allow to identify the areas that require improvement and make the necessary modifications to enhance the protection level of the CCSP.

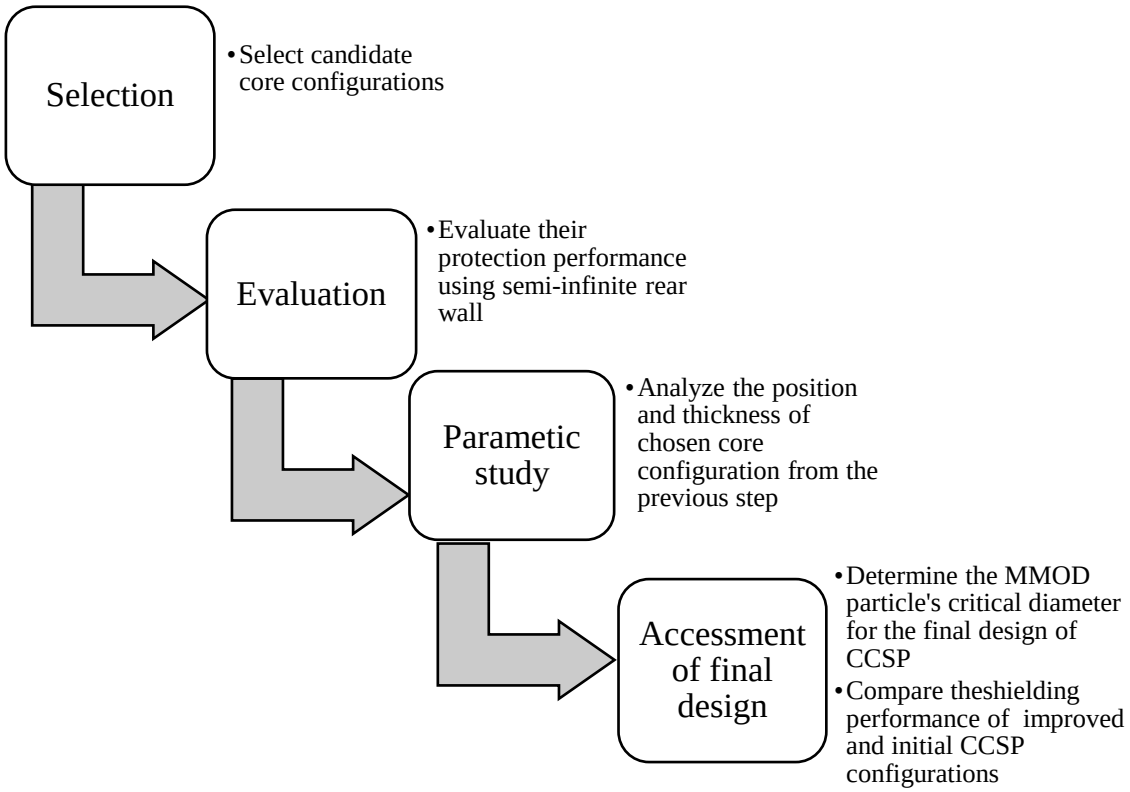

Figure 5.1 Enhancement of the CCSP design workflow

Several configurations of the CC were chosen at the beginning of this study for analysis. Damage assessment testing was then conducted numerically to evaluate their shield performance. Among the candidate core configurations, the configuration with the least damage in the semi-finite back wall was chosen. Following that, a parametric study was undertaken to further enhance the shielding effectiveness of the CCSP by modifying its characteristics.

Once completed, the shield performance of the enhanced design of the CC was accessed and compared to the initial configuration. To ensure a fair comparison, the areal density of the core was kept constant throughout the process of enhancing the shielding performance. More information about each step of this enhancement procedure will be provided in the following sections.

5.1 Assessing the Shielding Performance of Selected Corrugated Core Designs

This study is performed to enhance the shielding performance of the CCSP. It was identified in the previous section that the "valley" area of the corrugated core is one of the vulnerable locations to HVI. Three different design options were considered to achieve this goal: a solid corner, a corner with a flat web, and a corner with a ridge. These designs were selected as potential solutions to enhance the overall protective capability of the sandwich panel with the CC.

The corrugated angle (θ) was set at 60 degrees and the corrugated plate thickness (t_c) at 0.7 mm to keep the areal density identical to the initial CCSP configuration. The distance (h), which refers to the location of the added material (Fig. 5.2a), was set to 3.5 mm. To maintain the same areal density, the flat-web design (Fig. 5.2b) was assigned a "flat web" thickness ($t_{f.w.}$) of 0.874 mm, whereas the "ridge" design (Fig. 5.3c) was given a "ridge" thickness (t_r) of 0.45 mm.

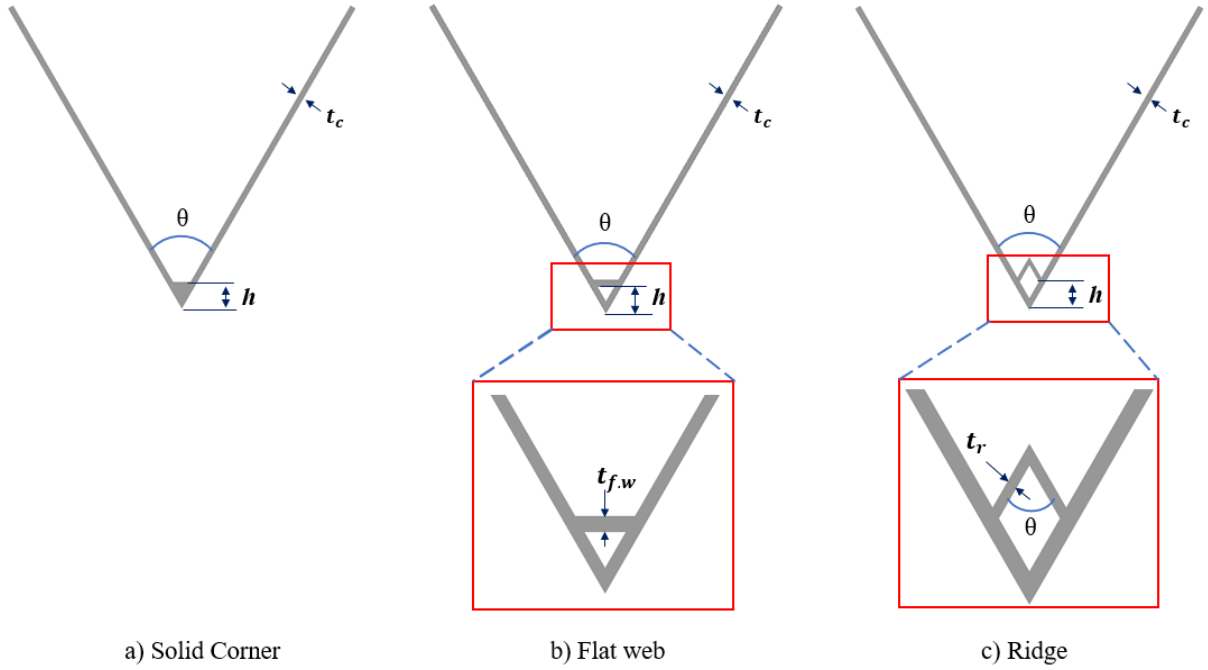

Figure 5.2 Geometry of solid corner, corner with flat web, and corner with ridge

5.1.1 Numerical Configuration and Evaluation Metric

The investigation was conducted using SPH and FEM methods. Different sizes of SPH particles were used to model the numerical configurations. The front facesheet and projectile were modelled using SPH particles with a size of 0.07 mm, while the corrugated core was filled with SPH particles of size 0.1 mm. A semi-infinite rear wall was employed as an assessment metric, and the depth of damage in the rear wall was calculated to understand which design was more effective against HVI. The finite element mesh size was set at 0.2 mm in the rear wall, with an erosion strain of 1.0. For this study, a 6.0 mm projectile traveling at 7 km/s was chosen for the impact tests, and Al 6061-T6 material was used for all parts in the models. In the numerical test setup, the rear wall was assumed to be semi-infinite and was given a thickness of 15mm. It was modeled using finite elements. Fig. 5.3, 5.4, and 5.5 show the numerical models of the solid corner, a corner with a flat web, and a corner with ridge designs, respectively.

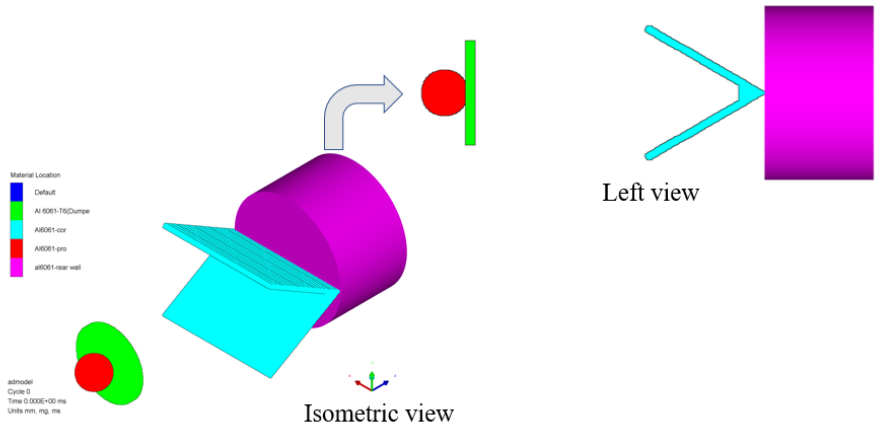

Figure 5.3 Numerical model of solid corner design

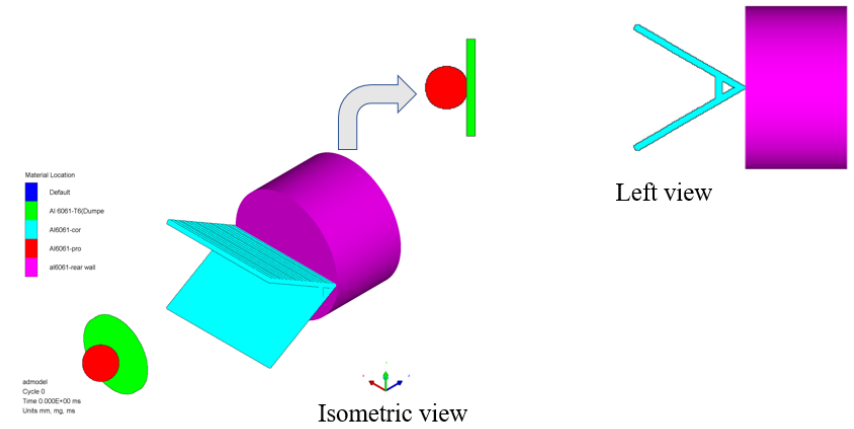

Figure 5.4 Numerical model of straight web design

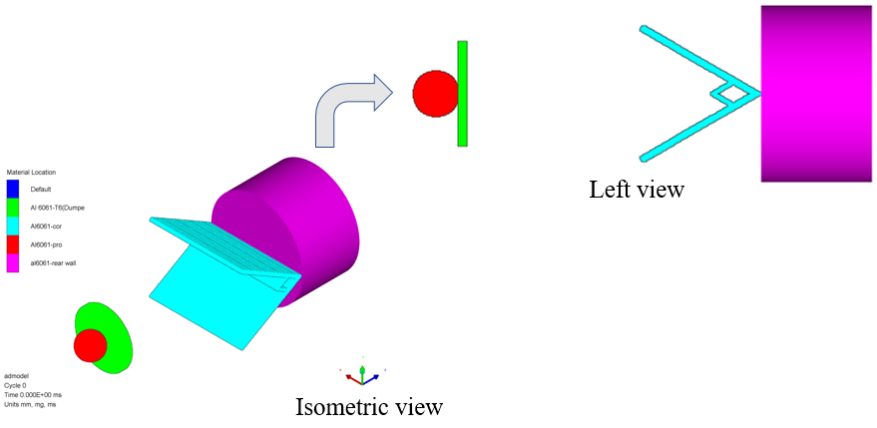

Figure 5.5 Numerical model of angular web design

5.1.2 Results

As shown in Table 5.1, the design with the "ridge" at the corner outperforms the configurations with the solid corner and flat web. The addition of the "ridge" to the valley corner leads to greater fragmentation and dispersion of the debris particles. In comparison to the flat web configuration, the design with the "ridge" resulted in a 27.7% reduction in the depth of damage in the semi-infinite rear wall. It also had a 11.8% reduction in damage compared to the configuration with the solid corner.

Table 5.1 Crater depth from various designs placed at the valley of CC

Design	**Depth of crater in the semi-infinite rear wall**
Solid corner	5.0 mm
Flat web	5.71 mm
"Ridge"	4.47 mm

5.2 Parametric Study of Selected Design

As demonstrated in the previous section, the "ridge" design was found to be the most effective at dispersing fragmentation and reducing damage depth among the configurations considered. This section examines additional variations of the "ridge" geometry to determine the most promising solution. Five different "ridge" geometries, along with their parameters, are shown in Fig. 5.6. The effect of the "ridge" position was also evaluated. The areal density was kept constant for all the proposed designs. In this study, both the "ridge" and the corrugated core plates had the same thicknesses.

The methodology for this study was similar to that used in the creation of the numerical model in section 5.1.1. A semi-infinite rear wall was used in place of the rear face sheet. Numerical HVI testing was conducted on configurations with selected core geometries. The depths of the deepest craters that occurred in the semi-infinite plate are presented in Table 5.2.

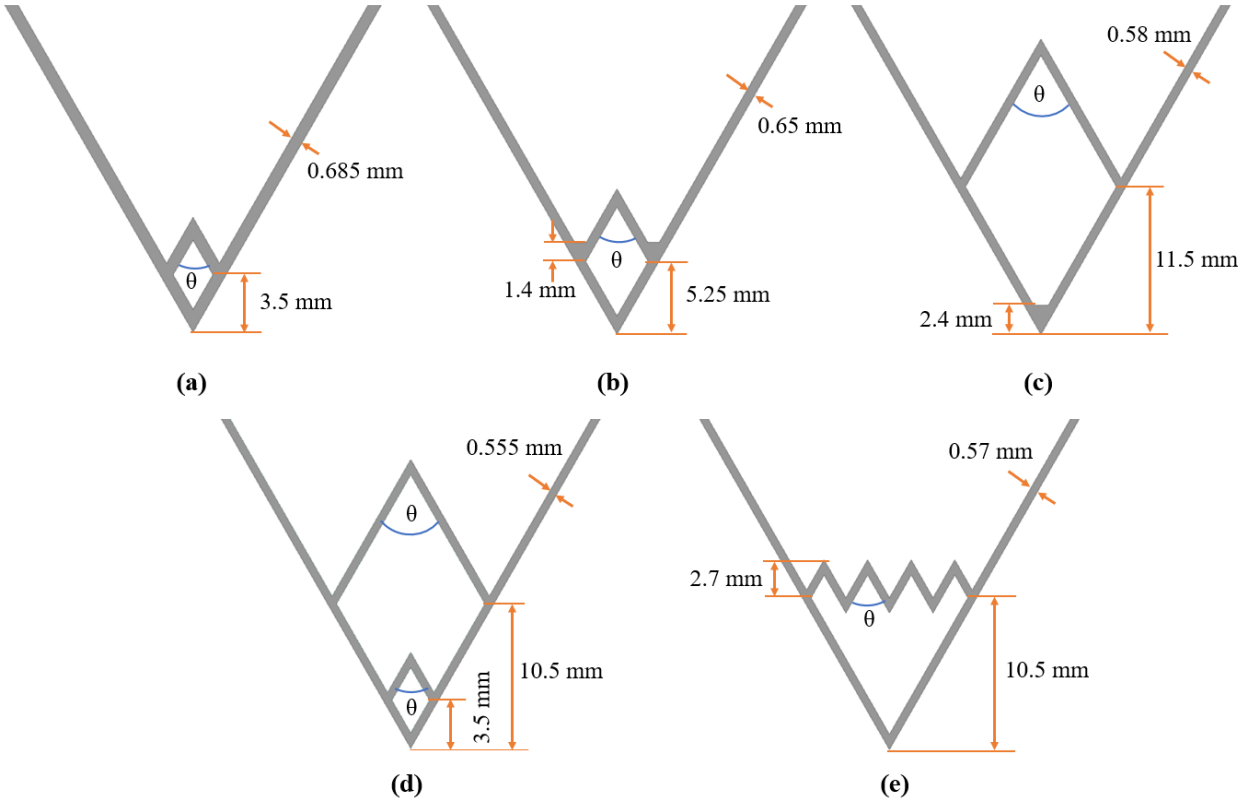

Figure 5.6 Different geometries of the "ridge" at the "valley" corner

Table 5.2 Crater depth from different "ridge" configurations

"Ridge" geometry	**Crater depth, mm**
(a)	4.37
(b)	6.157
(c)	7.08
(d)	5.7
(e)	9.025

Following the identification of type "a" geometry as the most effective, additional research was conducted on the configurations shown in Fig. 5.7 to determine the position of the "ridge" that would provide better fragmentation of the debris particles. The calculated crater depth for the "ridge" positions i, ii. iii and iv are shown in Table 5.3.

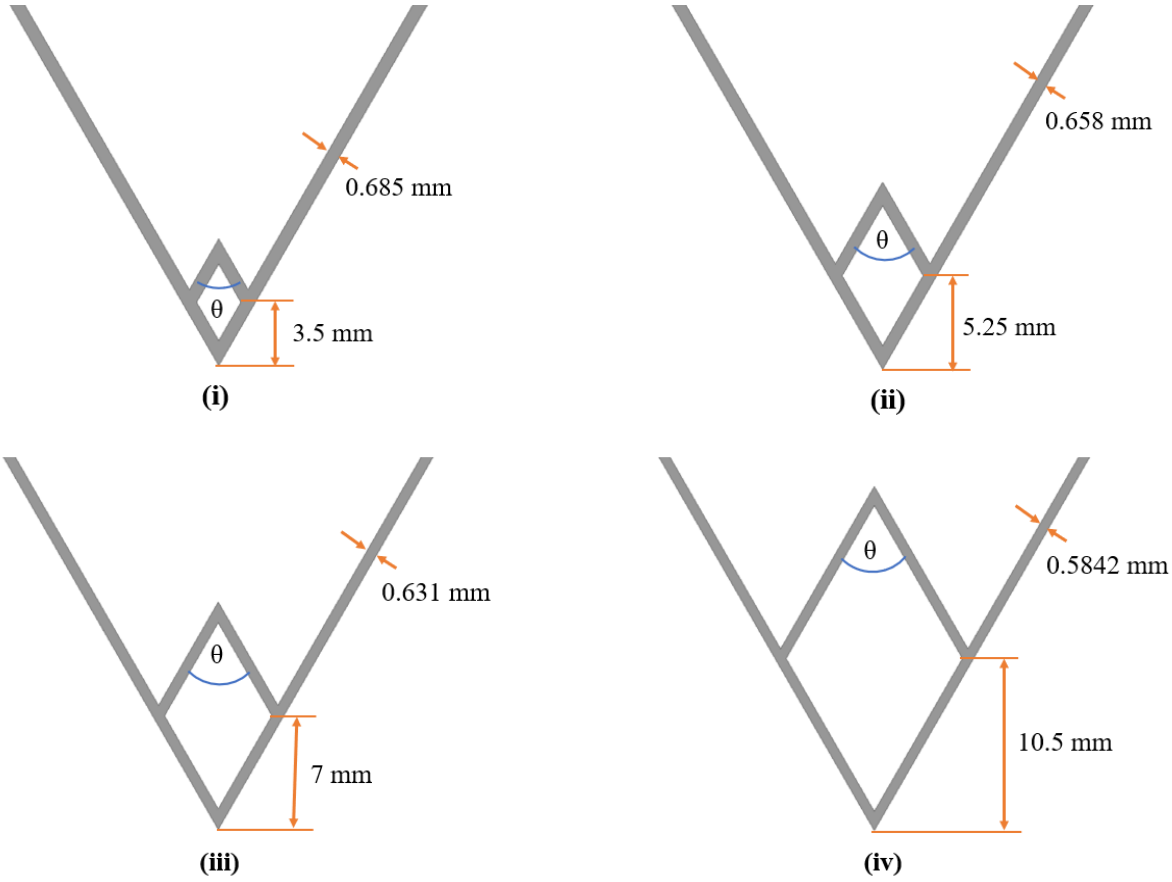

Figure 5.7 Evaluated positions of the "ridge"

Table 5.3 Crater depth from different locations of "ridge" at the valley of CC.

Position of the "ridge", mm	**Crater depth, mm**
(i) = 3.5	4.37
(ii) = 5.25	4.19
(iii) = 7	4.65
(iv) = 10.5	7.1

Out of four selected "ridge" positions, position "ii" at 5.25 mm performs the best. Shielding effectiveness tends to decline gradually if the distance of the "ridge" from the rear wall is less than or greater than 13% (5.25 mm) of the CC plate thickness.

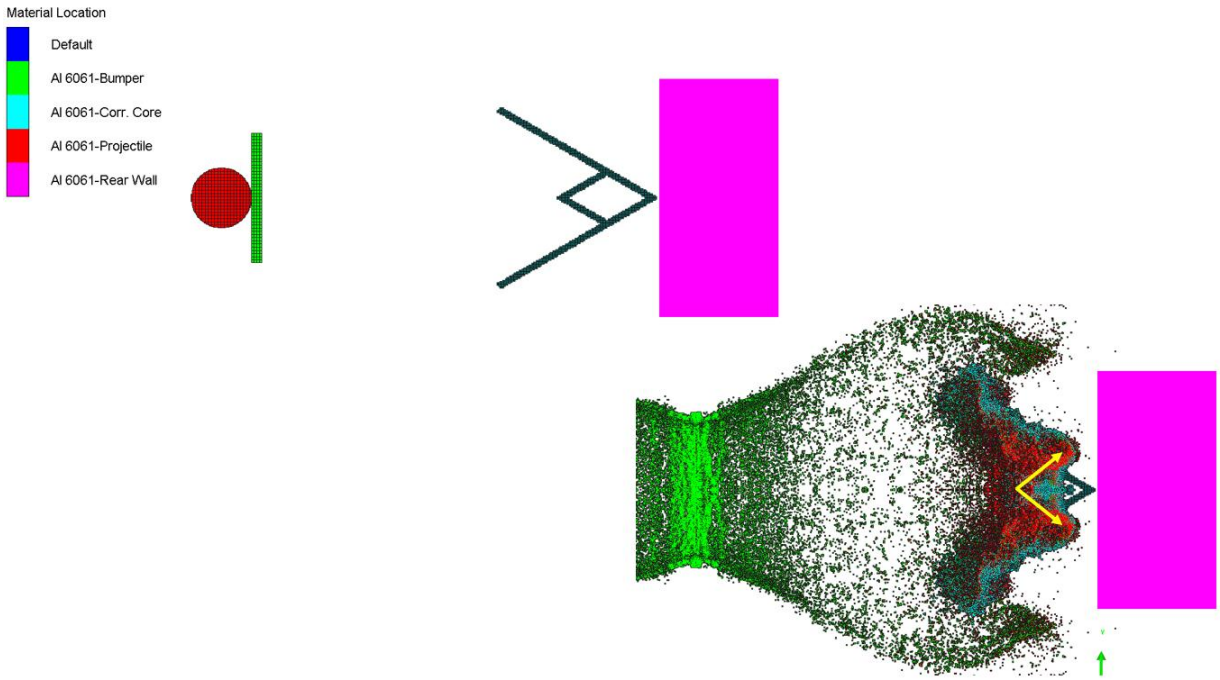

Figure 5.8 Numerical simulation of CC configuration with a "ridge" at 5.25 mm from the semi-infinite rear wall

"Ridge" design outperforms flat web and solid design at the CC valley by spreading the debris cloud in two directions as shown in Fig. 5.8. However, the "ridge" design does not perform well at the CC peak point. The debris cloud continues to display the same traits as described in section 4.4, with the cloud splitting into three clouds of fragments (Fig. 5.9). The core portions of the cloud still have fragments with higher momentum that have penetrated the back wall. A similar scenario can be observed if a flat web is mounted at the peak.

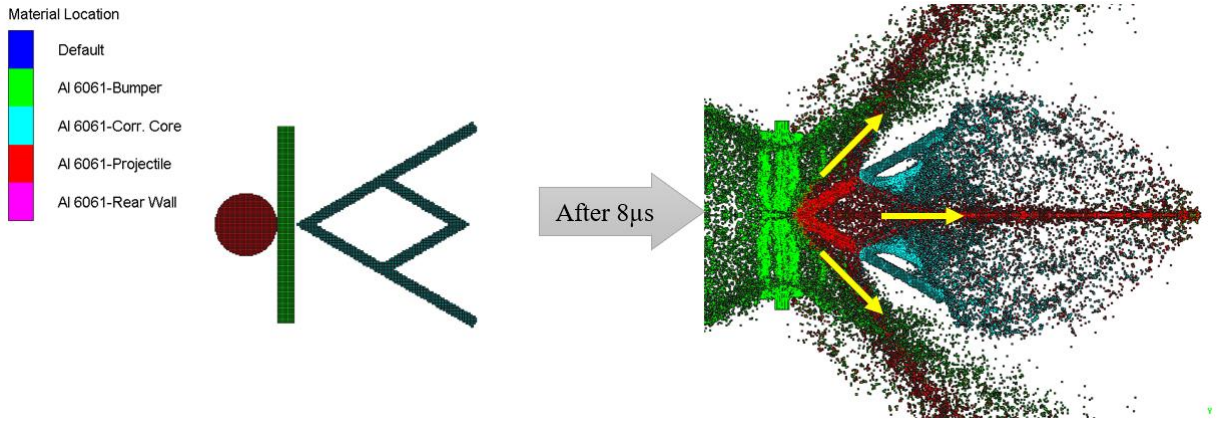

Figure 5.9 Demonstrate the 3 tongue debris clouds generated after interaction with the angular web at the CC peak point

However, by utilizing a solid corner, it was possible to avoid the creation of a center tongue with a higher momentum debris cloud, as shown in Fig 5.11, which the collision of the peak of the CC would have generated. There are 6.5703 mm^2 of space devoted to the "ridge" (ii) layout. The same area was utilized in the design of the solid corner and installed at the CC vertex so that the area density does not change, as can be shown in Fig. 5.10.

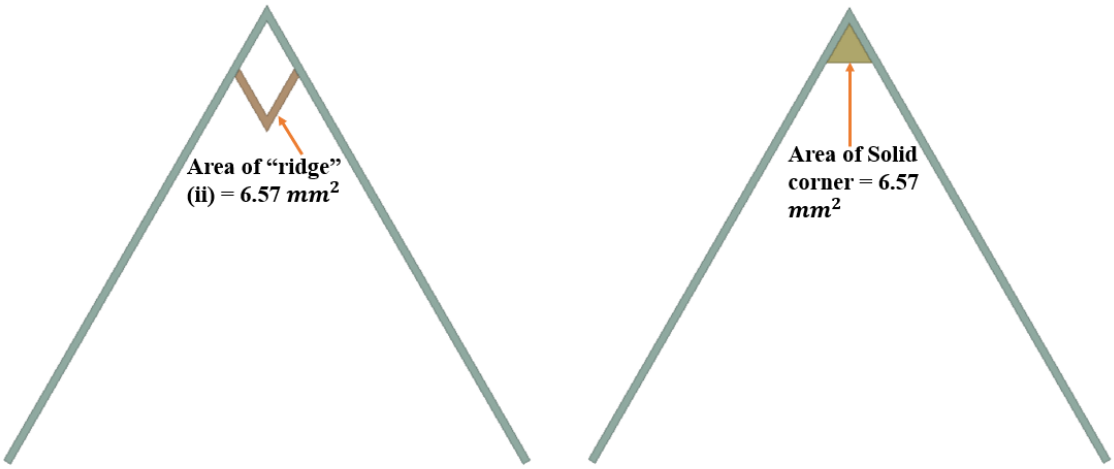

(a) Ridge (ii) design (b) Solid corner design

Figure 5.10 Adding the same quantities of material in the solid corner as the "ridge" (ii) layout

Adding more material to the peak corner of the corrugated core decreases the overall momentum of the central "tongue" of the debris cloud. Additionally, the solid corner configuration results in the debris cloud spreading over a larger area. Therefore, the solid corner design at the peak of the CC provided better fragmentation of the debris cloud compared to the "ridge" design.

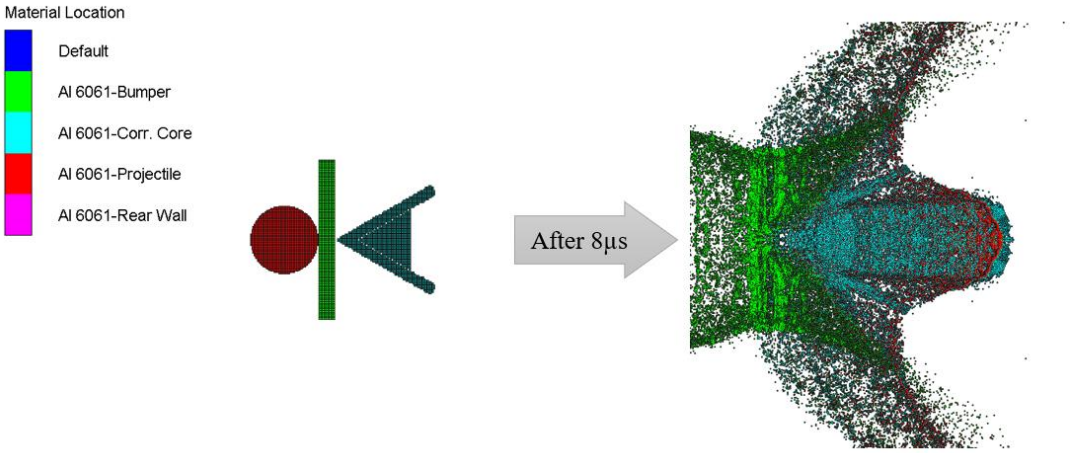

Figure 5.11 The debris cloud shape after interaction with a solid corner at the CC peak

5.3 Performance of Enhanced CCSP Configuration

Earlier research on the CCSP showed that the "valley" and "peak" areas of the CC were the most vulnerable to HVI, as discussed in section 4.4. In order to improve the performance of these positions, the enhancement procedure was applied. The numerical setup mentioned in section 3.1.4 was employed to conduct the study. Based on the results of the study in section 5.2, it was determined that the configuration with the "ridge" at the valley and the solid corner at the peak of the CC were able to improve the shielding effectiveness of the panel. Fig. 5.12 shows the initial and enhanced geometries of the CCSP.

The comparison between the modified and initial CCSP shows that the protection level is significantly improved in the position across the "valley" when the "ridge" is positioned at 5.25 mm from the rear facesheet. However, the "ridge" design did not significantly improve the performance of the peak area of the CC. In contrast, the solid corner significantly improved the shielding performance when used at the peak of the CC. Fig. 5.13 demonstrates the effect of the modified core geometry on the critical diameter for the CCSP.

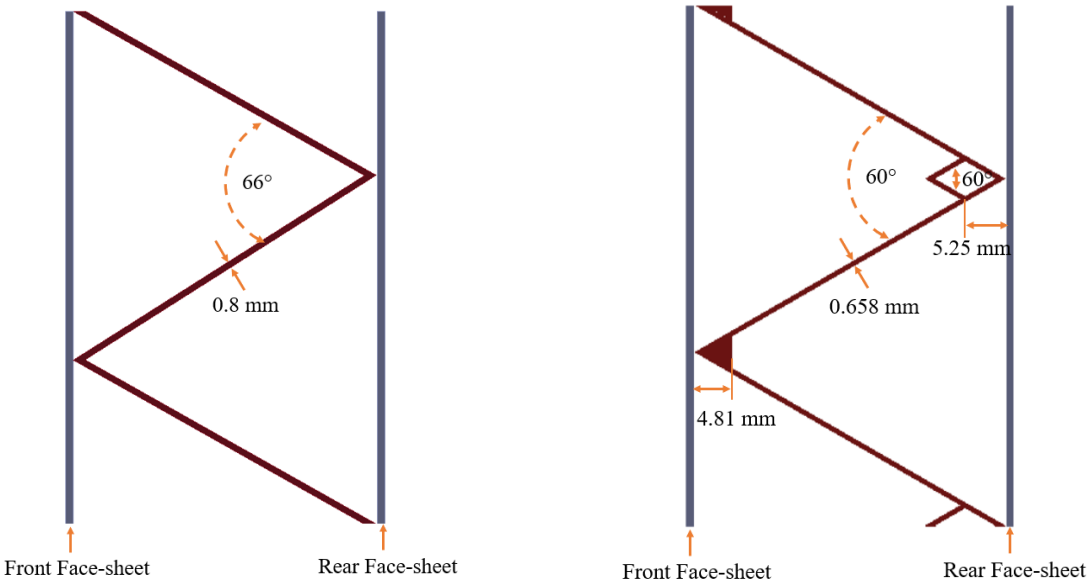

a) Initial CCSP geometry b) Enhanced CCSP geometry

Figure 5.12 Geometry of a) Initial corrugated core and b) Enhanced corrugated core

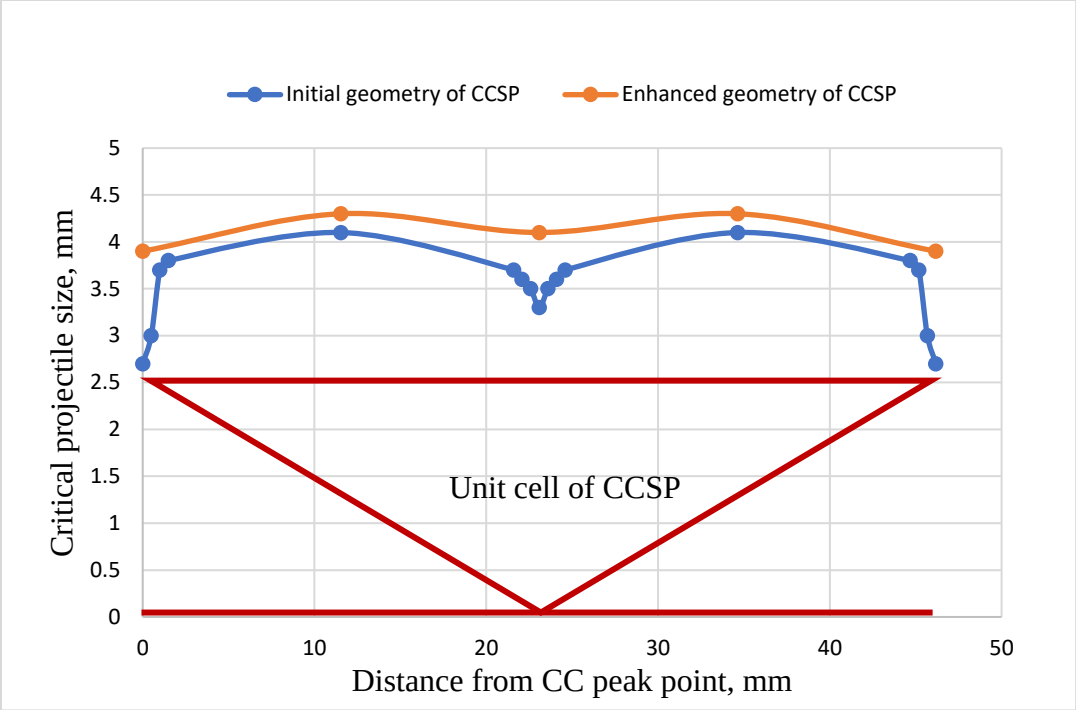

Figure 5.13 Critical diameter of projectile throughout the initial and enhanced CCSP

This improvement in protection level is achieved through the increased fragmentation and wider dispersal of the debris cloud as it interacts with the added elements at the peak and valley of the CC. For example, when a projectile impacts the valley of the CC, the "ridge" design can split the debris cloud into two different directions, decreasing the overall momentum of the debris cloud and improving the shielding performance, as demonstrated in Fig. 5.14. The enhanced CC geometry with the "ridge" design (ii) increases the critical diameter size by 24% at the valley compared to the initial geometry. In comparison to the initial geometry, the use of the solid corner design increased the critical diameter size at the peak of CC by 44%, as shown in Fig. 5.15.

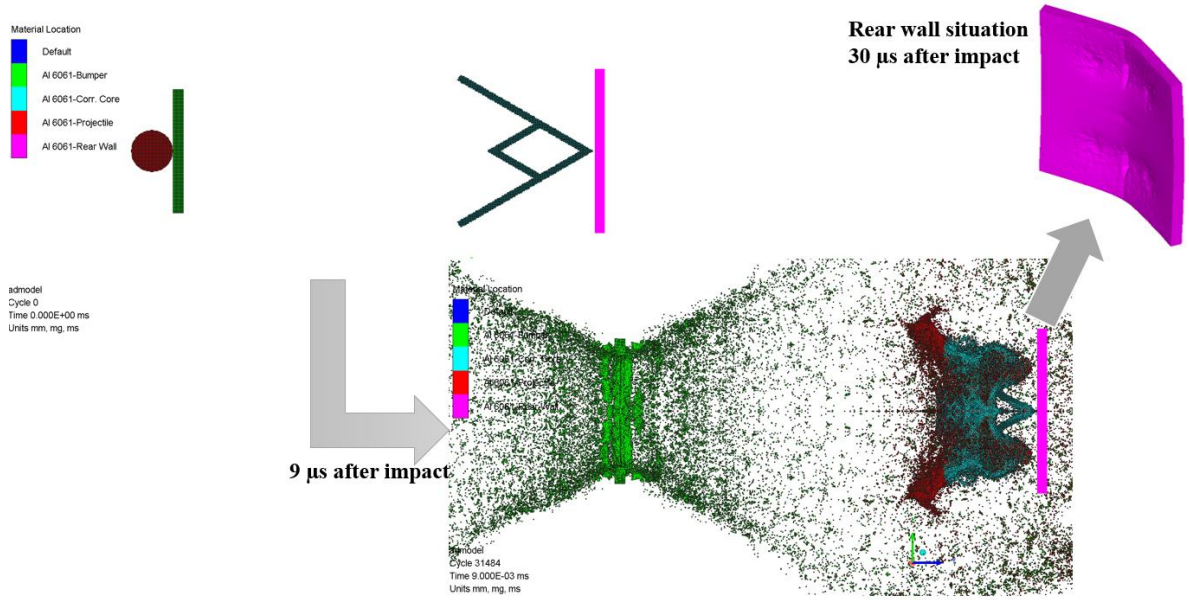

Figure 5.14 Simulation result when a 4.1 mm projectile hit in the direction of the valley of enhanced geometry of CCSP at 7 km/s

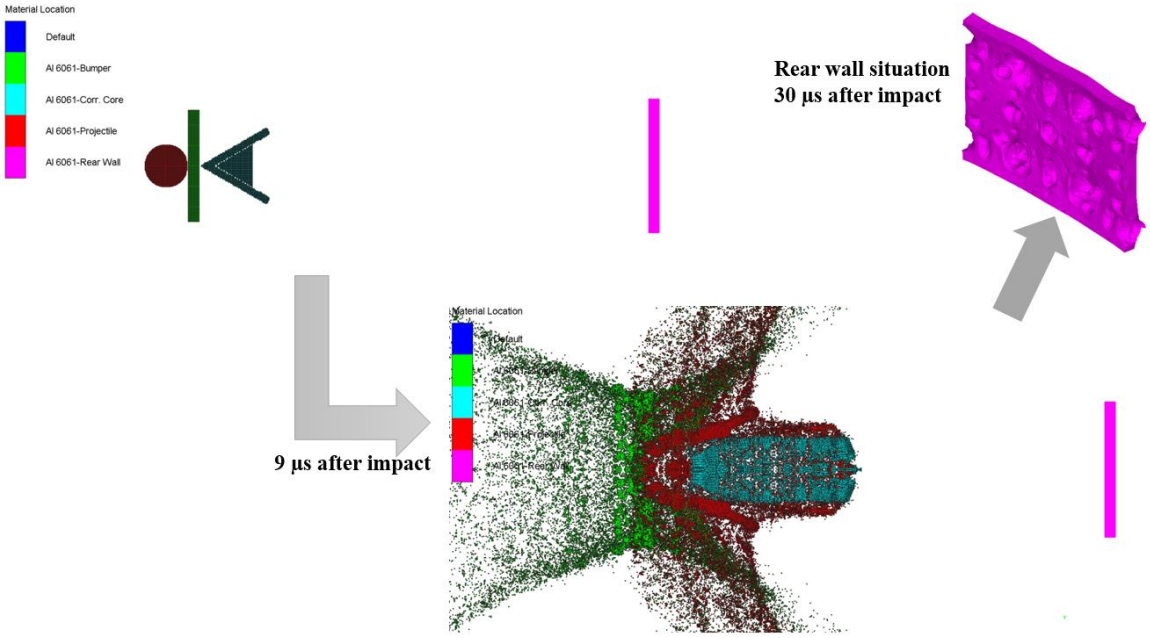

Figure 5.15 Simulation result when a 3.9 mm projectile hit in the direction of the peak of enhanced geometry of CCSP at 7 km/s

5.4 Summary of Chapter

The study resulted in the development of an improved corrugated core geometry that provides superior shielding compared to the CCSP with the original core geometry. By using a “solid corner” and "ridge" at the "peak" and "valley" of the CC, respectively, the vulnerability of these impact locations is effectively addressed. As a result, the enhanced geometry of the CCSP is able to provide consistent MMOD protection, with a flattened variation of the critical diameter (ranging from 3.9 mm to 4.3 mm) across the panel.

6. EFFECT OF BALLISTIC FABRICS

The present study demonstrated that a custom-engineered corrugated core enhances the shielding performance of CC sandwich panels. Furthermore, the shielding performance can be enhanced further with ballistic inserts containing layers of ballistic fabrics, e.g., Basalt fabric, Nextel, and Kevlar.

Several studies [67] - [69] undertaken by NASA, ESA, and CNSA demonstrate that ballistic fabric can increase a space debris shield's effectiveness. This fabric is typically inserted between the bumper (front facesheet) and rear wall (rear facesheet) and works as a second bumper. The ballistic fabric adds a further shock and pulverizes the debris cloud. Thus, the momentum density per unit area of the debris cloud is reduced such that any fragments reaching the rear wall are benign [70]. Besides, ballistic fabric layers do not contribute additional fragments to the debris cloud [71]-[75].

Ballistic inserts can be fabricated from lightweight polymeric foam in the shape of a triangular prism fitting the dimensions of the empty space within the corrugated plate core. The ballistic property of the inserts can be adjusted to comply with the specific mission's safety and operational requirements, making this configuration more manageable and universal.

This study is focused on using basalt fabric as a possible option among the other alternatives available. Basalt is a naturally occurring material found in volcanic rock. Basalt fabric's properties make it a suitable material for shielding against MMOD [76]. The effect of the ballistic inserts on CCSP shielding performance is assessed in the following paragraphs. The methodology for this study was similar to that used in the creation of the numerical model in section 5.1.1. For basalt fabric. 0.1 mm SPH particle was assigned.

In this study, we will focus on using basalt as a possible option among the other alternatives available. The subsequent paragraphs will evaluate the effect of these ballistic inserts on CCSP shielding performance.

6.1 Ballistic Fabric Layout

The goal of this study was to determine an arrangement of ballistic fabric that effectively improves the fragmentation of debris and decelerates the debris cloud.

6.1.1 Description of the Numerical Model

To conduct the study, numerical model of enhanced CCSP configuration with ballistic inserts was developed. Three positions within the core were selected, as shown in Fig 6.1 (a), (b), and (c), to install the basalt layers.

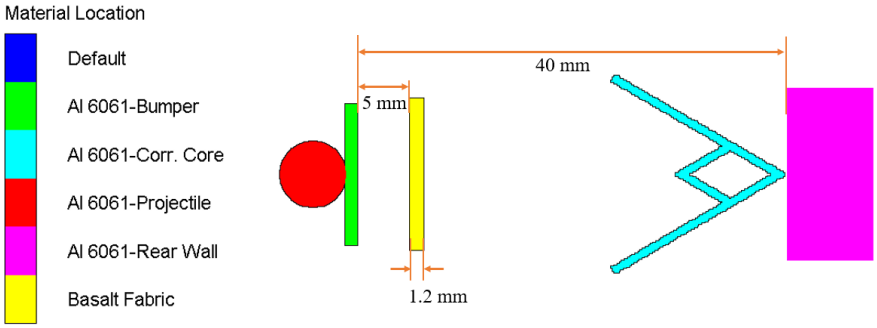

a) Enhanced CCSP configuration with 1 basalt layer close to the front facesheet

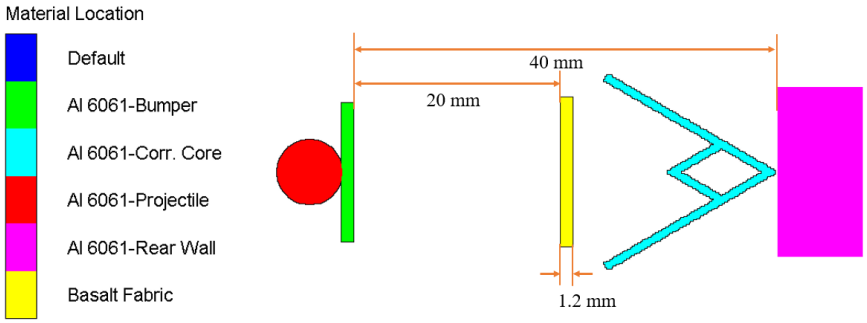

b) Enhanced CCSP configuration with 1 basalt layer close to the center of the panel

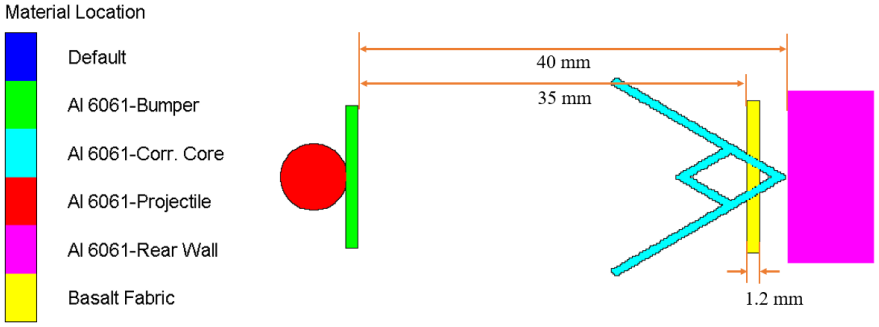

c) Enhanced CCSP configuration with 1 basalt layer close to the rear facesheet

Figure 6.1 Installing one basalt layer in a different location in the middle of the Enhanced CCSP configuration

The panel has 1 mm front facesheet, 0.658 mm CC plate thickness and a semi-infinite rear wall. Each basalt layer was 1.2 mm thick and made by McMASTER-CARR. After simulating each layout, the depth of the deepest crater that resulted on the semi-infinite rear wall was defined to identify the most favorable position of fabric to be installed.

6.1.2 Evaluation

The damage patterns for various positions of basalt fabric layers are illustrated in Fig. 6.2. When the ballistic fabric was positioned close to the front face sheet (5 mm after the front face sheet), a large crater with a depth of 6.075 mm was observed in the center of the semi-infinite rear wall. When the basalt layer was positioned in the center of the core, the damage pattern on the rear wall remained roughly the same, with the deepest crater of 4.79 mm observed aside from the center, representing a 21% decrease from the result for basalt near the front face. When the basalt fabric was placed close to the rear wall, the major crater depth of 7.21 mm occurred at the lateral part of the semi-infinite rear wall, 50% more than the depth observed when the basalt was positioned in the center of the panel thickness.

Thus, the second scenario, illustrated in Fig. 6.1 (b), exhibited the most effective shielding performance. This is likely because the fragments produced by the front facesheet were given ample space to expand before they came into contact with the basalt layer, and the fragments produced by the basalt layer were likewise given sufficient room to expand before interacting with the rear wall.

This finding is consistent with the numerical results obtained using the AUTODYN tool, which indicated that most of the fragmentation occurred in the debris cloud when the basalt layer was positioned in the center of the core (with a total of 43890 fragments). Placing the basalt fabric in close proximity to the front facesheet resulted in the second-highest number of fragments (41444 fragments), while placing it closest to the rear wall resulted in the fewest instances of fragmentation in the debris cloud (24572 fragments).

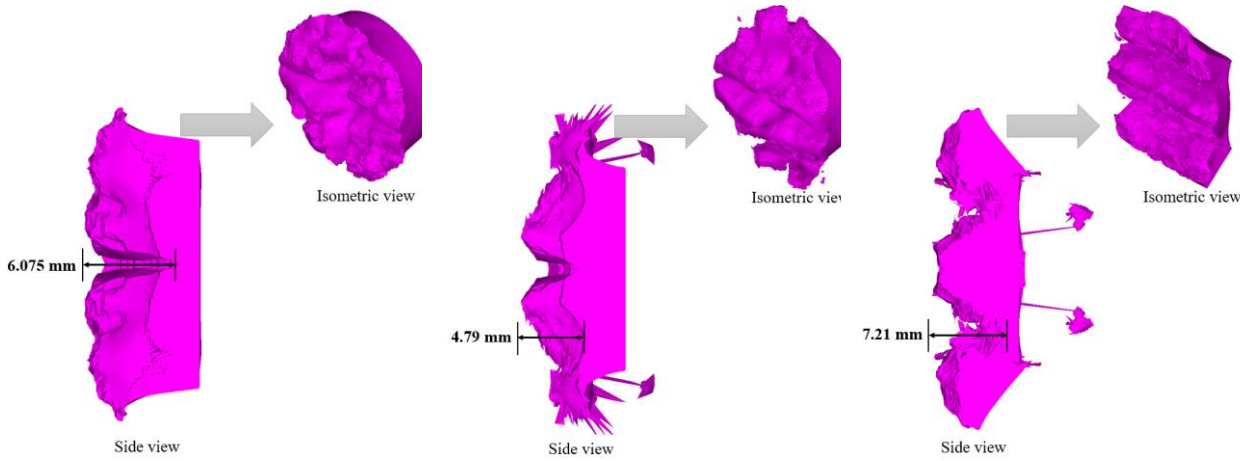

a) Basalt near to front facesheet

b) Basalt in the center of the panel

c) Basalt near to rear facesheet

Figure 6.2 The crater depth in the semi-infinite rear wall

6.2 Effect of Ballistic Fabric Thickness

It was found in the previous section that inserting ballistic fabric in the center of the sandwich panel provides better shielding performance than placing it close to the front and rear facesheets. The aim of this study is to determine how the thickness of the ballistic fabric affects performance. Two models were simulated using the same configuration as the previous section, with the exception of the number of basalt layers. The first model had 2 basalt fabric layers, and the second had 3 basalt fabric layers in the center of the panel. Fig. 6.3 illustrates the decrease in crater depth as the number of basalt layers is increased. As compared to the enhanced panel with only one basalt layer, the crater depth is reduced by 42.79% and 66.38% when two and three basalt layers are inserted, respectively.

However, as the number of layers of basalt fabric in the panel increases, the panel becomes heavier. By examining the relationship between the crater depth and the panel's areal density, the weight efficiency of the panel can be assessed. Several weight-efficient approaches for improving shielding protection will be discussed in the following section.

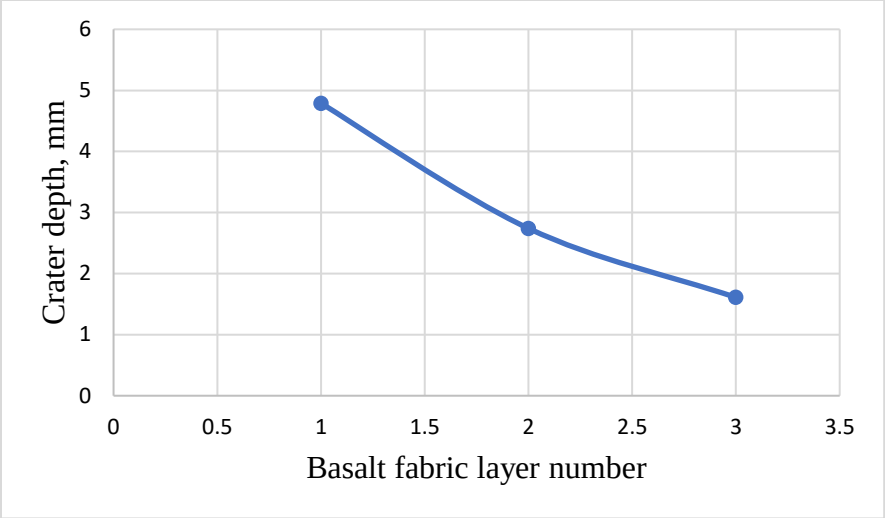

Figure 6.3 Effect of basalt fabric layer in the shielding performance

6.3 Weight-Efficient Approach for Improving the Protection Level

6.3.1 Description of Model Geometry

The initial and the enhanced CCSP configurations have the same areal density (9.41kg/m^2). The enhanced configuration provides protection with a smooth variation of the critical diameter ranging from 3.9 mm to 4.3 mm across the surface. Various approaches can be taken to further improve the performance of the panel, such as inserting ballistic layers and thickening CC plate.

The basalt layers have an areal density of 1.67 kg/m², improve the shielding performance of the panel by providing secondary fragmentation and energy absorption of the debris. However, this improvement comes at the cost of significantly increasing the panel's areal density. Similarly, increasing the thickness of the CC plate results in a higher level of protection but also increases the weight of the panel. In both cases, weight is increased, so it is essential to find the most efficient way to enhance the protection level while minimizing the weight increase. The numerical model had 0.07 mm and 0.1 mm SPH particle size from projectile, front facesheet and Corrugated core, Basalt fabric respectively. For the rear facesheet, 0.2mm mesh size was employed.

Fig. 6.4 shows the configurations and their corresponding areal densities for the three approaches evaluated in this study. The first approach involved placing ballistic inserts made of basalt fabric in the center of the initial CCSP, while the second approach involved placing the basalt fabric in

the center of the enhanced CCSP. The third approach was to increase the thickness of the CC plate in the initial CCSP without using any additional elements.

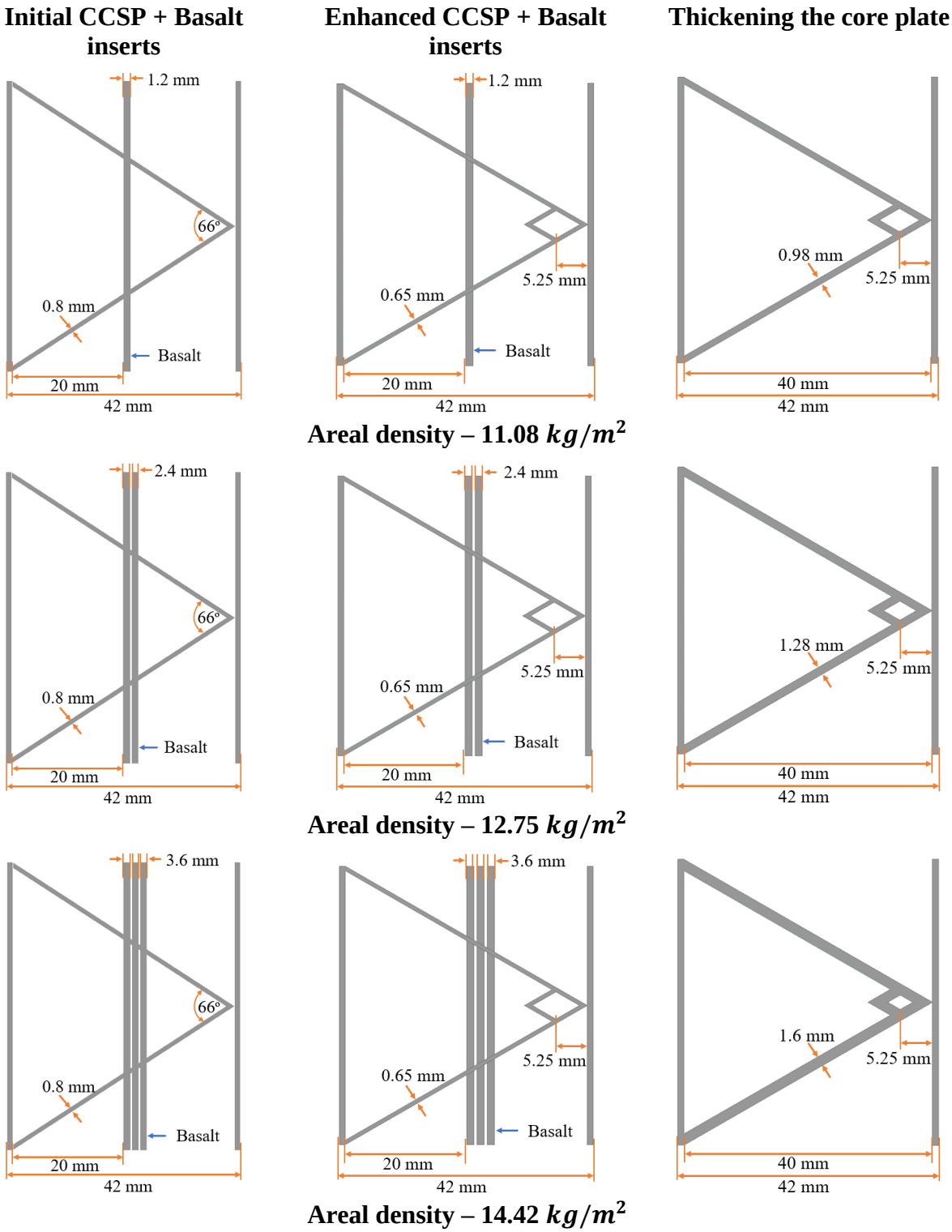

Figure 6.4 Geometry of enhanced CCSP model with and without ballistic fabric

6.3.2 Performance Evaluation

Numerical HVI testing was conducted on the candidate configurations, and the results, as illustrated in Fig. 6.5, showed that as the areal density increased in each approach, the depth of the resulting crater decreased. Specifically, the second approach, in which basalt layers were added in the center of the enhanced CCSP, resulted in a crater depth that was roughly 148% lower than the initial CCSP configuration with basalt layers. However, thickening the enhanced core plate resulted in a 102.6% reduction in crater depth but still 22.3% more than the enhanced CCSP with basalt layers. Figure 6.5 illustrates the crater depth for the three different approaches at varying areal densities. Therefore, the most weight-efficient way to improve the protection level of the CC sandwich panel among these three approaches is to use the combination of ballistic fabric and additional elements, such as a solid corner and a "ridge" at the CC peak and valley points.

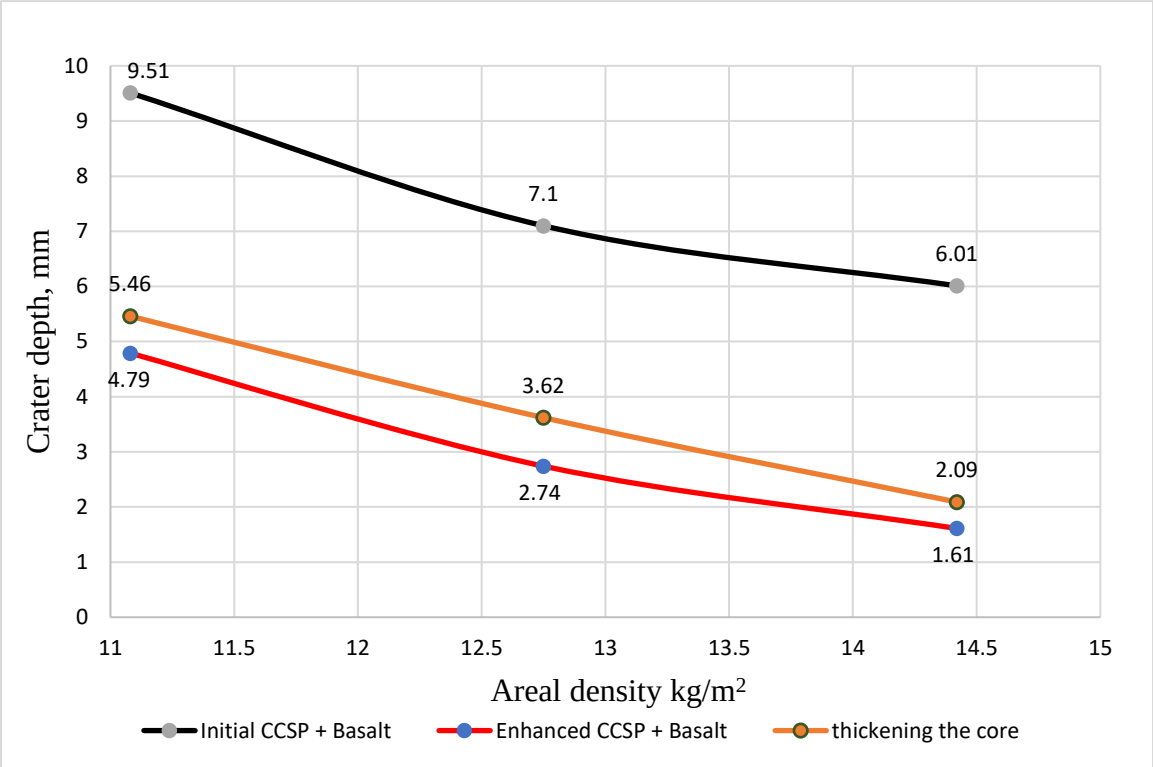

Figure 6.5 The shielding performance of three CCSP candidate configurations

6.4 Required Protection Level

Previous studies have shown that the enhanced CCSP configuration, with a "ridge" at the valleys and a solid corner at the peaks, can prevent complete perforation by a projectile with a critical diameter ranging from 3.9 mm to 4.3 mm across the panel.

This section aimed to analyze the way in which the MMOD protection capability of CCSP could be enhanced more efficiently to withstand a 5.16 mm spherical aluminum projectile at 7 km/s. The choice of impact parameters reflects the requirements for MMOD protection of robotic spacecraft such as RCM spacecraft [77]-[79] designed to operate for seven years in a nearly polar orbit at an altitude of approximately 600 km. The methodology for this study was similar to that used in the creation of the numerical model in section 6.3.1.

6.4.1 CCSP Configuration to Withstand HVI at CC Valley Point

In this subsection, the numerical model of Enhanced CCSP with basalt fabric in the center of the core was used for the analysis. The thickness of the basalt was increased until the rear facesheet (1 mm thick) completely stopped a 5.16-mm projectile at 7km/s. One basalt fabric is 1.2 mm thick. Thus, the thickness was increased by adding more layers. The results of the simulations indicated that two layers of basalt fabric (2.4 mm) are sufficient to prevent perforation of the panel by a 5.16 mm projectile. The rear facesheet experienced a significant bulging, but no perforation occurred. Fig. 6.6 shows the numerical model of the evaluated configuration and the damage to the rear facesheet after the impact.

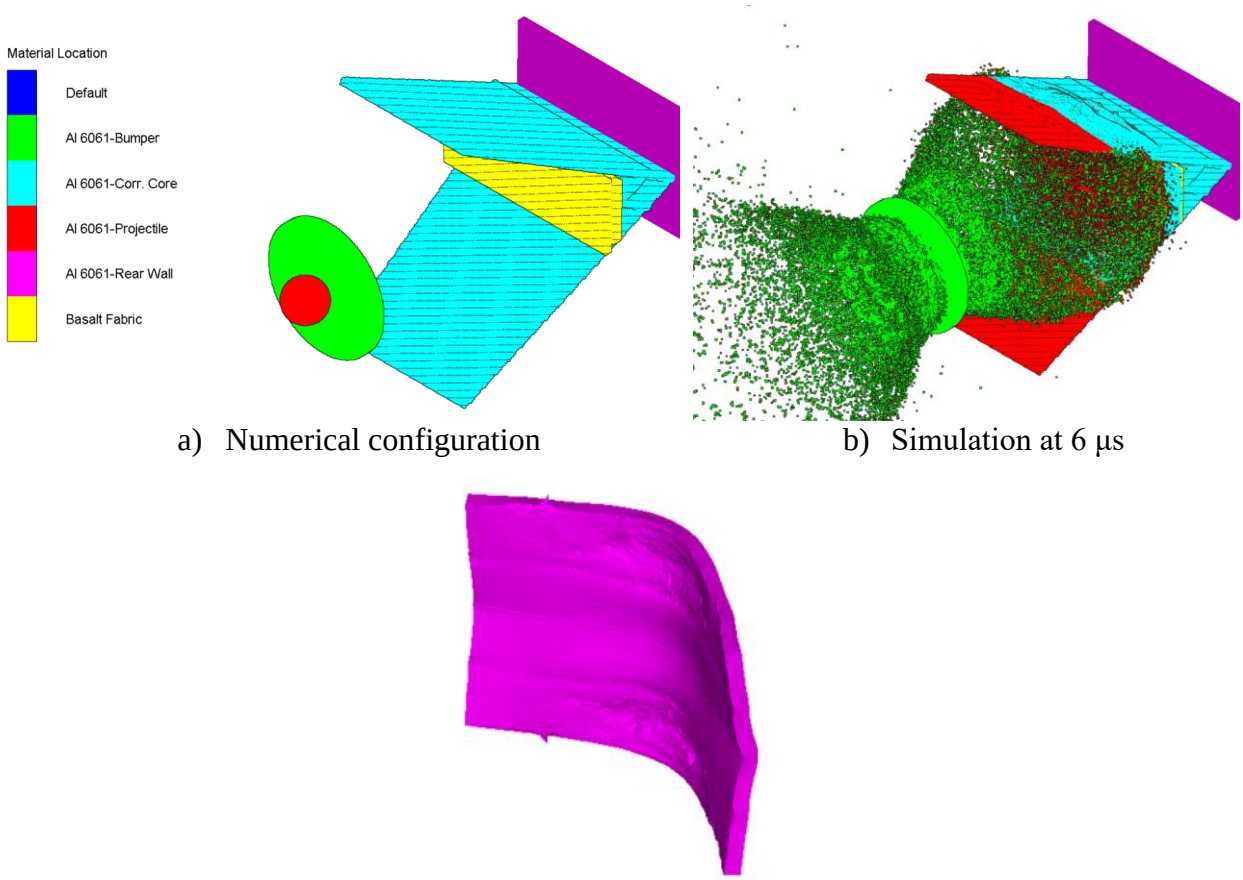

a) Numerical configuration

b) Simulation at 6 μs

c) Rear facesheet situation at the simulation

Figure 6.6 The numerical configuration of the enhanced CCSP model with 2 basalt layers to stop a 5.16 mm projectile at the valley of CCSP.

6.4.2 CCSP Configuration to Withstand HVI at CC Peak Point

In this subsection, a similar approach as in the previous subsection was taken to determine the thickness of the basalt layer required to stop a 5.16 mm projectile that impacts the peak of the corrugated plate. The results of the numerical simulation were consistent with those obtained in the earlier subsection (6.4.1), where it was found that two basalt layers (2.4 mm thick) are sufficient to prevent perforation by a 5.16 mm projectile that impacts the peak of the corrugated plate. Fig. 6.7 shows the numerical test setup and the simulated damage to the rear facesheet.

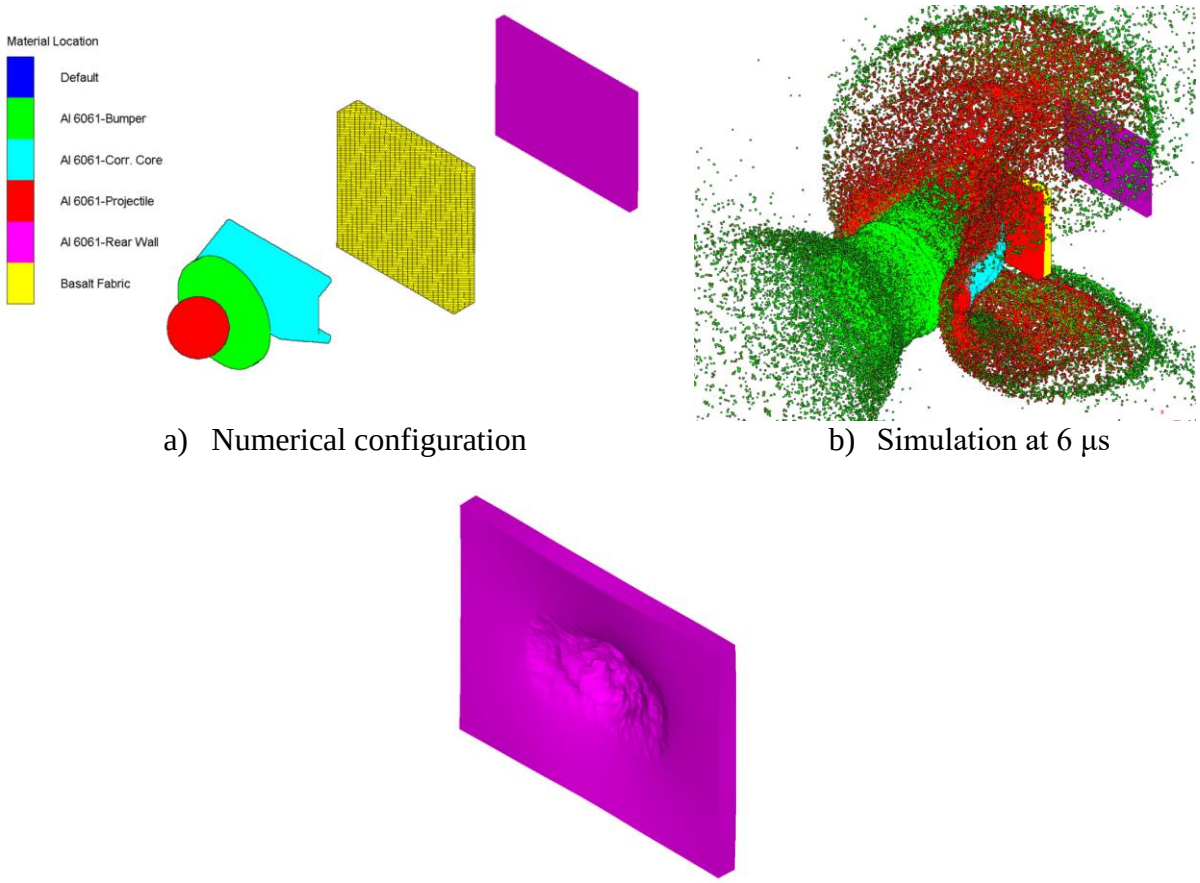

a) Numerical configuration

b) Simulation at 6 μs

c) Rear facesheet situation at the simulation

Figure 6.7 The numerical configuration of the enhanced CCSP model with 2 basalt layers to stop a 5.16 mm projectile at the peak of CCSP.

6.5 Summary of Chapter

This chapter examined the impact of ballistic fabric on the shielding performance and weight of the CCSP. It was found that placing the ballistic fabric in the center of the panel leads to improved fragmentation and consequently reduced damage to the back facesheet. The level of protection increases as the thickness of the ballistic fabric increases. Of the three approaches for further enhancing the shield performance, inserting basalt layers in the enhanced CCSP was found to be the most weight efficient. Finally, it was determined that the enhanced CCSP model required the addition of two basalt layers in the center of the panel for protection against a 5.16 mm projectile at 7km/s at any point within the CCSP surface. The required areal density to protect a 5.16 mm projectile is 12.75 kg/m^2. However, if the CC plate of the initial configuration is thickened to protect a 5.16 mm projectile, the required areal density increases to 23.46 kg/m2.

7. CONCLUSION AND FUTURE WORKS

Due to the rapid increase in orbital debris, all types of spacecraft would require enhanced protection from orbital debris impact to complete their missions successfully. Current work employed the ENSURE-concept introduced by the UM-ORDER Group, which is based on the idea of redesigning the original structural parts, such as the structural panel, to enhance their inherent protection capability without the prohibitive additional weight.

The corrugated core sandwich panel (or CCSP) is a promising candidate for a lightweight and versatile sandwich panel with excellent structural integrity and potential for other functional purposes, including protection against orbital debris impact. While CCSP's structural performance has been established, its MMOD protection capabilities have not been thoroughly investigated.

This thesis focused on evaluating the CCSP's ballistic shielding capabilities using a numerical technique validated with experimental data and identifying potential approaches for improving ballistic protection. The conclusion derived from the overall objective of this study is presented in the following areas: 1) Model development and validation; 2) Identification of most vulnerable regions within the CCSP; 3) Enhancement of the shielding performance of CCSP.

To model CCSP in a 3-D domain, a combination of SPH and FEM was used; this approach helps reduce each method's drawbacks to an acceptable level with minimum error. Following a thorough parametric investigation, the appropriate numerical model data, material model parameters, and impact conditions were determined and validated using experimental data with a margin of error of less than 10%.

An examination of the geometrical properties of CCSP supported by the numerical analysis revealed that the regions in the vicinity of the CC peak and valley points are highly vulnerable to hypervelocity impact. Therefore, it was concluded that in order to preserve CCSP's multifunctional potential and enhance its ability to withstand more significant threats, both the "peak" and "valley" regions of the panel's design must be improved.

A range of potential solutions was created and assessed to determine their effectiveness in enhancing the CCSP's ballistic protection without compromising the panel's structural integrity.

After conducting a comprehensive analysis, it was determined that incorporating a solid corner at the peak and a ridge at the valley of the corrugated core was an effective measure to mitigate the susceptibility of these impact areas.

Using the solid corner design at the peak increased the critical diameter size by 44 percent compared to the initial CCSP design. At the valley, the "ridge" design increases the critical diameter size by 24%. The enhanced CCSPs with a solid corner and "ridge" can provide consistent protection regardless of impact location. Compared to the initial CCSP, the enhanced configuration boasts a 44.4 percent increase in the minimum critical diameter required to penetrate the CCSP with a projectile. Specifically, the minimum critical diameter has been raised from 2.7 mm to 3.9 mm.

Furthermore, the impact of integrating basalt fabric as a toughening material in the CCSP was studied. The most effective placement of the toughening material was determined, and a parametric analysis was conducted to evaluate the impact of varying the toughening material's thickness on the panel's ballistic performance. The study's outcome indicated that placing the ballistic fabric in the center of the core leads to improved fragmentation and expansion of debris cloud and consequently reduced damage to the target structure of the spacecraft. Additionally, the shielding efficacy increases with basalt fabric thickness and converges to a certain point. After this increase, the thickness of basalt doesn't improve the protection level noticeably.

Having understood the ballistic protection capabilities of CCSP, the effect of corrugated core angle on CCSP's structural integrity and shielding performance was numerically evaluated using a 3-point bending test procedure. According to the study's findings, structural stiffness improves when the angle of the structure is reduced. On the other hand, it was discovered that the level of protection offered by CCSP improves with an increase in the angle of the corrugated core.

To conclude, this study has effectively demonstrated the ballistic shielding capability of the corrugated-core sandwich panel, while also recognizing the panel's exceptional structural integrity. Furthermore, to counteract the escalating threat of MMOD impact due to heightened human activities in space, methods for enhancing the panel's ballistic capability, such as utilizing ballistic inserts, were identified. The findings of this thesis can be employed to tailor the ballistic properties of these inserts to meet the specific safety and operational requirements of each mission, making this configuration more versatile and manageable.

7.1 Contributions to Knowledge

- A robust numerical model for simulating the corrugated core sandwich panel in three dimensions was developed with a combination of SPH and FEM. Three sets of HVI test data were used to validate the accuracy of the developed numerical model, demonstrating that it is suitable for the analysis of the CCSP model with an error margin of less than 10%.
- The investigation revealed that the normal impact (0 degrees) is the most dangerous direction, and the regions adjacent to the "valley" and "peak" points of the corrugated core are the most vulnerable zones for HVI. The minimal critical diameter of the initial CCSP configuration is 2.7 mm. After considerable research, a solid corner and "ridge" at the corrugated core's "peak" and "valley" reduce impact vulnerability. The enhanced CCSP configuration has a 44.4% higher minimal critical diameter (3.9 mm) than the initial arrangement without increasing the weight of the panel.
- To investigate the impact of ballistic fabric on the CCSP, two specific steps were taken: 1) Identifying the most suitable position to position the basalt fabric, and 2) Examining the influence of varying thickness levels of the basalt fabric. From that investigation, it was observed that placing the ballistic fabric in the center of the panel leads to improved fragmentation and expansion of debris cloud and consequently reduced damage to the back facesheet. Additionally, the shielding efficacy increases with basalt fabric thickness and converges to a certain point. After that increase, the thickness of basalt doesn't improve the protection level noticeably.
- To determine the most weight-efficient tactic for further enhancing the shield performance of CCSP, three approaches were presented. 1. Inserted basalt fabric with initial CCSP configuration; 2. Inserted basalt fabric with enhanced CCSP configuration; 3. Thickening the enhanced Corrugated core. It was observed that basalt layers in the center of enhanced CCSP were the most weight-efficient method out of the three different ways to further improve the shield's performance.
- Finally, it was determined that the enhanced CCSP model required the addition of two basalt layers in the center of the panel for protection against a 5.16 mm projectile at 7km/s. Compared to the areal density of the initial CCSP configuration capable of stopping 5.16 mm, the upgraded CCSP configuration with two basalts has 45.65 % less areal density.

7.2 Future Work

The main focus of this thesis is to explore the shielding performance of CCSP configurations and investigate and investigate how to improve the protection level in a weigh-efficient way. Through the conducted research, key trends in improving shielding performance were identified. Future studies will examine deeper the implementation of various materials and techniques to fabricate enhanced panels. Although the improved CCSP configuration exhibited significant advancements over the initial design, experimental testing is necessary to validate its performance. In addition, future research will evaluate the shielding performance and assess the structural integrity of the enhanced CCSP, both numerically and physically, and compare it with conventional sandwich panels.

REFERENCE

[1] https://www.esa.int/Space_Safety/Space_Debris/Space_debris_by_the_numbers

[2] N. Handbook, "National Aeronautics and Space Administration HANDBOOK FOR Measurement System Identification : Metric," 2013

[3] https://www.nasa.gov/mission_pages/station/news/orbital_debris.html

[4] Lambert, M., Shielding against orbital debris - a challenging problem, Proceedings of the ESA Symposium on "Space applications of advanced structural materials," 21-21 March 1990, ESTEC, ESA SP-303, 1990.

[5] Drolshagen G., Hypervelocity Impact Effects on Spacecraft, Proceedings of the Meteoroids 2001 Conference (ESA SP-495, November 2001), Swedish Institute of Space Physics, Kiruna, Sweden, 6-10 August 2001
https://www.esa.int/Space_Safety/Space_Debris/Space_debris_by_the_numbers

[6] Christiansen E.L., Meteoroid/Debris Shielding, NASA TP-2003-210788, 2003

[7] ESA, "ESA'S ANNUAL SPACE ENVIRONMENT REPORT." 22 April 2022

[8] D. J. Kessler and B. G. Cour-palais, "Collision Frequency of Artificial Satellites: The Creation of a Debris Belt," Geophys. Res., vol. 83, no. 8, pp. 918–924, 1978, doi: 10.1029/JA083iA06p02637.

[9] J. N. Pelton, Space Debris and Other Threats from Outer Space. 2013

[10] I. S. Group and W. Group, "IADC Space Debris Mitigation Guidelines," no. June 2021

[11] Whipple F. Meteorites and Space Travels, Astronomical Journal, 1161, p. 131 (1947)

[12] Christiansen E.L. et al., "Handbook for Designing MMOD Protection" NASA Johnson Space Center, NASA/TM-2009-214785 (2009).

[13] Cherniaev A., Telichev I., "Design and Analysis Of Orbital Debris Protection For Spacecraft Composite Pressure Vessels", Ph.D. thesis, University of Manitoba, Canada, 2016. Available: https://mspace.lib.umanitoba.ca/xmlui/handle/1993/31949

[14] T. G. Roberts, "Space launch to Low Earth Orbit," 2020. https://aerospace.csis.org/data/space-launch-to-low-earth-orbit-how-much-does-it-cost

[15] B. G. Cour-Palais and J. L. Crews, "A Multi-Shock Concept for Spacecraft Shielding," Int. J. Impact Eng., vol. 10, no. 1–4, pp. 135–146, 1990, doi: 10.1016/0734-743X(90)90054-Y

[16] E. L. Christiansen, "Advanced Meteoroid and Debris Shielding Concepts," Orbital Debris Conf. Tech. Issues Futur. Dir. 1990, 1990, doi: 10.2514/6.1990-1336

[17] D. O. Adams et al., "Multi-functional sandwich composite concepts for spacecraft applications: An initial assessment," Int. SAMPE Symp. Exhib., vol. 51, no. June 2006

[18] M. Schubert and S. Perfetto, "MULTI-FUNCTIONAL LOAD CARRYING LIGHTWEIGHT STRUCTURES FOR SPACE DESIGN Institute of Structural Mechanics and Lightweight Design, RWTH Aachen University, Fraunhofer Institute for Structural Durability and System Reliability LBF, Darmstadt," pp. 1–11, 2017

[19]R. Destefanis, F. Schäfer, M. Lambert, M. Faraud, and E. Schneider, "Enhanced Space Debris Shields for Manned Spacecraft," Int. J. Impact Eng., vol. 29, no. 1–10, pp. 215–226, Dec. 2003, doi: 10.1016/j.ijimpeng.2003.09.019

[20] A. Boudjemai, M. Bekhti, M. H. Bouanane, A. M. Si Mohammed, G. Cooper, and G. Richardson, "Small satellite computer-aided design and manufacturing," Eur. Sp. Agency, (Special Publ. ESA SP, no. 581, pp. 181–188, 2005

[21] C. Paper, S. Dynamics, B. V Sankar, and R. Haftka, "Homogenization of Plates with Microstructure and Application to Corrugated Core Sandwich Panels," no. April 2015, 2010, doi: 10.2514/6.2010-2706

[22] I. Dayyani, A.D. Shaw, E.I. Saavedra Flores, M.I. Friswell, The mechanics of composite corrugated structures: A review with applications in morphing aircraft, Composite Structures, Volume 133, 2015, Pages 358-380, ISSN 0263-8223, https://doi.org/10.1016/j.compstruct.2015.07.099

[23]Carlsson LA, Nordstrand T, Westerlind B. "On the elastic stiffnesses of corrugated core sandwich". Journel of Sandwich Structures & Material, Oct 2001;3(4):253–67

[24] M. R. M. Rejab and W. J. Cantwell, "The mechanical behavior of corrugated-core sandwich panels," Compos. Part B Eng., vol. 47, pp. 267–277, 2013, doi: 10.1016/j.compositesb.2012.10.031.

[25] Santosh Kumar Sahu, P S Rama Sreekanth, et al "A Brief Review on Advanced Sandwich Structures with Customized Design Core and Composite Face Sheet," October 2022 Polymers 14(20):4267 doi: 10.3390/polym14204267

[26] C. Paper, S. Dynamics, B. V Sankar, and R. Haftka, "Homogenization of Plates with Microstructure and Application to Corrugated Core Sandwich Panels," no. April 2015, 2010, doi: 10.2514/6.2010-2706

[27] W. P. Schonberg and R. J. Tullos, "Spacecraft wall design for increased protection against penetration by space derris impacts," AIAA Sp. Programs Technol. Conf. 1990, vol. 29, no. 12, pp. 2207–2214, 1990, doi: 10.2514/6.1990-3663

[28] H. Zhou, R. Guo, and R. Liu, "Protection properties of stuffed corrugated sandwich structures under hypervelocity impact: Numerical simulation," J. Sandw. Struct. Mater., vol. 21, no. 2, pp. 532–551, 2019, doi: 10.1177/1099636217697493

[29] L. Olivieri, C. Giacomuzzo, A. Francesconi, H. Stokes, and A. Rossi, "Experimental characterization of multi-layer 3D-printed shields for microsatellites," J. Sp. Saf. Eng., vol. 7, no. 2, pp. 125–136, 2020, doi: 10.1016/j.jsse.2020.05.001

[30] A. Dumitrescu, S. J. I. Walker, F. Romei, and A. Bhaskar, "Structural assessment and material validation of 3D printed corrugated spacecraft debris shields," no. April, pp. 20–23, 2021

[31] Book “High-velocity impact phenomena” (Ray Kinslow, A. J. Cable, et al.) 1970.

[32] Space station integrated wall design and penetration damage control: final report, contract NAS8-36426, Boeing Aerospace Company, Seattle, WA

[33] Eric L. Christiansen, Justin H. Kerr, “Ballistic limit equations for spacecraft shielding” International Journal of Impact Engineering, Volume 26, Issues 1–10, December 2001, Pages 93-104

[34] S. Ryan, E. Ordonez, E. Christiansen, D. Lear, "Hypervelocity Impact Performance of Open Cell Foam Core," NASA, 2010

[35] M. B. liu G. R. liu, Smooth Particle Hydrodynamics - a meshfree particle method. 2002

[36] A. Yang, J. Li, H. Qu, Y. Pan, Y. Kang, and Y. Zhang, "Numerical Simulation of Hypervelocity Impact FEM-SPH Algorithm Based on Large Deformation of Material," Guti Lixue Xuebao/Acta Mech. Solida Sin., vol. 32, no. October, pp. 1–9, 2016, doi: 10.20944/preprints201610.0055.v1

[37] L. B. Lucy, "A numerical approach to the testing of the fission hypothesis," Astronomical, vol. 82, pp. 1013–1024, 1977.

[38] R. A. G. and J. J. Monaghan, "Smooth particle hydrodynamics: theory and application to non-spherical stars," Astronomical, 1977.

[39] Chun Wang; Yongqi Wang; Chong Peng; and Xiannan Meng, “Smoothed Particle Hydrodynamics Simulation of Water-Soil Mixture Flows” Journal of Hydraulic Engineering, Volume 142 Issue 10 - October 2016

[40] C.A.D.F. Filho: Smoothed Particle Hydrodynamics: Fundamentals and basic applications in continuum Mechanics. 2019.

[41] Monaghan, J.J.: SPH without tensile instability. J. Comput. Phys. 159, 290–311 (2000).

[42] Norman Robertson, Colin Hayhurst, Greg Fairlie, "Numerical simulation of impact and fast transient phenomena using AUTODYNTM-2D and 3D", Nuclear Engineering and Design vol.150 (1994) page 235-241

[43] D. Kong, "A modeling study of filtration mechanisms for micron-particles filtration in fibrous diesel particulate filters," 2019.

[44] P. A. Cundall, "The measurement and analysis of accelerations in rock slopes," vol. 379, no. February, pp. 1–237, 1971

[45] E. Watson and M. O. Steinhauser, "Simulating Hypervelocity Impact Phenomena with Discrete Elements," Procedia Eng., vol. 204, pp. 75–82, 2017, doi: 10.1016/j.proeng.2017.09.728

[46]A. F. J. Levent Aktay, "FEM/SPH Coupling Technique for High-Velocity Impact Simulations," in Advances in Meshfree Technique, 2007, pp. 147–167.

[47] E. P. Fahrenthold and B. A. Horban, "An improved hybrid particle-element method for hypervelocity impact simulation," Int. J. Impact Eng., vol. 26, no. 1–10, pp. 169–178, 2001, doi: 10.1016/s0734-743x(01)00079-3

[48]Andrew Nuttall, Sigrid Close, "A thermodynamic analysis of hypervelocity impacts on metals" International Journal of Impact Engineering, 2020.

[49] Mou-Bin LIU, Shang-ming Li, " On the modeling of viscous incompressible flows with smoothed particle hydrodynamics" Journal of Hydrodynamics, 2016.

[50] ANSYS, Explicit_STR Lecture 6: Material Models, 2012.

[51]] S. Hiermaier, Structures Under Crash and Impact: Continuum Mechanics, Discretization and Experimental Characterization, Springer, 2008.

[52] Meyers M.A. Dynamic behavior of materials. John Wiley and Sons, Inc. (1994)

[53] Zukas J. A. "Introduction to hydrocodes" Elsevier (2004)

[54] Afaf M. Abd El-Hameed, Y. A. Abdel-Aziz1, "Aluminium Alloys in Space Applications: A Short Report" Journal of Advanced Research in Applied Sciences and Engineering Technology 22, Issue 1 (2021) 1-7.

[55] Victor O. Babarinde, Anton Kuznetcov, and Igor Telichev, "Morphologically Accurate Numerical Model of Satellite Foam-Core Panel Impacted by Orbital Debris" AIAA JOURNAL Vol. 60, No. 4, April 2022.

[56] Zongwen Li, Jianxun Ma, "Properties and Applications of Basalt Fiber and Its Composites" IOP Conference Series: Earth and Environmental Science, 2018

[57] Yan Zhaopu, Wang Yangwei, et al, "Research Progress On Static And Dynamic Mechanical Properties And Ballistic Properties Of Basalt Fiber Composites" MATERIAL REPORT, 2022, Vol. 36, No.4.

[58] Rajesh Mishra, Hafsa Jamshaid, and Jiri Militky, "Investigation of Mechanical Properties of Basalt Woven Fabrics by Theoretical and Image Analysis Methods" Fibers and Polymers 2017, Vol.18, No.7, 1369-1381

[59] Adrian Dumitrescu, Scott J. I. Walker, et al, “Structural assessment and material validation of 3D printed corrugated spacecraft debris shields” 8th European Conference on Space Debris (virtual), Darmstadt, Germany, 20–23 April 2021

[60] Aleksandr Cherniaev*, Igor Telichev, “Meso-scale modeling of hypervelocity impact damage in composite laminates” Composites Part B, 2015

[61] M. S. Cowler, O. La'adan, T. Ohta, “High performance computing using AUTODYN-3D” © 2000 WIT Press.

[62] ANSYS Autodyn User's Manual, release 19.0, January 2018

[63] https://um-grex.github.io/grex-docs/

[64] K.M. Zhao, J.K. Lee, "Finite element analysis of the three-point bending of sheet metals", Journal of Materials Processing Technology, Volume 122, Issue 1, 5 March 2002, Pages 6-11

[65] https://asm.matweb.com/search/SpecificMaterial.asp?bassnum=ma6061t6

[66] B.S. Aakash, John Patrick Connors, Michael D. Shields, "Variability in the thermo-mechanical behavior of structural aluminum" Journal- thin-walled structures, 21st January 2019

[67] Christiansen, E. L., Crews, J. L., Williamsen, J. E., Robinson, J. H., & Nolen, A. M. (1995). Enhanced meteoroid and orbital debris shielding. International Journal of Impact Engineering, 17(1-3), 217–228. doi:10.1016/0734-743x(95)99848-l

[68] Destefanis, R., Schäfer, F., Lambert, M., & Faraud, M. (2006). Selecting enhanced space debris shields for manned spacecraft. International Journal of Impact Engineering, 33(1-12), 219–230. doi:10.1016/j.ijimpeng.2006.09.065

[69] Putzar, R., Zheng, S., An, J., & Hovland, S. (2019). A stuffed Whipple shield for the Chinese space station. International Journal of Impact Engineering. doi:10.1016/j.ijimpeng.2019.05.018

[70] https://hvit.jsc.nasa.gov/shield-development/#:~:text=The%20Stuffed%20Whipple%20Shield%20is,reaching%20the%20rearwall%20are%20benign.

[71]E. L. Christiansen, J. L. Crews, J. E. Williamsen, J. H. Robinson, and A. M. Nolen, “Enhanced Meteoroid and Orbital Debris Shielding,” vol. 17, pp. 217–228, 1995.

[72] M. Higashide, M. Tanaka, Y. Akahoshi, S. Harada, and F. Tohyama, “Hypervelocity Impact Tests Against Metallic Meshes,” Int. J. Impact Eng., vol. 33, no. 1–12, pp. 335–342, 2006, doi: 10.1016/j.ijimpeng.2006.09.071.

[73] E. Schneider, F. K. Schäfer, R. Destefanis, and M. Lambert, “Advanced Shields for Manned Space Modules Frank Schäfer , Roberto Destefanis Michel,” no. 1, pp. 1–13, 2004, doi: 10.2514/6.IAC-04-IAA.5.12.2.01.

[74] K. Thoma, F. Schäfer, S. Hiermaier, and E. Schneider, “An Approach to Achieve Progress in Spacecraft Shielding,” Adv. Sp. Res., vol. 34, no. 5, pp. 1063–1075, 2004, doi: 10.1016/j.asr.2003.03.034.

[75] E. L. Christiansen, K. Nagy, D. M. Lear, and T. G. Prior, “Space Station MMOD shielding,” Acta Astronaut., vol. 65, no. 7–8, pp. 921–929, 2009, doi: 10.1016/j.actaastro.2008.01.046.

[76]Eric Christiansen, MMOD Protection and Degradation Effects for Thermal Control Systems, NASA Johnson Space Center August 2014 https://ntrs.nasa.gov/api/citations/20140010668/downloads/20140010668.pdf.

[77] S. M. Hull, "A Proposal for Standardized MMOD Shielding for Robotic Spacecraft," 2019.

[78] M. S. Pryzby et al., "Landsat 9 Micrometeoroid and Orbital Debris (MMOD) Mission Success Approach," in First Int'1. Orbital Debris Conf. (2019), 2019, pp. 1-6.

[79] NASA, "Process for Limiting Orbital Debris," 2019

[80] Taylor, E. A., Herbert, M. K., Vaughan, B. A. M., & McDonnell, J. A. M. (1999). Hypervelocity impact on carbon fibre reinforced plastic / aluminium honeycomb: Comparison with whipple bumper shields. International Journal of Impact Engineering, 23(1), 883–893. doi:10.1016/s0734-743x(99)00132-3

[81]Yasensky J., Christiansen E. Hypervelocity Impact Evaluation of Metal Foam Core Sandwich Structures. JSC63945 (2007).

APPENDICES

Appendix A

Vulnerable location of CCSP

The outcome is obtained by simulating 12 different cases shown below.

#1.1

In the case where a 3.3mm spherical projectile impact bumper along with the Peak of CC at **0° angle**:

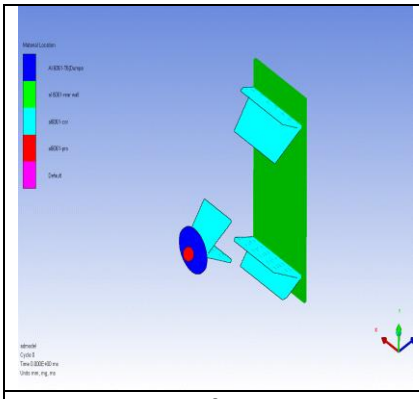	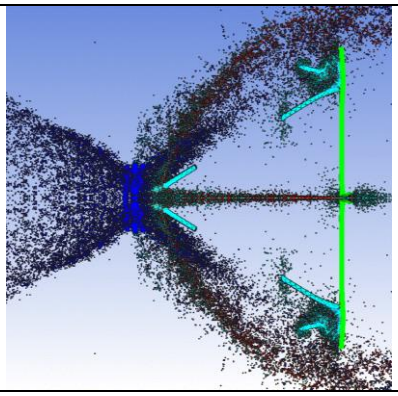	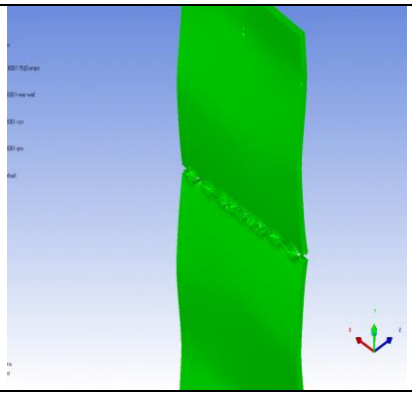
3D view of the model	Side view at 15 microseconds	Rear wall at 30 micro-second

#1.2

In the case where a 3.3mm spherical projectile impact bumper towards the Peak of CC at **30° angle**:

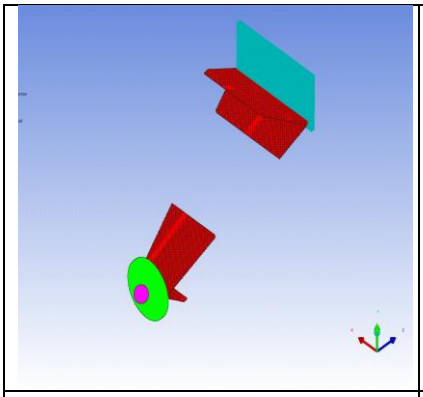	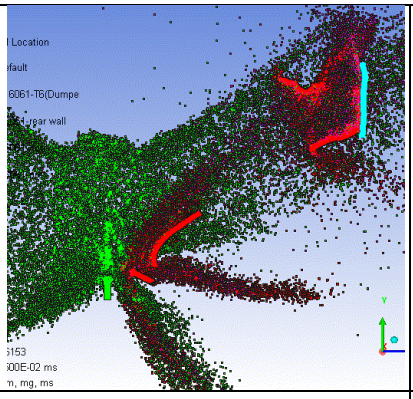	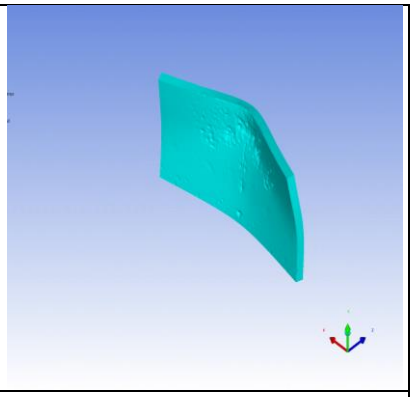
3D view of the model	Side view at 15 microseconds	Rear wall at 30 micro-second

#1.3

In the case where a 3.3mm spherical projectile impact bumper towards the Peak of CC at **45° angle**:

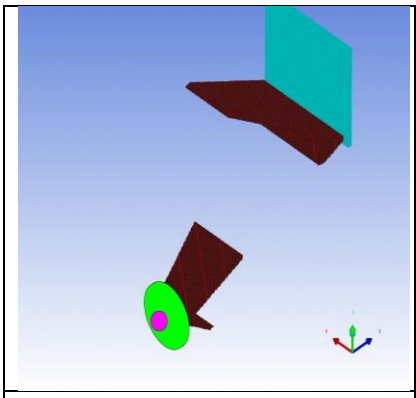	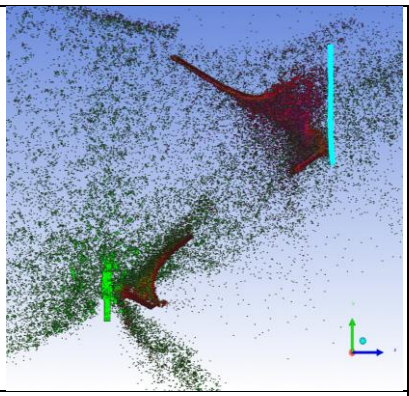	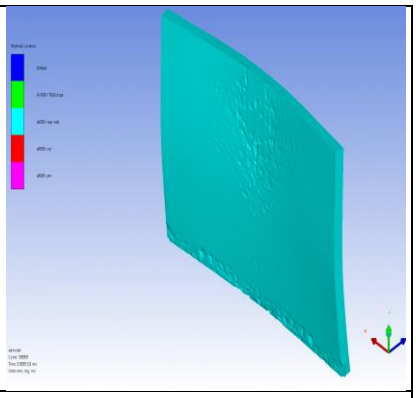
3D view of the model	Side view at 15 microseconds	Rear wall at 30 microseconds

#1.4

In the case where a 3.3mm spherical projectile impact bumper towards the Peak of CC at **60° angle**:

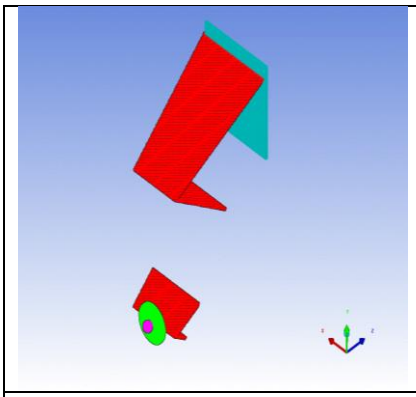	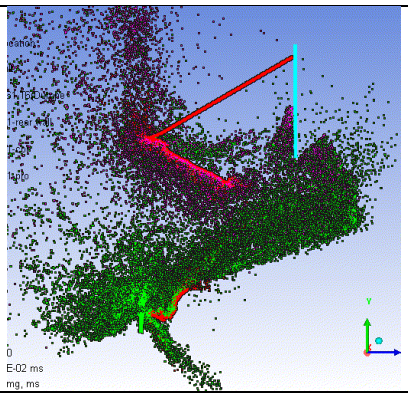	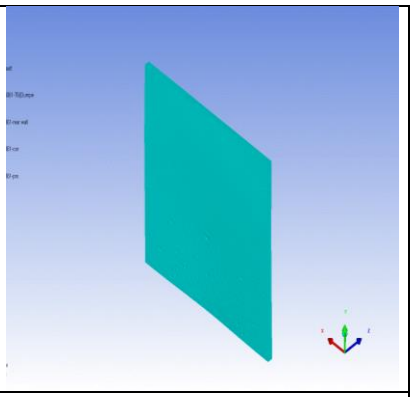
3D view of the model	Side view at 15 microseconds	Rear wall at 30 micro-second

#2.1

In the case where a 3.3mm spherical projectile impact bumper towards the middle of CC slope at **0° angle:**

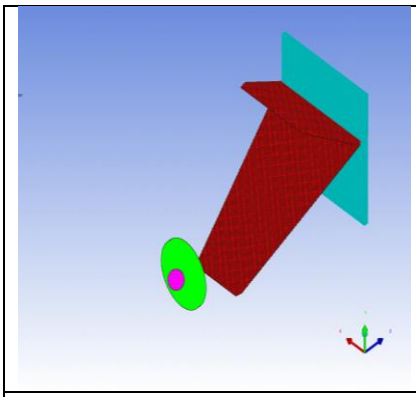	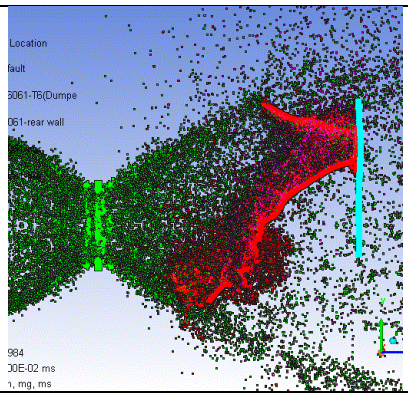	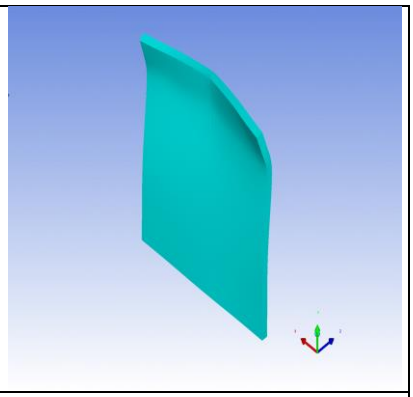
3D view of the model	Side view at 15 microseconds	Rear wall at 30 micro-second

#2.2

In the case where a 3.3mm spherical projectile impact bumper towards the middle of CC slope at 3**0° angle:**

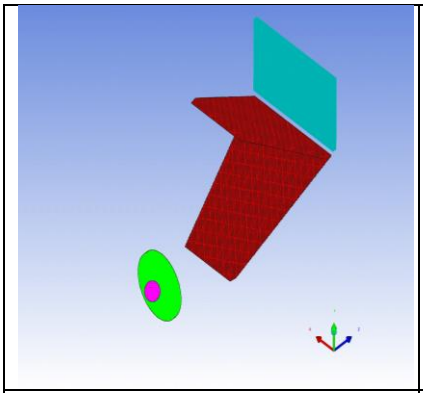	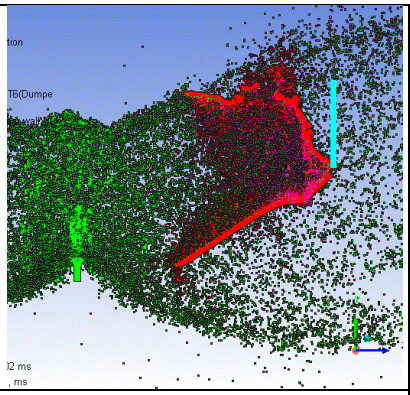	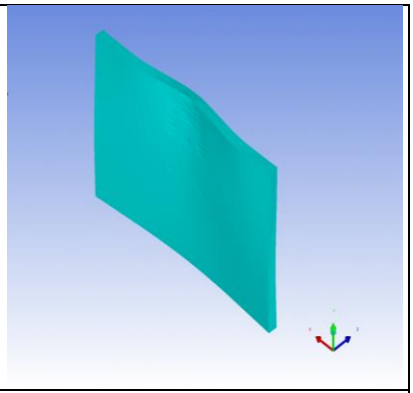
3D view of the model	Side view at 15 microseconds	Rear wall at 30 micro-second

#2.3

In the case where a 3.3mm spherical projectile impact bumper towards the middle of CC slope at **45° angle:**

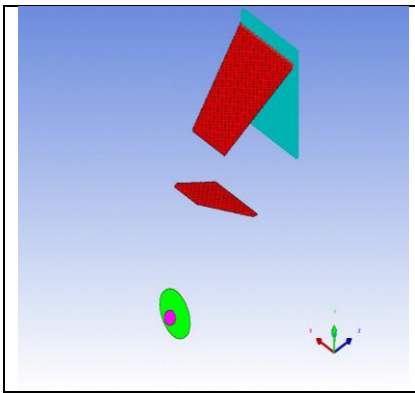	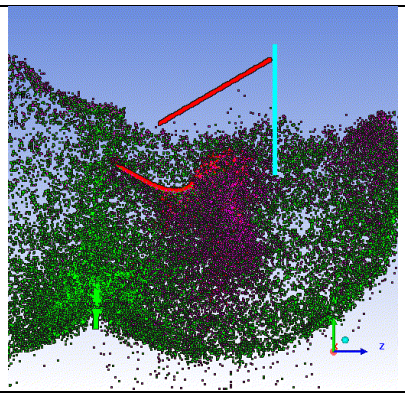	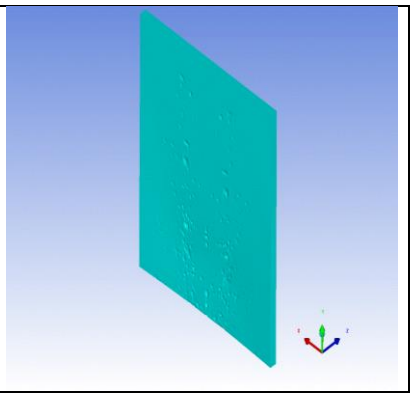
3D view of the model	Side view at 15 microseconds	Rear wall at 30 micro-second

#2.4

In the case where a 3.3mm spherical projectile impact bumper towards the middle of CC slope at 6**0° angle:**

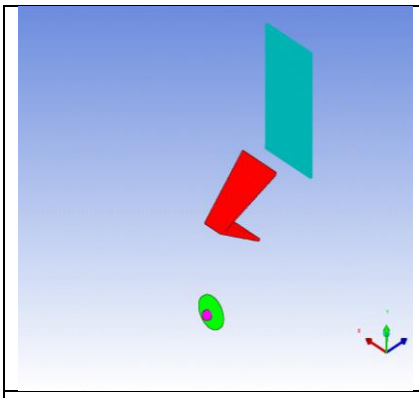	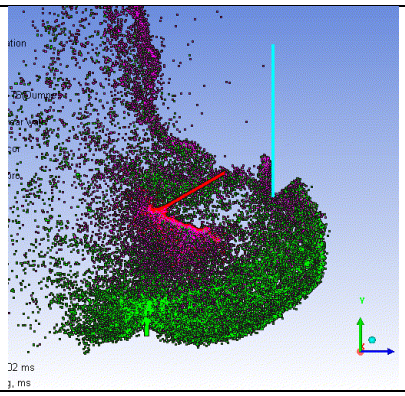	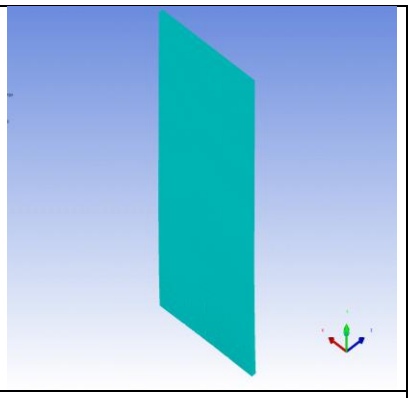
3D view of the model	Side view at 15 microseconds	Rear wall at 30 micro-second

#3.1

In the case where a 3.3mm spherical projectile impact bumper towards the valley of CC at **0° angle:**

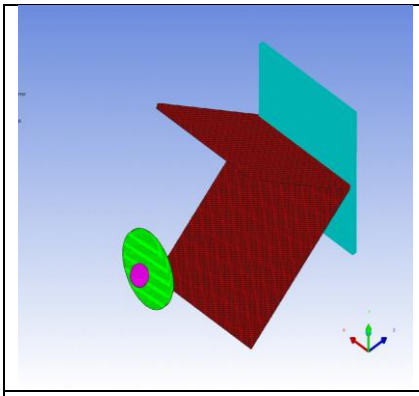	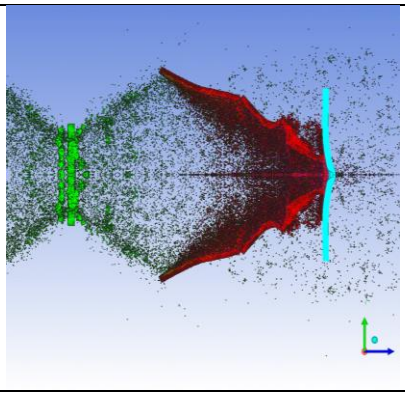	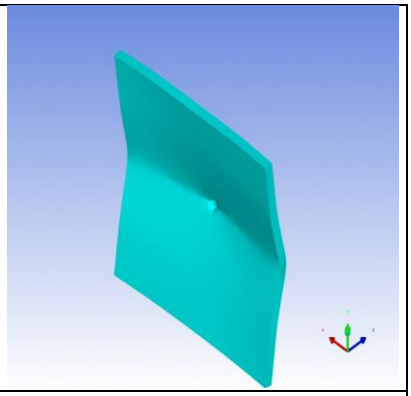
3D view of the model	Side view at 15 microseconds	rear wall at 30 micro-second

#3.2

In the case where a 3.3mm spherical projectile impact bumper towards the valley of CC at 3**0° angle:**

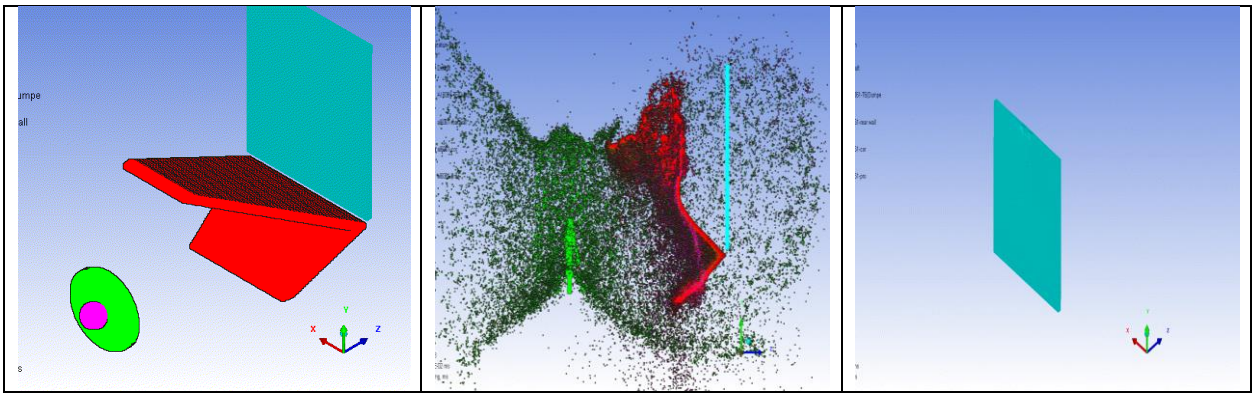

3D view of the model	Side view at 15 microseconds	Rear wall at 30 micro-second

#3.3

In the case where a 3.3mm spherical projectile impact bumper towards the valley of CC at **45° angle:**

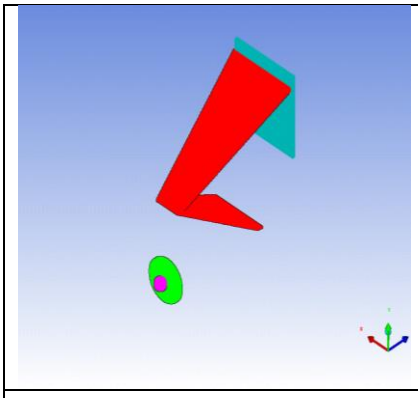	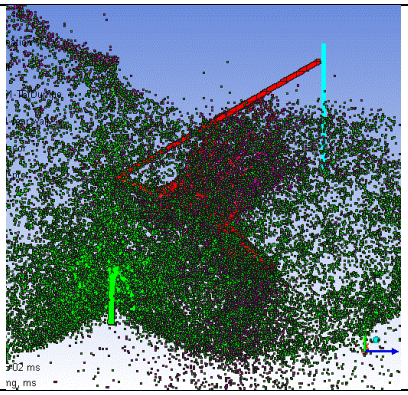	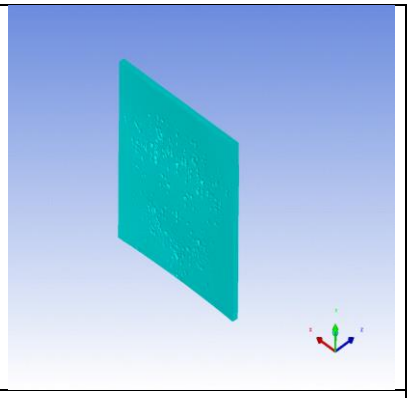
3D view of the model	Side view at 15 microseconds	Rear wall at 30 micro-second

#3.4

In the case where a 3.3mm spherical projectile impact bumper towards the valley of CC at **0° angle:**

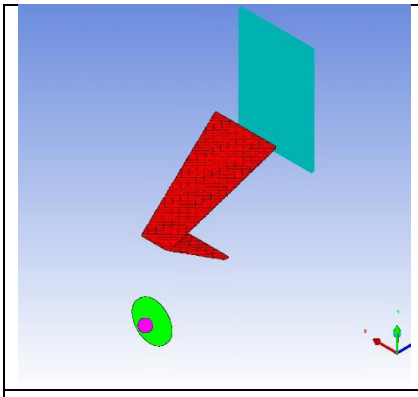	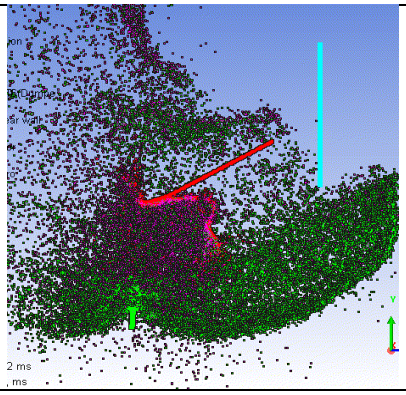	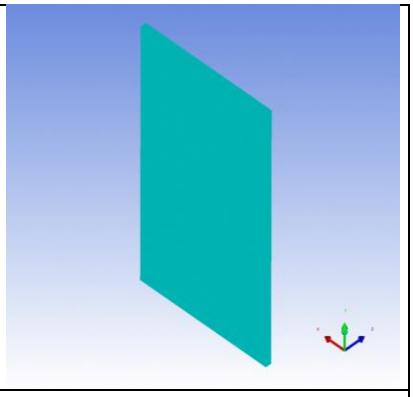
3D view of the model	Side view at 15 microseconds	Rear wall at 30 micro-second

Energy absorbed by the CCSP model at different positions and angles is demonstrated in the table below. The least int. energy and plastic work have happened when the projectile impact in the direction of the peak of the cor. slope.

#NO	Impact Location	Impact Angle	Max Plastic WK (µJ) at 30 microseconds	Max Int. Energy (µJ) at 30 Microseconds	Rear wall status
1.1	Peak of CC	0°	**1.9698e+07**	**1.219e+08**	Perforation
1.2	Peak of CC	30°	3.8985e+07	2.8405e+08	Bended, No perforation
1.3	Peak of CC	45°	3.900e+07	2.8458e+08	Small craters, no perforation
1.4	Peak of CC	60°	4.5884e+07	2.4255e+08	No crater, no perforation
2.1	Middle of CC slope	0°	4.1577e+07	3.7792e+08	Bended, No perforation
2.2	Middle of CC slope	30°	4.5045e+07	3.422e+08	Bended, No perforation
2.3	Middle of CC slope	45°	3.8723e+07	2.2569e+08	Small craters, no perforation
2.4	Middle of CC slope	60°	4.4386e+07	2.4348e+08	No Crater, no perforation
3.1	Valley of CC	0°	**2.7528e+07**	**1.9995e+08**	Bending, Tiny perforation
3.2	Valley of CC	30°	NA	NA	NA
3.3	Valley of CC	45°	3.7938e+07	2.9160e+08	Small craters, no perforation
3.4	Valley of CC	60°	5.8421e+07	3.5980e+08	No Crater, no perforation

Higher the int. energy and plastic work, lower the damage on the rear facesheet of the CCSP. Least amount of plastic work was done at the impact at the peak and valley cross section. As a result, the panel is most vulnerable at the valley and peak of the corrugated core.

Appendix B

Different type of core design and their critical diameter

There are four more corrugated core designs. Trapezoid, sinusoids, rectangle, and X-shape core. Every corrugated core has the same areal density same as the primary triangle core.

Table 1 four more corrugated core designs

Core type	Parameter of the panel	Isometric view
Trapezoid core	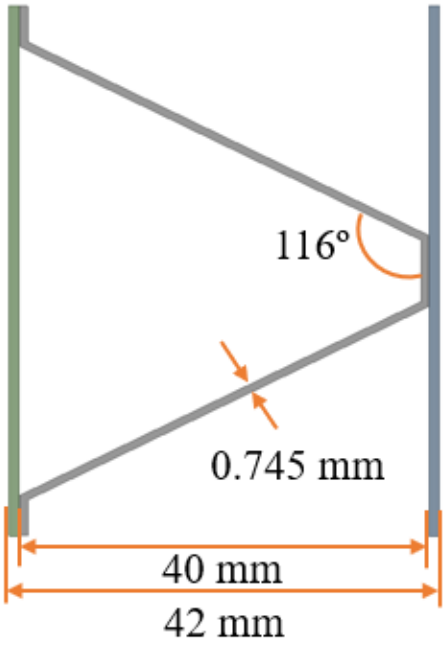	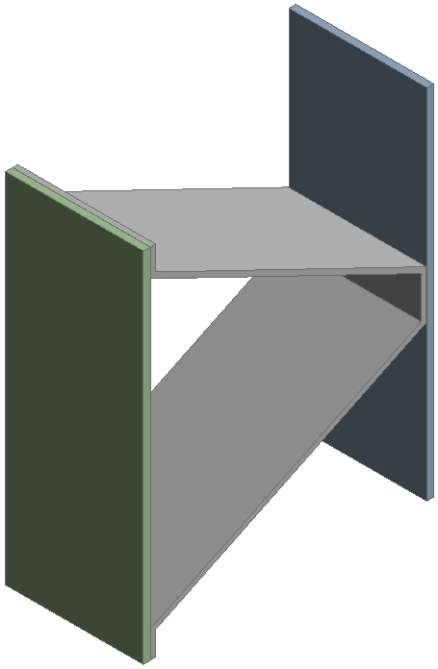
Sinusoid core	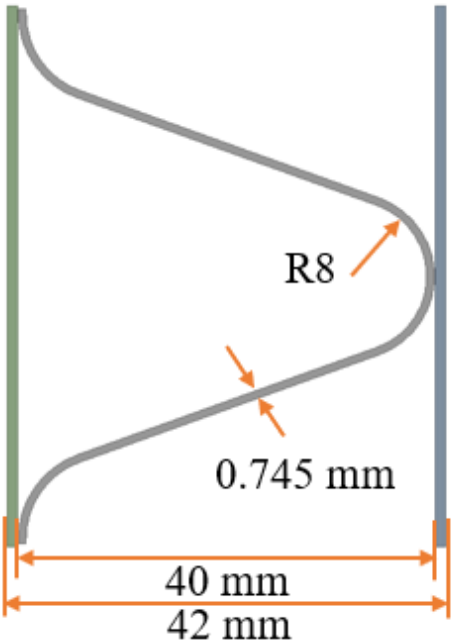	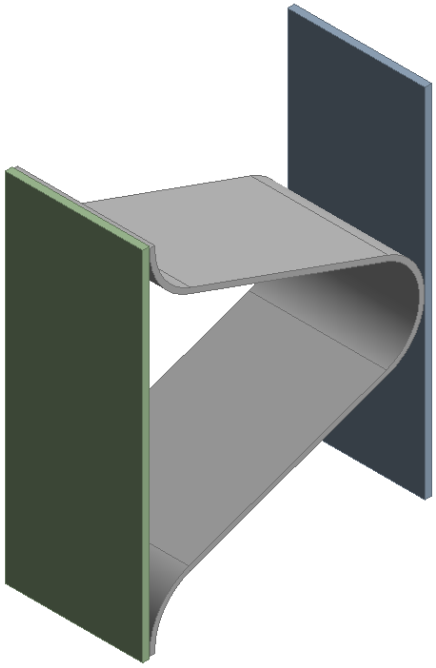

Rectangle core

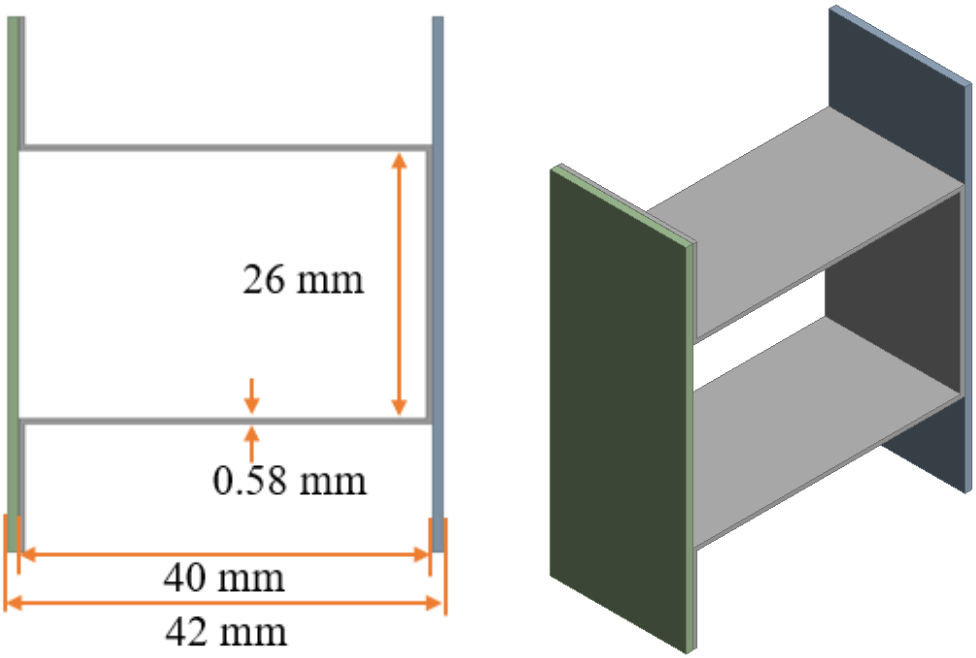

X-shape core

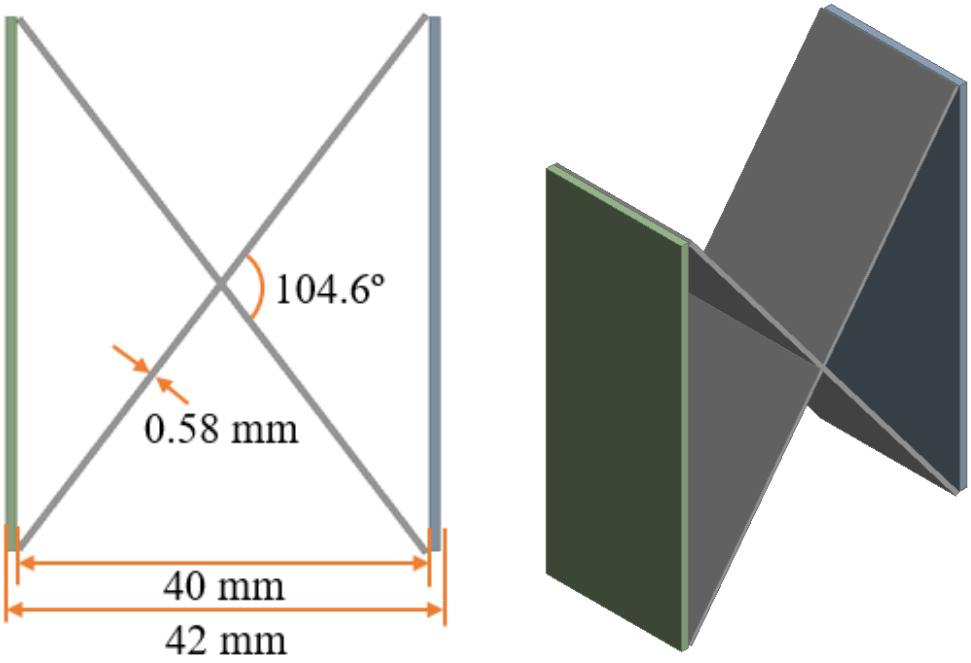

Numerical simulation over CCSP with various corrugated core.

Table 2 Numerical model and outcome of various corrugated core

Core Type	Isometry view of Numerical model	Simulation results after 8 μs	Rear facesheet simulation after the simulation
Trapezoid	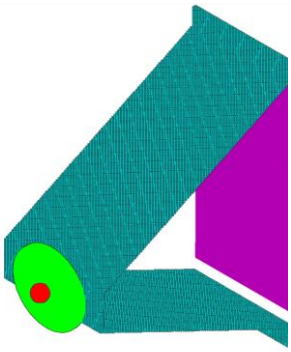	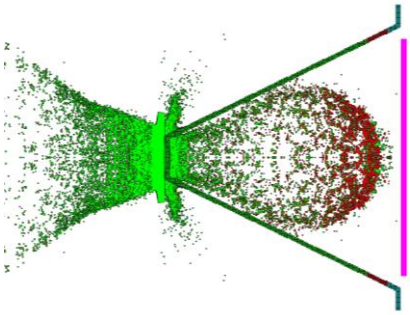	
Sinusoid	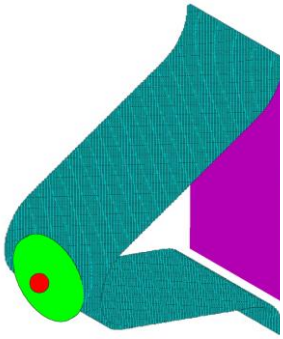	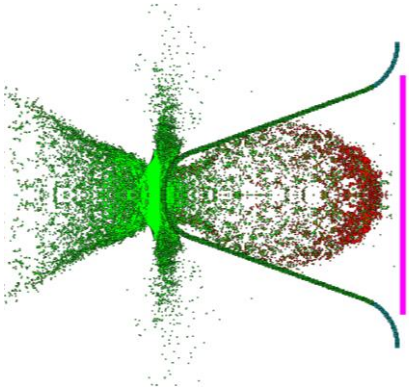	
Rectangle	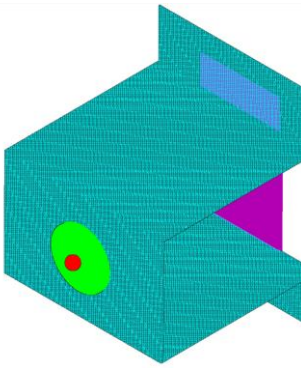	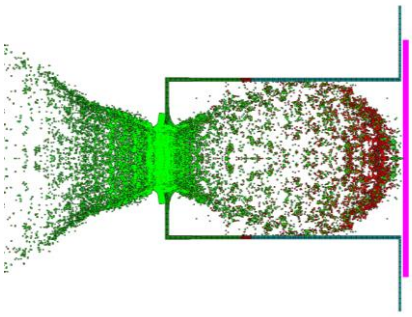	
X-shape	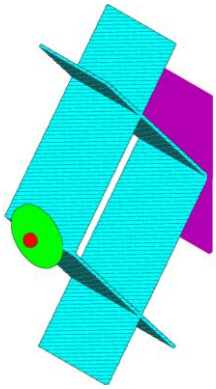	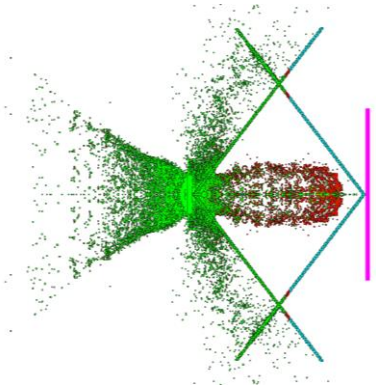	

The areal density of different cores is constant (9.41kg/m^2). The critical diameter of projectile for the trapezoid, sinusoid, rectangle, and X-shape core is lower than the triangle corrugated core as presented in section (4.6). Table-5 shows the trapezoid, sinusoid, rectangle, and X-shape critical diameter of the projectile.

Table 3 Critical diameter of the different corrugated core configuration

Corrugated Core shape	**Critical diameter of the projectile, mm**
Triangle	2.7
Trapezoid	2.55
Sinusoid	2.4
Rectangle	2.5
X-shape	2.2